# Investigation of Spin Injection in Semiconductors: Theory and Experiment

Thesis by

Stephan R. Ichiriu

In Partial Fulfillment of the Requirements

for the Degree of

Doctor of Philosophy


California Institute of Technology

Pasadena, California

2005

(Submitted May 26, 2005)

# Acknowledgements

When I first arrived at Caltech, I was a snot-nosed kid with no background whatsoever in semiconductor physics. Having grown up a little during my time here, I've found that I'm still snot-nosed, but at least I now know a thing or two about semiconductor devices. There are many people who have contributed greatly along the way and I'd like to take a moment to express my sincere gratitude and appreciation.

Tom, thank you for giving me the opportunity to be a part of the legacy you have left behind. You have provided me with an unparalleled education—our lab facilities were certainly the envy of many other research groups and the freedom that you gave your students in their work allowed us to explore topics that actually motivated us. Thank you for giving me the freedom to fail as well as to succeed. I have perhaps learned more from what didn't work than what did. As your last remaining graduate student, I wish you the best in your remaining years at Caltech and in any future endeavors.

Gerry, thank you for the countless discussions and insight that you gave me. The light that you shed on the significant problems I faced in my research helped guide and direct my efforts. I hope that you and Joy are able to make further serendipitous contributions to the world of astronomy and society in general now that there are no more grad students to help.

Tim, who knew that in the course of your time working with the SSDP group that you would step out of the office and into the lab? Thank you for your help over the last few months of my research; I couldn't have done it without you. Good luck to you and Esther in Albuquerque, and happy rail fanning!

The most important part of my educational experiences at Caltech have most certainly come from my daily interactions with our group's postdocs and fellow graduate students. I have been fortunate enough to be a part of a research group where our camaraderie made my experiences not only educational, but fun. Thank you, Cory, for the immeasurable help that you have given me in my research. Your expertise in MBE growth and characteriza-

tion techniques has never ceased to amaze me. Bob, thanks for sharing your insight and knowledge of device physics with me. Much of what I have included in the chapter on device characterization I owe to discussions with you. Rob, thank you for your help with the electrical characterization of my devices and with that darn MMR probe station. You could always be counted on to bring a sense of levity to any situation. Thank you, Paul, for your encouragement and dry wit. Talking with you always motivated me to work harder to finish. Thanks, Neal, for helping me to gain a slightly better appreciation for materials science and for helping me from afar with the metalization chamber. I could not have asked for a better officemate. I hope your desk at Intel is a step up from that big cardboard box you were using! Ed, thanks for showing me that it's possible to jury-rig just about anything in the lab. I bet you could make a new hemispherical analyzer for our XPS system from a handful of peanuts and two Coke cans. Xavier, thank you for sharing your insane understanding of solid state theory with us. The Monte Carlo simulation would have been impossible aside from your contributions to the photon generation code. And Justin, thanks for showing me the ropes on the cryostats. And thanks also for showing me that it is possible to successfully make the transition from high-energy physics to solid state. To all of the guys, thanks for the hours of "network testing." The stress relief from that has certainly helped me to push through and finish this thesis.

To all of my friends, thank you for your countless prayers and words of encouragement. You all have been there on the sidelines cheering me on and for that I am truly grateful. Thanks especially to the gang from No Limit for always believing in me and helping me to push forward. I have certainly been sharpened through my relationships with all of you. Thank you, Taylor, for your friendship. You've got all kinds of skills—guitar skills, magic skills, youth pastoring skills.... You're one amazing guy and I feel privileged to call you my friend. Thanks for helping me to keep my eye on the prize.

To my family, thank you for seeing the potential inside of me and helping me to drag that out. None of this would have been possible without your love and support. Dad, Hazel, Mike, Vincent, Debbie, Cynthia, Kevin, and Theresa—I love you guys.

Finally, thank you, Jesus, for the tremendous blessings that you have poured out into my life. All that I have and all that I am I owe to you. הַלְלוּיָהּ

# Abstract

Spin electronics, or *spintronics*, is a nascent field of research whereby the spin degree of freedom in electronic devices is exercised. The electroluminescence polarization of the spin light emitting diode (spin-LED) is important in the characterization of spin injection efficiency into non-magnetic semiconductors. The validity of these measurements is questioned due to the use of large external magnetic fields during measurement and the effects of reflection and refraction within the semiconductor structure. A Monte Carlo ray-tracing simulation for the spin-LED was written to address these issues and a device-dependent polarization correction factor was calculated for the Fe/$Al_{0.2}Ga_{0.8}As$ system to account for these effects. Spin injection into $Al_{0.2}Ga_{0.8}As$ from Fe and Co-Cr spin aligning contacts via a Schottky barrier was measured. Fe was chosen because of the strong spin polarization of conduction electrons at the Fermi level, while Co-Cr was selected because of its properties as a perpendicular magnet for certain alloy concentrations. The contacts were epitaxially grown at room temperature by electron-beam evaporation. These samples were measured to have zero spin injection. The results were attributed to the Schottky barrier properties.

# Contents

# List of Figures

# List of Tables

# Chapter 1 Spin Manipulation for Fun and Profit

## 1.1 Why Spintronics?

### 1.1.1 A Brief History of Si CMOS

In 1948, Bardeen and Brattain announced the development of the point-contact transistor [1]. Little did they know the tremendous impact that this invention from Bell Laboratories would have. Semiconductor transistor technology blossomed in the 1960s as planar processing techniques paved the way for the development of the integrated-circuit (IC) and microprocessor. These advancements are responsible for the creation of what is now a $200B industry. ICs can be found in everything from seemingly pedestrian household appliances to the most advanced probes designed for deep-space exploration. The past 57 years of human history have been tremendously affected by the invention of one device.

Silicon complementary metal-oxide-semiconductor (CMOS) technology, where both *p*-channel and *n*-channel metal-oxide-semiconductor field effect transistors (MOSFETs) are formed on the same Si substrate, has been of primary importance in these advancements (see Figure 1.1). Conduction between the source and drain contacts of each transistor is controlled by the application of a voltage to the gate contact. As the gate voltage is varied, the carrier concentration in the semiconductor material beneath the gate oxide changes. For an *n*-channel MOSFET device the application of a positive bias to the gate will cause a depletion of holes in the *p*-type substrate. Increasing the bias further for such a device will cause an inversion layer to form at the oxide-semiconductor interface, which acts as a conducting channel between the source and drain contacts.

The ability to scale Si CMOS down to smaller and smaller dimensions has been the driving force behind the IC industry. Oxide thickness, gate length, doping concentrations,

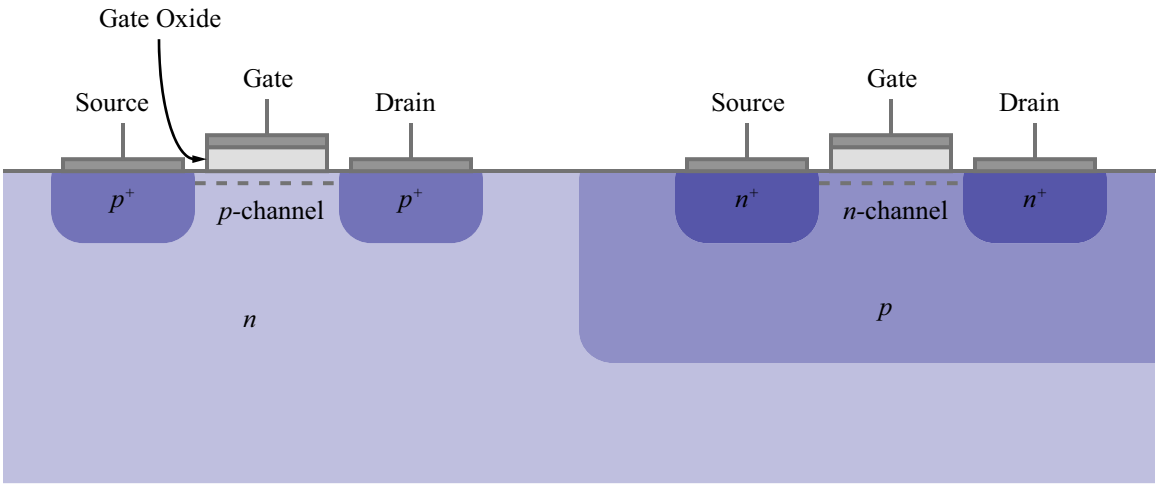


Figure 1.1: CMOS transistors using $p$-well technology. Important device parameters are the oxide thickness, $d$, and the gate length, $L$.

applied voltages, and all other relevant device parameters can be scaled in a way such that device performance remains constant. As device size shrinks, speed increases and power consumption decreases. In fact, scaling of CMOS technology has proceeded at such a predictable rate that Gordon Moore's observation, commonly known as Moore's law, that transistor density would double every 18 months has held true for the past 30 years [2].

### 1.1.2 The End of an Era

All good things must come to an end, and it appears that standard Si CMOS technology, the driving force behind the semiconductor industry for well over half a century, is preparing to leave the limelight. For years, methods were found to continue to scale oxide thickness, gate length, and all other important device parameters to keep in step with Moore's law. As characteristic thicknesses and lengths are reduced, however, challenges due to processing issues such as lithography and scaling issues like oxide leakage become increasingly significant. Many innovative techniques have been employed to extend the life of this material system—alternative gate dielectrics, high-conductivity interconnect materials, and silicon-on-insulator techniques have all played their supporting roles in breathing new life into Si CMOS technology. Unfortunately, the IC industry is fast approaching a time when even these Band-Aid measures will be unable to keep the exponential increase in device density

going. New material systems and new technologies must be investigated.

In addition to these scaling issues, the computational systems based upon conventional Si CMOS logic all follow classical computational principles. Classical computers are good at performing many different kinds of calculations, but there are definitely problems for which this technology is not well-suited. Factoring numbers, for example, is at best an $O\left[\exp\left(\left(\frac{64}{9}\right)^{1/3} N^{1/3} (\log N)^{2/3}\right)\right]$ problem [3]—the time required to solve this type of problem with a classical computer increases exponentially with the byte length, $\lceil \log N \rceil$, of the number $N$ to be factored. Fast factorization of large numbers is especially important for applications in the intelligence community because current data encryption techniques make heavy use of the difficulty of such factorization.

With the current emphasis on homeland security in this country, the ability to quickly sift through large amounts of possibly encrypted data has become increasingly important. Classical computers are clearly deficient in this arena. Making smaller and faster microprocessors may reduce computation time, but the addition of several bytes to the data encryption strength will quickly nullify any gains made through these means. What we need, then, is not just another artificial respirator to keep Si CMOS going for a few more years, but a new approach to electronics that is not bound by the same limitations as this technology.

## 1.2 Spintronics: A New Hope

In 1997, Datta and Das introduced a device concept that could possibly completely revolutionize semiconductor electronics. What was their idea? It was the spin transistor [4].

Electrons and holes, the elementary constituent components of electronic devices, not only carry electrical charge but also have a magnetic character contained within their spin. Spin electronics, or *spintronics*,[1] seeks to employ this spin degree of freedom to extend the realm of semiconductor electronics. Rather than storing or transferring information through the absence or presence of charge carriers, we may encode the required information upon the spins of these particles. This introduces new possibilities that are not available with

[1] See references [5–9] for several thorough reviews of this emerging field.

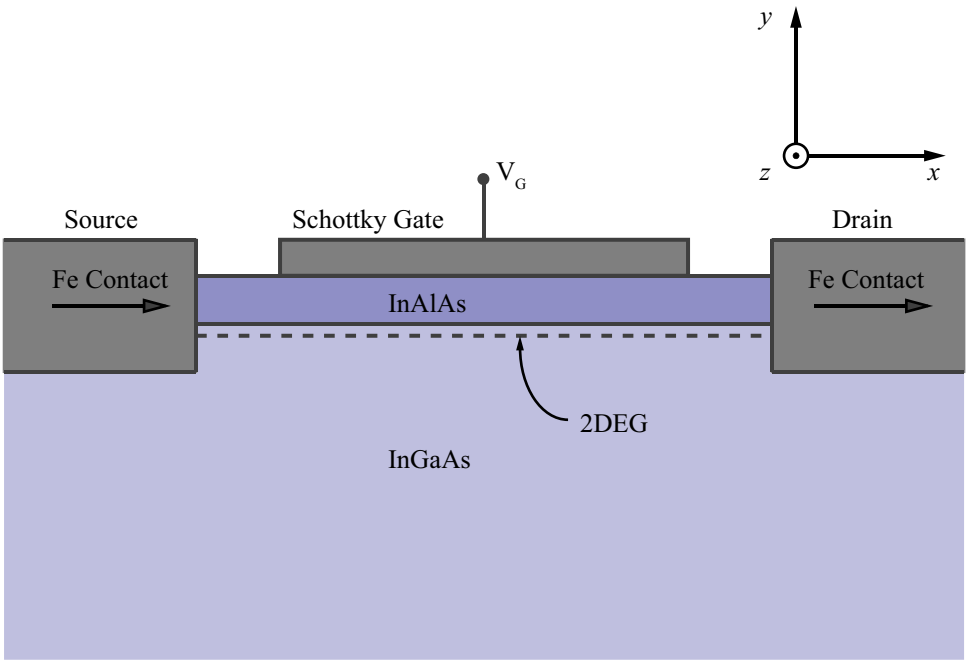


Figure 1.2: Spin transistor proposed by Datta and Das. Figure adapted from reference [4].

existing technologies.

The device proposed by Datta and Das is the first of such spintronic devices and is shown in Figure 1.2. It consists of ferromagnetic source and drain contacts connected by a two-dimensional electron gas (2DEG) formed by a heterojunction between two narrow gap semiconductor materials, in this case $In_xAl_{1-x}As$ and $In_xGa_{1-x}As$. Spin-aligned electrons are injected into the 2DEG from the source contact. For electrons traveling along $x$, the Rashba term to the Hamiltonian

$$H_R = \eta\left(\sigma_z k_x - \sigma_x k_z\right), \tag{1.1}$$

where $\eta$ is the spin-orbit coupling constant, will give rise to a difference in energy and hence a difference in wave vector between electrons with their spins aligned along $+z$ and $-z$. This difference in wave vector is translated into a phase shift that can be detected at the drain contact due to a change in magnetoresistance. Varying the potential applied to the gate contact changes the strength of the Rashba Hamiltonian and thus the conduction properties of the device.

Why is this device concept so important? Traditional electronics have relied upon the movement or storage of electrical charge carriers. The spin transistor, on the other hand, operates principally upon the magnetic character of the same particles. When the state of an electrical system is to be changed, the electrons or holes themselves must be moved. Changing the magnetic state does not require charge transfer. Imagine a transmission line in which spin information is passed from electron to electron without any movement of the charge carriers.[2] The net effect would be a transmission of information through a spin current with zero electrical current. The transfer rate over such a transmission line could conceivably be greater than what is presently available because RC limitations no longer apply in the absence of an electrical current. Power consumption would also decrease for the same reason.

### 1.2.1 Quantum Computation

Information transfer is just one possible application of spintronics. Computation using devices based on this type of technology is yet another tempting application [10, 11].

Classically, computers operate using well-defined binary information states. A bit that is stored in memory can either be a 1 or a 0 depending upon the state of the system in which the bit is stored. The computer reads this information state and performs a series of logic functions on that information, which results in the output of another well-defined binary information state. If the same series of operations must be done on several sets of information states, those operations must be done serially.

Because of the quantum nature of spin, the electrons and holes can be prepared in states that are not simply spin up or spin down, but any linear combination of the two. The state of a single quantum bit, or *qubit*, would be

$$\psi_1 = a\,|\uparrow\rangle + b\,|\downarrow\rangle\,, \tag{1.2}$$

where the probability amplitudes $a$ and $b$ satisfy the relation $|a|^2 + |b|^2 = 1$. For a two qubit

[2] This could be realized for a system with a uniform carrier distribution, but nonuniform spin population. Spin diffusion would cause the tranfer of spin information without charge transfer.

system, the wavefunction would be

$$\psi_2 = a\,|\uparrow\uparrow\rangle + b\,|\uparrow\downarrow\rangle + c\,|\downarrow\uparrow\rangle + d\,|\downarrow\downarrow\rangle\,, \tag{1.3}$$

where $|a|^2 + |b|^2 + |c|^2 + |d|^2 = 1$. A quantum computer would then take these information states and perform logic operations on them, much in the same way that computation is performed classically. The essential difference, however, is that the initial system is prepared in a superposition of states so the result of the calculation is an information state that is also a superposition of states. Rather than looking up a single value in the truth table represented by this state machine, whole sections of the truth table are probed at the same time. The quantum computer performs in parallel what a classical computer would have to do serially.

Shor's algorithm is a direct application of the principles of quantum computation to a real-world problem. The algorithm describes steps that can be used on a quantum computer to efficiently factorize a number $N$. The details of the algorithm itself are beyond the scope of this work and are described elsewhere, but its computational complexity is $O\left((\log N)^2 \log\log N\right)$ on a quantum computer with an additional $O(\log N)$ steps necessary on a classical computer to finish the calculation [12]. Compared with the exponential complexity of the most efficient classical algorithm, Shor's polynomial-time algorithm for factorization is clearly superior.

### 1.2.2 Spintronics in the Solid State

All of this sounds great in theory, but spintronic devices will never be commercially viable unless several conditions are met. First, technologically feasible techniques for state preparation and detection must be developed. Second, methods for the logical manipulation of these states must be established. Third, the technology must be reasonably priced. Economies of scale can help to reduce the cost for individual devices. Finally, room temperature operation, although not absolutely necessary, is desired for commercial applications.

Utilizing the solid state for spintronics seems like a natural fit because semiconductor materials are well-understood. Our current knowledge of these materials is a definite

advantage in attempting to satisfy the first and second requirements stated above. As for the third and fourth requirements, they are easily satisfied in the solid state. The existing fabrication and processing technology surrounding these materials should allow for rapid low-cost development of this burgeoning field once the first two conditions are met. Temperature-stable device operation is brought about through the use of doping. The activation energies for impurity ionization and intrinsic carrier generation are such that device operation is predictable over a wide range of temperatures.[3]

The task, then, is first to produce and subsequently to manipulate spin currents in the solid state.

## 1.3 Spin Currents in Semiconductors

Creating a spin-polarized current in a semiconductor at room temperature is much more difficult than one might initially believe. Most semiconductors are naturally nonmagnetic so a nonequilibrium spin population must be achieved. One would be tempted to think that it would be possible to produce this kind of spin population through the injection of spin-polarized electrons from direct contact between a magnetic metal and a semiconductor. Application of a potential difference across this interface should cause spin-polarized electrons from the magnetized metal to drift into the semiconductor and create a net spin-polarized electron population in that material. Unfortunately, there is a fundamental flaw in this reasoning that prevents this from occurring.

### 1.3.1 Conductivity Mismatch

Schmidt *et al.* [13] were the first to identify the fly in the ointment—the conductivity mismatch between the ferromagnetic metal (F) and semiconductor (S). Temporarily neglecting the Schottky barrier that forms between the two materials, consider a pictorial representation of the events that take place near the interface as a bias is applied (see Figure 1.3). The electric field sweeps away charge carriers of both spin types in S, freeing those states to

[3] See [1] for further details.

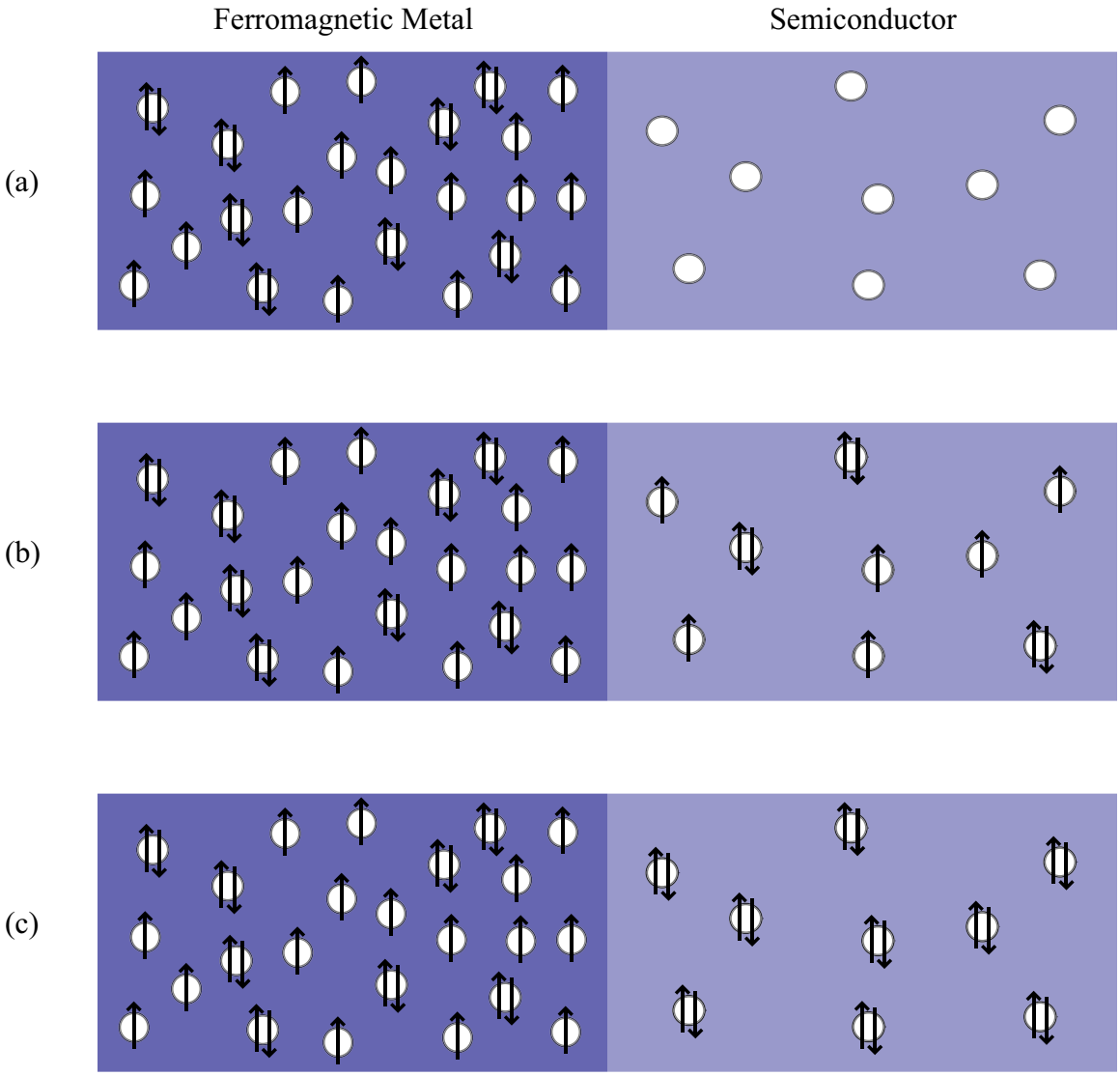


Figure 1.3: Pictorial representation of the conductivity mismatch problem: (a) the electric field sweeps carriers away from the interface in the semiconductor leaving behind empty states. (b) Empty states are occupied by carriers from the metal. (c) The chemical potential for each spin type quickly evens out in the semiconductor so that no net spin current traverses the metal-semiconductor interface

be occupied by carriers from F. Electrons from F drift into S with a net spin polarization determined by the magnetization of the metal. Majority spin electrons begin to occupy the available states, but because of the large difference in the densities of states for these two materials the chemical potential for adding a majority spin electron to S becomes much larger than for the minority spin electrons. As minority spin electrons travel across the interface, the chemical potentials for the two spin types even out and S is left with no net spin polarization.

To put more rigor behind these cartoon arguments, take a system as above with chemical potentials $\mu_{\eta,\mathrm{M}}$, conductivities $\sigma_{\eta,\mathrm{M}}$, and spin diffusion lengths $\Lambda_{\mathrm{M}}$, where $\eta = \uparrow, \downarrow$ corresponds to the two spin types and M = F, S indicates the material. Smith and Silver [14] have shown that for such a system, the spin currents, $j_{\eta,\mathrm{M}}$, and chemical potentials satisfy

$$j_{\eta,\mathrm{M}} = \sigma_{\eta,\mathrm{M}} \frac{\partial \mu_{\eta,\mathrm{M}}/e}{\partial x} \tag{1.4}$$

$$\frac{\partial^2 (\mu_{\uparrow,\mathrm{M}} - \mu_{\downarrow,\mathrm{M}})}{\partial x^2} = \frac{\mu_{\uparrow,\mathrm{M}} - \mu_{\downarrow,\mathrm{M}}}{\Lambda_{\mathrm{M}}^2}. \tag{1.5}$$

They observed that from these equations, the current polarization in the semiconductor is

$$P = \frac{j_\uparrow - j_\downarrow}{j_\uparrow + j_\downarrow} = \frac{(2\alpha_{\mathrm{F}} - 1) R_{\mathrm{F}} + (2\alpha_{\mathrm{S}} - 1) R_{\mathrm{S}} + (1/G_\uparrow) - (1/G_\downarrow)}{R_{\mathrm{F}} + R_{\mathrm{S}} + (1/G_\uparrow) + (1/G_\downarrow)} \tag{1.6}$$

$$R_{\mathrm{M}} = \frac{\Lambda_{\mathrm{M}}}{\sigma_{\mathrm{M}} \alpha_{\mathrm{M}} (1 - \alpha_{\mathrm{M}})} \tag{1.7}$$

$$\alpha_{\mathrm{M}} = \begin{cases} \frac{1}{1+\exp\left(-(\mu_\uparrow - \mu_\downarrow)/kT\right)}, & \mathrm{M} = \mathrm{S} \\ \text{constant}, & \mathrm{M} = \mathrm{F} \end{cases}, \tag{1.8}$$

where $G_\eta$ is the spin-dependent interface conductance. The indices indicating material type have been dropped in the expression for $P$ for clarity. $R_{\mathrm{M}}$ defines the relevant resistance for the problem—the bulk resistivity, $\rho_{\mathrm{M}} = 1/\sigma_{\mathrm{M}}$, of the material times the spin diffusion length. Since $\rho_{\mathrm{M}}$ lies in the range $10^{-3}$–$10^{8}\ \Omega\,\mathrm{cm}$ for semiconductors and in the range $10^{-8}$–$10^{-3}\ \Omega\,\mathrm{cm}$ for metals, $R_{\mathrm{S}}$ will dominate Equation 1.6 in the absence of interface resistance. If there is no difference in chemical potentials for the two spin types, as the cartoon model above argues, $\alpha_{\mathrm{S}}$ will be $1/2$ and no current polarization will be observed.

In order to overcome the conductivity mismatch problem (which, in essence, is really a density of states mismatch issue, as is made clear by the cartoon picture), several approaches can be taken. As is hinted by Equation 1.6, either the conductivity of the spin injector can be altered to match that of the semiconductor or some kind of spin-selective barrier can be introduced between the metal and semiconductor to promote the transport of one spin type.

### 1.3.2 Dilute Magnetic Semiconductors

Instead of contacting the semiconductor with a ferromagnetic metal, the contact could be made through another semiconductor—one with magnetic properties. This solves the conductivity mismatch problem by ensuring that the densities of states of the materials on both sides of the interface are comparable in magnitude. To obtain a semiconductor with magnetic character, the nonmagnetic material can be lightly doped with magnetic ions such as Mn [5, 6, 15]. These dilute magnetic semiconductors (DMS) have been shown to exhibit ferromagnetism, a property that is necessary if they are to be used in applications with zero applied external field.

The DMS approach has met with great success. Spin-polarized currents of 90% have been observed through this method [16]. Unfortunately, one major drawback lies in the fact that dilute magnetic semiconductors are only magnetic at low temperatures. Several DMS materials are predicted to have Curie temperatures above room temperature, but this has yet to be seen. The best Curie temperature demonstrated to date has been 110 K for the dilute magnetic semiconductor (Ga,Mn)As [17]. Unless the earth experiences an ice age like never before, this is clearly not suitable for room temperature use.

### 1.3.3 Spin-Selective Barriers

Rather than focusing on the conductivity of the ferromagnet, one can exploit the metal-semiconductor interface resistance. While normal ohmic contacts have not produced spin injection [18, 19], tunnel barriers can support the chemical potential difference needed for spin injection. The first clues of this came from Alvarado, who measured spin injection

from magnetic scanning tunneling microscope (STM) probe tips [20]. The vacuum tunnel barrier in STM may not find widespread commercial appeal, but the proof of concept has led to the measurement of spin injection from other tunnel barriers, including aluminum oxide and thin reverse biased Schottky barriers [21, 22].

Albrecht and Smith [23] have shown theoretically how a Schottky barrier operating in the tunneling regime works to allow spin-polarized transport. They found that tailoring the shape of the depletion region formed by the metal-semiconductor contact had a profound effect on the ability for this system to inject spins. A heavily doped region in the semiconductor near the interface was found to be favorable, but not so high that contact resistivity suffered greatly—resistivity needed to be kept high enough ($\sim 10^{-3}\,\Omega\,\mathrm{cm}$) to ensure that the barrier properties determined injection efficiency.

## 1.4 Measurement of Spin Polarization

Several methods for generating spin-polarized carrier currents have been discussed, but how is the spin polarization in the semiconductor actually measured? Spin injection from ferromagnetic metals is typically quantified by either electrical or optical measurements.

### 1.4.1 Electrical Measurement

Electrical measurements rely upon GMR (giant magnetoresistance) -type effects where injection into the semiconductor from one ferromagnetic contact is probed by a second ferromagnetic contact. Because of the spin-dependent properties of these contacts, the resistance will change depending on whether the the carrier spins in the semiconductor are either aligned or antialigned with the magnetization of the second contact.

This seems like a straightforward measurement, but questions about the validity of these electrical measurements have arisen. It is argued that the fringing fields from the magnetic contacts give rise to variations in measurement results due to the local Hall effect. Because of these concerns, optical characterization of spin injection has been the measurement technique of choice.

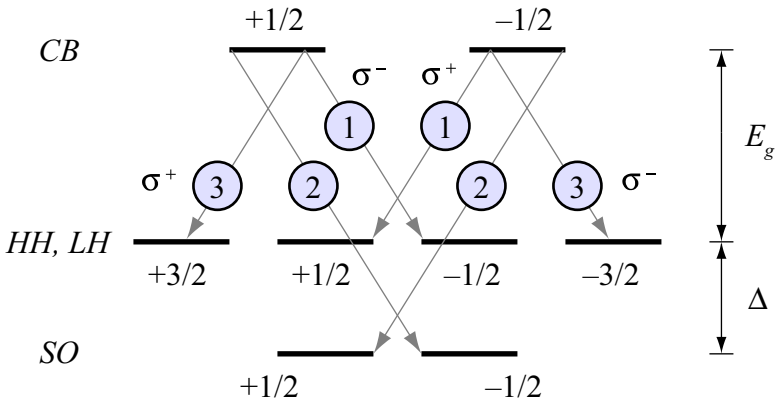


Figure 1.4: Allowed CB-VB transitions. Relative transition probabilities are indicated by the circled numbers. Adapted from [6].

### 1.4.2 Optical Measurement

The quantum mechanical selection rules dictate that not all conduction band (CB) to valence band (VB) transitions are allowed and that the ones that do occur do not do so with equal probability (see Figure 1.4). A $\left|\frac{1}{2}, +\frac{1}{2}\right\rangle_{CB}$ to ${}_{VB}\left\langle\frac{3}{2}, +\frac{3}{2}\right|$ transition, for example, is three times more likely to occur than a $\left|\frac{1}{2}, +\frac{1}{2}\right\rangle_{CB}$ to ${}_{VB}\left\langle\frac{3}{2}, -\frac{1}{2}\right|$ transition. The helicity of the light that is emitted along the spin direction in these transitions is also set by the selection rules. When the helicities are combined with the transition probabilities for CB to either heavy hole or light hole transitions, 50% circularly polarized light will be generated if all conduction electrons are spin-aligned. This fact allows for the measurement of the carrier spin population in a semiconductor and is the basis for the optical measurement of spin injection. Spin light emitting diodes (spin-LEDs) are *pn* or *p-i-n* semiconductor structures, often including a quantum well, that test the efficiency of various types of spin injectors (Figure 1.5) through this process.

Spin injection from a variety of different material systems have been probed by the use of spin-LEDs. Table 1.1 summarizes some of these results to date. As this table shows, injection results vary widely depending upon the injection method, measurement temperature, and semiconductor structure. The largest observed room temperature injection has been 30% for injection from Fe into (Al,Ga)As by Hanbiki, *et al.* using a Schottky contact as a tunnel barrier.

| Reference | Injecting Material | Barrier | Semiconductor | Temperature (K) | Efficiency (%) |
|---|---|---|---|---|---|
| Fiederling [16] | (Be,Mg,Zn)Se | - | (Al,Ga)As | 4 | 90 |
| Ohno [24] | (Ga,Mn)As | - | (In,Ga)As | 6 | 10 |
| Motsnyi [21] | Fe | $AlO_x$ | (Al,Ga)As | 80 | 9 |
| Hanbicki [22] | Fe | *n*+ Schottky Barrier | (Al,Ga)As | 300 | 30 |
| Ramsteiner [25] | MnAs | - | GaAs | 80 | 6 |
| Yoh [26] | Fe | - | *p*-InAs | 7 | 40 |
| Kioseoglou [27] | Fe | *n*+ Schottky Barrier | (Al,Ga)As (110) | 5 | 13 |
| Ramsteiner [28] | Fe | *n*+ Schottky Barrier | GaAs | 300 | 2 |

Table 1.1: Summary of spin injection measurements to date. The first two entries are the results for dilute magnetic semiconductor systems. The wide variation in these results, especially for injection from Fe into (Al,Ga)As, are cause for concern.

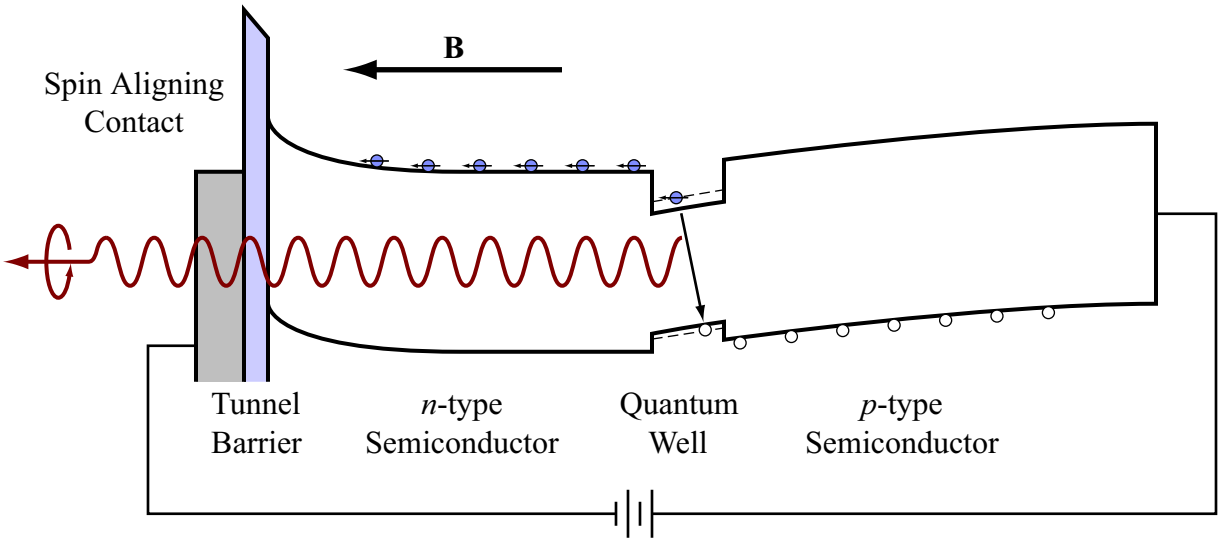


Figure 1.5: Spin-LED band diagram

Spin-LEDs, however, are not without their problems. The correlation between the spin injection efficiency and the the measured circular polarization of the electroluminescence is obfuscated by several factors:

1. Because the luminescence from the spin-LED is often viewed along the device growth direction, the carrier spins must be aligned along the same direction in order for the circular polarization to be measureable. This requires the use of large external magnetic fields to align the contact magnetization out of the plane of the thin film. Circular dichroism can cause a shift in the measured polarization signal. This is not expected for the materials under consideration, but measurements without the external field would be preferrable.

2. The electroluminescence is very often not emitted exactly in the magnetic field direction and will therefore not exactly have the helicity mentioned above. In fact, emission of light along a direction transverse to the spin orientation can result in the creation of linearly polarized rather than circularly polarized light. The finite solid angle occupied by the detection equipment in spin-LED polarization measurements implies that the measured polarization may be slightly lower than the actual value.

3. Reflections and refraction within the semiconductor structure add complexity and ob-

scure the relationship between spin polarization and photon polarization. Phase and amplitude changes during these events may seriously impact these measurements.

Solving the first of these problems can be done by either using the natural in-plane magnetization of the contact material, or by employing a spin aligning contact with an out-of-plane easy magnetization axis (perpendicular magnet). Using the in-plane magnetization would require measurement of side emission from the LEDs while the use of a perpendicular magnet hinges upon the development of such a material with good interfacial properties with the chosen semiconductor system.

Attacking the second and third problems from a theoretical standpoint can provide clarity. Assuming that spin-polarized carriers have, in fact, been injected into the LED structure, the polarization dependence of the electroluminescence on the spin state of these carriers and the propagation direction of the photon resulting from electron-hole recombination can be quantified. The effects of reflection and refraction throughout the device structure can also be modeled.

## 1.5 Thesis Outline

The questions of the legitimacy of spin-LED injection measurements are valid and these issues must be addressed. In addition, the variance of the spin-LED injection measurements in the literature is troubling. This thesis seeks to shed light on each of these problems by theoretical as well as experimental means.

Chapter 2 addresses the issues of photon polarization and the effects of reflection and refraction within the spin-LED. A Monte Carlo ray-tracing simulation incorporating these effects is discussed and the question of side emission as a viable measurement technique is considered.

Design considerations for and the fabrication of a spin-LED are the subject of Chapter 1. The design includes simulation of the electrical characteristics of the spin-LED as well as discussion of appropriate material choice. The section of fabrication focuses on the method by which the spin aligning contacts were formed and the wafer processed.

Characterization of these devices is covered in Chapter 4. The growth of the semiconductor structure as well as the contact materials is evaluated. Magnetic, electrical, and optical characterization of the devices is also discussed.

Finally, Chapter 5 details the experimental setup used for spin injection measurement. The results are compared to similar work and the effectiveness of the tunnel barrier for these samples is assessed.

# References


[1] S. M. Sze, *Physics of Semiconductor Devices*, 2nd ed. (John Wiley & Sons, Inc., New York, YEAR).

[2] G. E. Moore, Electronics **38**, (1965).

[3] Odlyzko, Technical report, AT&T Bell Laboratories (unpublished).

[4] S. Datta and B. Das, Appl. Phys. Lett. **56**, 665 (1990).

[5] S. A. Wolf, D. D. Awschalom, R. A. Buhrman, J. M. Daughton, S. von Molnar, M. L. Roukes, A. Y. Chtchelkanova, and D. M. Treger, Science **294**, 1488 (2001).

[6] I. Zutic, J. Fabian, and S. Das Sarma, Rev. Mod. Phys. **76**, 323 (2004).

[7] H. Akinaga and H. Ohno, IEEE Trans. Nanotechnol. **1**, 19 (2002).

[8] J. De Boeck, W. Van Roy, J. Das, V. Motsnyi, Z. Liu, L. Lagae, H. Boeve, K. Dessein, and G. Borghs, Semicond. Sci. Technol. **17**, 342 (2002).

[9] G. A. Prinz, Science **282**, 1660 (1998).

[10] S. Bandyopadhyay, Superlattices Microstruct. **37**, 77 (2005).

[11] A. E. Popescu and R. Ionicioiu, Phys. Rev. B **69**, 245422 (2004).

[12] P. W. Shor, SIAM Rev. **41**, 303 (1999).

[13] G. Schmidt, D. Ferrand, L. W. Molenkamp, A. T. Filip, and B. J. van Wees, Phys. Rev. B **62**, R4790 (2000).

[14] D. L. Smith and R. N. Silver, Phys. Rev. B **64**, 045323 (2001).

[15] *Semiconductor Spintronics and Quantum Computation*, edited by D. D. Awschalom, D. Loss, and N. Samarth (Springer-Verlag, New York, 2002).

[16] R. Fiederling, M. Keim, G. Reuscher, W. Ossau, G. Schmidt, A. Waag, and L. W. Molenkamp, Nature **402**, 787 (1999).

[17] H. Ohno, A. Shen, F. Matsukura, A. Oiwa, A. Endo, S. Katsumoto, and Y. Iye, Appl. Phys. Lett. **69**, 363 (1996).

[18] S. Gardelis, C. G. Smith, C. H. W. Barnes, E. H. Linfield, and D. A. Ritchie, Phys. Rev. B **60**, 7764 (1999).

[19] F. G. Monzon and M. L. Roukes, J. Magn. Magn. Mater. **199**, 632 (1999).

[20] S. F. Alvarado and P. Renaud, Phys. Rev. Lett. **68**, 1387 (1992).

[21] V. F. Motsnyi, P. Van Dorpe, W. Van Roy, E. Goovaerts, V. I. Safarov, G. Borghs, and J. De Boeck, Phys. Rev. B **68**, 245319 (2003).

[22] A. T. Hanbicki, B. T. Jonker, G. Itskos, G. Kioseoglou, and A. Petrou, Appl. Phys. Lett. **80**, 1240 (2002).

[23] J. D. Albrecht and D. L. Smith, Phys. Rev. B **68**, 035340 (2003).

[24] Y. Ohno, D. K. Young, B. Beschoten, F. Matsukura, H. Ohno, and D. D. Awschalom, Nature **402**, 790 (1999).

[25] M. Ramsteiner, J. Supercond. **16**, 661 (2003).

[26] K. Yoh, H. Ohno, Y. Katano, K. Sueoka, K. Mukasa, and M. E. Ramsteiner, Semicond. Sci. Technol. **19**, S386 (2004).

[27] G. Kioseoglou, A. T. Hanbicki, J. M. Sullivan, O. M. J. van 't Erve, C. H. Li, S. C. Erwin, R. Mallory, M. Yasar, A. Petrou, and B. T. Jonker, Nat. Mater. **3**, 799 (2004).

[28] A. Ramsteiner, H. J. Zhu, H. P. Schonherr, and K. H. Ploog, Physica E **13**, 529 (2002).

# Chapter 2 Monte Carlo Simulation of the Spin-LED

## 2.1 Introduction

As described in Section 1.2, the spin-LED structure has been used extensively to study spin-polarized carrier injection into semiconductors.[1] The circular polarization of the electroluminescence from these devices is related back to the spin polarization of the injected carrier population through the quantum mechanical selection rules. These optical measurements are more trustworthy than electrical measurements, but the accuracy of the correlation between the circular polarization of the emitted light and the spin polarization of the electron population in the LED is not without question.

Light is not emitted directly from a spin-LED. There are several notable interfaces within these devices (metal-semiconductor contacts, semiconductor heterojunctions, and the semiconductor-air interface) and reflection and refraction at these interfaces can bring about significant changes in polarization. Is the polarization of the light emitted from these devices closely correlated to the initial polarization of the photons created in the electron-hole recombination process? Or does the possibility for multiple internal reflection and refraction events within the spin-LED structure drastically alter the electroluminescence polarization properties?

Reflection and refraction are one consideration. Measurements of spin injection from ferromagnetic metals also typically require large external magnetic fields to align the magnetization of the contact to a direction appropriate for vertical emission measurements. This is done because the shape anisotropy of a magnetic metal forces the easy axis for magnetization to lie in the plane of the contact. Because the electroluminescence (EL) generated in these devices is circularly polarized along the direction of the electron spin, the Faraday

[1] See Table 1.1.

or Kerr geometries often used in these experiments force the use of an external magnet to align the contact magnetization along the hard axis. One possible method for overcoming the need for the large external field is to use side emission from LED structures.

To determine the extent of these effects, a Monte Carlo computer simulation was created using a ray-tracing algorithm to track photon polarization and propagation through the device structure. Ray-tracing simulators have been developed to aid in the design of efficient LED structures [1, 2], but no commercial application exists that tracks photon polarization in a device composed of arbitrary layers. Poldiode, a Monte Carlo ray-tracing LED simulator written in C++, performs this task.

## 2.2 Physical Model and Flow Chart for Poldiode

Theoretical models for the injection of spin-polarized carriers into semiconductor materials have been developed elsewhere [3, 4]. The aim of of this simulation, then, is not to model the injection process itself, but to determine the relationship between the spin state of an electron involved in band-to-band recombination and the polarization of the photon that is eventually emitted from the spin-LED.

In the simulation, a configuration file is first read that determines the number of photons to generate, the energy of these photons, the distance from the LED to the photodetector (assumed to have a quantum efficiency of 1), the spin orientation of the electrons injected into the device, and valence bands to which the electrons will transition. The LED structure is then defined through another configuration file as a circular mesa structure composed of arbitrary (semiconductor, contact metal, or insulator) material layers. The radius, height, and complex index of refraction, $\tilde{n}$, for each layer is given, and a flag sets the active region of the device where the photons are to be generated. The program then performs the work of creating the photons and propagating them through the device until they are either transmitted into the air surrounding the LED or absorbed back into the device material. Figure 2.1 depicts the flow chart for this portion of the simulation. Because of the independent nature of each of the photons, Poldiode was written as a multithreaded application to decrease computation time. The following sections cover the details of these calculations.

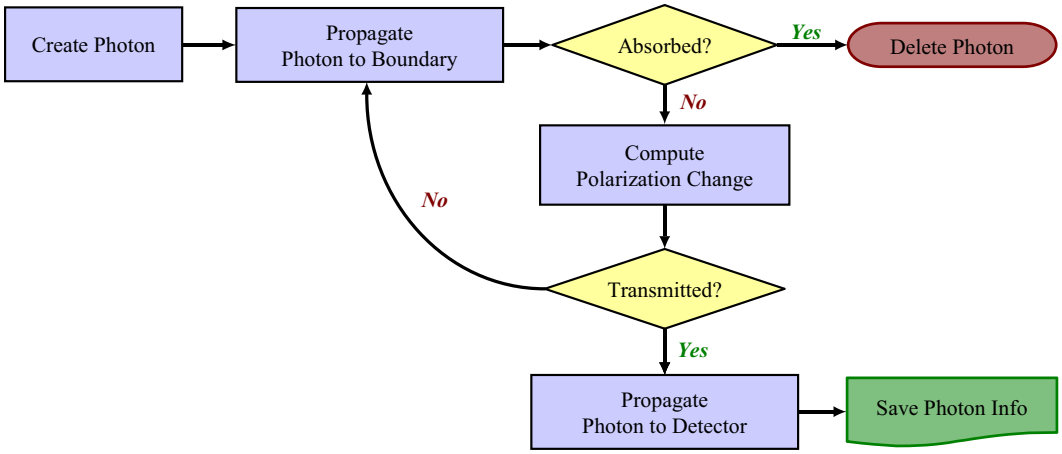


Figure 2.1:
Flow chart of the ray-tracing algorithm for Poldiode. Because each photon is independent from the next, a multithreaded application was written to speed computation time. The simulation was performed on a Silicon Graphics Origin 2000.

### 2.2.1 Photon Generation

Photon generation is a result of radiative electron-hole recombination in the active layer of the device. This transition may occur between the spin-aligned electron in the conduction band and one of several available valence bands (see Figure 2.2). Because of the spin characters of the conduction and valence bands as well as the energy differences between the heavy-hole (HH), light-hole (LH), and split-off (SO) bands, the probabilities for an electron of a given spin type to transition to the HH, LH, or SO bands are different.

For most bulk zincblende III–V semiconductors, the HH and LH band maxima are equal at the Γ-point. Thus, for a *p-n* junction diode, the relative transition probabilities for these two bands are completely determined by the spin state of the electron in the conduction band. These bands are separated in quantum well structures, however, because of the dependence of the well confinement upon the effective masses of the electrons and holes. For an infinitely deep well, the energy energy difference between the CB well state and the VB well state is given by

$$E_{\hbar\omega} = E_g + \frac{\hbar^2\pi^2 n^2}{2m_0 d^2}\left[\frac{1}{m_e} + \frac{1}{m_h}\right], \tag{2.1}$$

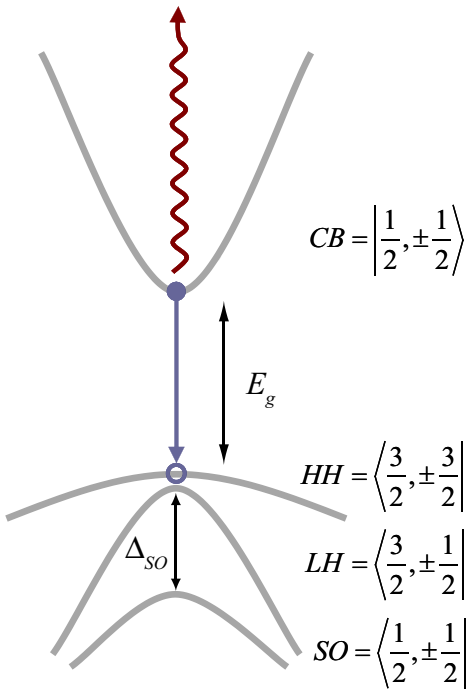


Figure 2.2: Radiative conduction band to valence band transition in a semiconductor. The transition probabilities are determined by the energy difference between the conduction band and various valence bands as well as the spin orientation of the electron involved in the recombination process.

where $E_g$ is the semiconductor bandgap, $n$ is index of the quantum well energy level under consideration, $m_0$ is the free electron mass, $d$ is the width of the well, and $m_e$ and $m_h$ are the electron and hole effective masses. For GaAs, $m_e = 0.067$, $m_{LH} = 0.082$, $m_{HH} = 0.45$, and $m_{SO} = 0.17$. However, because $\Delta_{SO} = 0.34\,\text{eV}$, transitions to the split-off band are much less likely and can be spectrally resolved from CB to LH or CB to HH transitions. These transitions are therefore neglected in this simulation.

These differences between bulk zincblende *p-n* junction diodes and quantum well structures cause the radiation patterns and photon polarization distributions to be different. The cases of CB to LH, HH, and LH+HH transitions will therefore be treated separately as photon generation is discussed.

#### 2.2.1.1 Initial Photon Location

In generating a photon, the first step is to determine the location of the electron-hole recombination event. These events occur within the active region of the LED, which is set by the device configuration file. For a quantum well LED structure, the active region corresponds to the quantum well layer. For a *p-n* homojunction diode, it would be the depletion region of the device. Photons are uniformly generated throughout the volume of this region. No weighting is given to this distribution because current spreading in the spin-aligning contact layer should provide a uniform current density passing through the mesa structure.

#### 2.2.1.2 Propagation Direction Selection

Once a location has been chosen at which the photon will be generated, the direction of propagation and polarization state of the photon must be set. Cartoxía [5] developed the formalism to calculate these quantities based on time-dependent perturbation theory. Using this method, the propagation direction may first be selected and then the polarization may subsequently be chosen based on that information. For the coordinate system shown in Figure 2.3, the propagation direction, $\hat{\mathbf{k}}$, is determined by a probability distribution function that depends on the set of valence bands to which the electron may transition. These

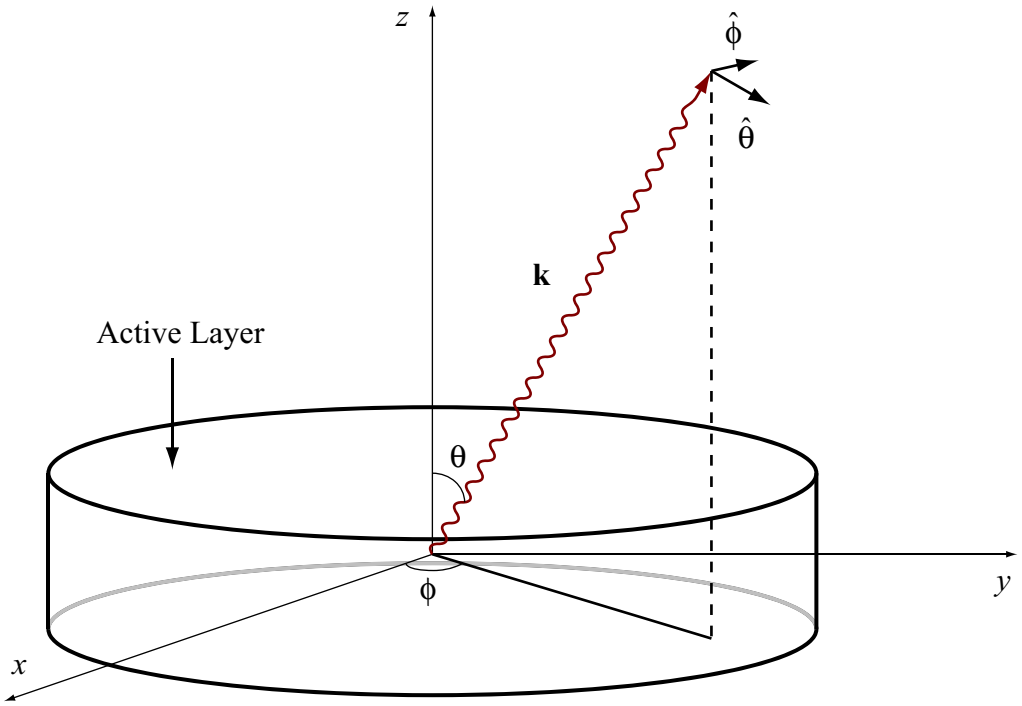


Figure 2.3: Coordinate system used in Poldiode. The polarization of each photon is given in the $\hat{\theta}$, $\hat{\phi}$ basis.

probability distribution functions are

$$p_{HH}(\theta,\phi) = \frac{3}{16\pi}\left(1+\cos^2\theta\right) \tag{2.2}$$

$$p_{LH}(\theta,\phi) = \frac{1}{16\pi}\left(5-3\cos^2\theta\right) \tag{2.3}$$

$$p_{LH+HH}(\theta,\phi) = \frac{1}{4\pi}. \tag{2.4}$$

The angles $\theta$ and $\phi$ completely determine $\hat{\mathbf{k}}$. Note that these distribution functions are independent of the angle $\phi$ because of the azimuthal symmetry present in the system.

In order to generate this distribution two pseudorandom numbers, $r_\theta$ and $r_\phi$ are needed. However, the random number generator uniformly generates $r_\theta$ and $r_\phi$ on the interval [0, 1]. How can a uniform distribution be transformed into an arbitrary probability distribution? To do so, the cumulative probability distribution function, $f(\theta,\phi)$, is necessary [6]. For an azimuthally symmetric probability distribution function $p(\theta,\phi) \equiv p(\theta)$ in spherical

coordinates, $f(\theta,\phi) = f^{\theta}(\theta) f^{\phi}(\phi)$. $f^{\theta}(\theta)$ is given by

$$f^{\theta}(\theta) = \int_{-1}^{\cos\theta} \int_{0}^{2\pi} p(\theta',\phi')\, d\phi'\, d\cos\theta'. \tag{2.5}$$

Since $f^{\theta}(\theta) \in [0,1]$, the same interval as $r_\theta$, $f^{\theta}(\theta) \equiv r_\theta$ can be inverted to give $\theta$ (or $\cos\theta$, which is more convenient for this problem) in terms of $r_\theta$. For the probability distributions in equations 2.2–2.4, the cumulative probability distributions are

$$f^{\theta}_{HH}(\theta) = \frac{3}{8}\left(\frac{4}{3} + \cos\theta + \frac{1}{3}\cos^3\theta\right) \tag{2.6}$$

$$f^{\theta}_{LH}(\theta) = \frac{1}{8}\left(4 + 5\cos\theta - \cos^3\theta\right) \tag{2.7}$$

$$f^{\theta}_{LH+HH}(\theta) = \frac{1}{2}(1 + \cos\theta) \tag{2.8}$$

and the angles $\theta$ for these three cases in terms of $r_\theta$ are

$$\cos\theta_{HH} = \frac{1 - \left(2 - 4r_\theta + \sqrt{5 + 16r_\theta(r_\theta - 1)}\right)^{2/3}}{\left(2 - 4r_\theta + \sqrt{5 + 16r_\theta(r_\theta - 1)}\right)^{1/3}} \tag{2.9}$$

$$\cos\theta_{LH} = \frac{5(-3)^{2/3} - (-3)^{1/3}\left(18 - 36r_\theta + \sqrt{1296r_\theta(r_\theta - 1) - 51}\right)^{2/3}}{3\left(18 - 36r_\theta + \sqrt{1296r_\theta(r_\theta - 1) - 51}\right)^{1/3}} \tag{2.10}$$

$$\cos\theta_{LH+HH} = 2r_\theta - 1, \tag{2.11}$$

where the appropriate roots of the cubic equation have been chosen such that $\cos\theta \in [-1, 1]$. For all three cases, the azimuthal angle is given by

$$\phi = 2\pi r_\phi. \tag{2.12}$$

#### 2.2.1.3 Photon Polarization

Once the initial propagation direction has been chosen, the polarization state of the photon may be set. The process for determining this information is as follows (the details of this calculation are covered more extensively in Reference [5]:

1. The spin orientation, **s**, of the conduction electron is set (done in the configuration

| | $\lvert x\rangle\left\lvert -\frac{1}{2}\right\rangle$ | $\lvert x\rangle\left\lvert +\frac{1}{2}\right\rangle$ | $\lvert y\rangle\left\lvert -\frac{1}{2}\right\rangle$ | $\lvert y\rangle\left\lvert +\frac{1}{2}\right\rangle$ | $\lvert z\rangle\left\lvert \frac{1}{2}, -\frac{1}{2}\right\rangle$ | $\lvert z\rangle\left\lvert +\frac{1}{2}\right\rangle$ |
|---|---|---|---|---|---|---|
| $_{SO}\left\langle -\frac{1}{2}\right\rvert$ | $0$ | $-i/\sqrt{3}$ | $0$ | $-1/\sqrt{3}$ | $i/\sqrt{3}$ | $0$ |
| $_{SO}\left\langle +\frac{1}{2}\right\rvert$ | $-i/\sqrt{3}$ | $0$ | $1/\sqrt{3}$ | $0$ | $0$ | $-i/\sqrt{3}$ |
| $_{HH}\left\langle -\frac{3}{2}\right\rvert$ | $-i/\sqrt{2}$ | $0$ | $-1/\sqrt{2}$ | $0$ | $0$ | $0$ |
| $_{HH}\left\langle -\frac{1}{2}\right\rvert$ | $0$ | $i/\sqrt{6}$ | $0$ | $1/\sqrt{6}$ | $i\sqrt{2/3}$ | $0$ |
| $_{LH}\left\langle +\frac{1}{2}\right\rvert$ | $-i/\sqrt{6}$ | $0$ | $1/\sqrt{6}$ | $0$ | $0$ | $i\sqrt{2/3}$ |
| $_{LH}\left\langle +\frac{3}{2}\right\rvert$ | $0$ | $i/\sqrt{2}$ | $0$ | $-1/\sqrt{2}$ | $0$ | $0$ |

Table 2.1: Clebsch-Gordan coefficients used to calculate photon polarization for bulk zincblendes. The position ket denotes the direction of the relevant component of the momentum operator in the electric dipole term of the Hamiltonian $H = H_0 - \frac{e}{m_0}\mathbf{P}\cdot\mathbf{A}$.

| | $\lvert x\rangle\left\lvert -\frac{1}{2}\right\rangle$ | $\lvert x\rangle\left\lvert +\frac{1}{2}\right\rangle$ | $\lvert y\rangle\left\lvert -\frac{1}{2}\right\rangle$ | $\lvert y\rangle\left\lvert +\frac{1}{2}\right\rangle$ |
|---|---|---|---|---|
| $_{HH}\left\langle -\frac{1}{2}\right\rvert$ | $0$ | $i/\sqrt{2}$ | $0$ | $-1/\sqrt{2}$ |
| $_{HH}\left\langle +\frac{1}{2}\right\rvert$ | $i/\sqrt{2}$ | $0$ | $1/\sqrt{2}$ | $0$ |
| $_{LH}\left\langle -\frac{1}{2}\right\rvert$ | $0$ | $i/\sqrt{2}$ | $0$ | $1/\sqrt{2}$ |
| $_{LH}\left\langle +\frac{1}{2}\right\rvert$ | $i/\sqrt{2}$ | $0$ | $-1/\sqrt{2}$ | $0$ |

Table 2.2: Clebsch-Gordan coefficients used to calculate photon polarization for quantum well structures.

file) and the angle, $\cos\theta_{sk} = (\mathbf{s}\cdot\mathbf{k}) / |\mathbf{s}|\,|\mathbf{k}|$, between the electron spin and the photon propagation direction is calculated. The components of the electron's spinor, $\sigma = a\,|\uparrow\rangle + b\,|\downarrow\rangle$, along $z$ are also determined at this time.

2. The valence band to which the electron recombines is chosen probabilistically. These transition probabilities depend upon the set of valence bands to which the electron may transition, the spin character of each of these bands, the polar angle of the emitted photon, and the components of the electron's spinor.

3. The components of the photon's electric field are calculated in the $\hat{\theta}$, $\hat{\phi}$ basis (see Figure 2.3) for spin-up ($E_\theta^\uparrow$, $E_\phi^\uparrow$) and spin-down ($E_\theta^\downarrow$, $E_\phi^\downarrow$) conduction electrons. The strength of each of these terms is determined by the photon's propagation direction as well as the Clebsch-Gordan coefficients listed in Tables 2.1 and 2.2.[2]

[2]The Clebsch-Gordan coefficients relate to the symmetry properties of the energy bands involved in recombination and are tabulated in Reference [7].

4. These electric field components are added together in proportion to the conduction electron's spinor to give the photon polarization

$$\mathbf{E}_\gamma = \left(aE_\theta^\uparrow + bE_\theta^\downarrow\right)\hat{\theta} + \left(aE_\phi^\uparrow + bE_\phi^\downarrow\right)\hat{\phi}. \tag{2.13}$$

The polarization state of light is best described by using quantities that are quadratic in the field because intensity is easier to measure than amplitude. One method of characterizing the polarization state of light uses the four Stokes parameters, $I$, $Q$, $U$, and $V$. These describe the intensity, two states of linear polarization, and the circular polarization state, respectively (see Appendix A for a review of these quantities). The normalized Stokes parameters, $Q/I$, $U/I$, and $V/I$ range from $-1$ to 1 and give a better measure of the polarization state of the light.

For a conduction electron in the $|1/2, +1/2\rangle$ state (with quantization along the $z$-axis), the procedure described in this section will produce light with the following polarization properties:

Bulk Zincblende

$$\frac{Q}{I} = 0 \tag{2.14}$$
$$\frac{U}{I} = 0 \tag{2.15}$$
$$\frac{V}{I} = -\frac{1}{2}\cos\theta \tag{2.16}$$

Quantum Well with Heavy-Hole Character

$$\frac{Q}{I} = \frac{1-\cos^2\theta}{1+\cos^2\theta} \tag{2.17}$$
$$\frac{U}{I} = 0 \tag{2.18}$$
$$\frac{V}{I} = -\frac{2\cos\theta}{1+\cos^2\theta} \tag{2.19}$$

Quantum Well with Light-Hole Character

$$\frac{Q}{I} = 1 - \frac{2}{5 - 3\cos^2\theta} \tag{2.20}$$

$$\frac{U}{I} = 0 \tag{2.21}$$

$$\frac{V}{I} = \frac{2\cos\theta}{5 - 3\cos^2\theta} \tag{2.22}$$

Figures 2.4 and 2.5 confirm that the simulation does indeed produce the correct polarization given for the case of bulk zincblende and quantum well spin-LEDs.

### 2.2.2 Photon Propagation

Once the photon has been generated and its polarization and propagation direction set, the location of the intersection of the photon's **k** vector and the boundaries of the current device layer is calculated. The length, $L$, of the path connecting that point to the photon's current location is calculated and the photon's position is updated to the location of the intersection.

If the material is absorbing, there is some probability that the photon will be lost while traversing this path. That probability is given by

$$P = 1 - e^{-\alpha L} \tag{2.23}$$

$$\alpha \equiv \frac{4\pi k}{\lambda}, \tag{2.24}$$

where $\lambda$ is the wavelength of the photon and $k = \Im[\tilde{n}]$ is the absorption constant [8]. If it is determined that the photon was absorbed, the photon's state is discarded and the simulation proceeds to generate the next photon. Photon recycling is not considered because absorption primarily occurs in the semiconductor substrate for the quantum well structures that are typically used for spin injection measurements. Radiation generated from electron-hole recombination in the substrate can easily be spectrally resolved from quantum well radiation.

### 2.2.3 Polarization Changes at Interfaces

Changes in photon polarization occur at interfaces between dissimilar materials due to differences in the optical properties of those materials (see Figure 2.6). For an incident

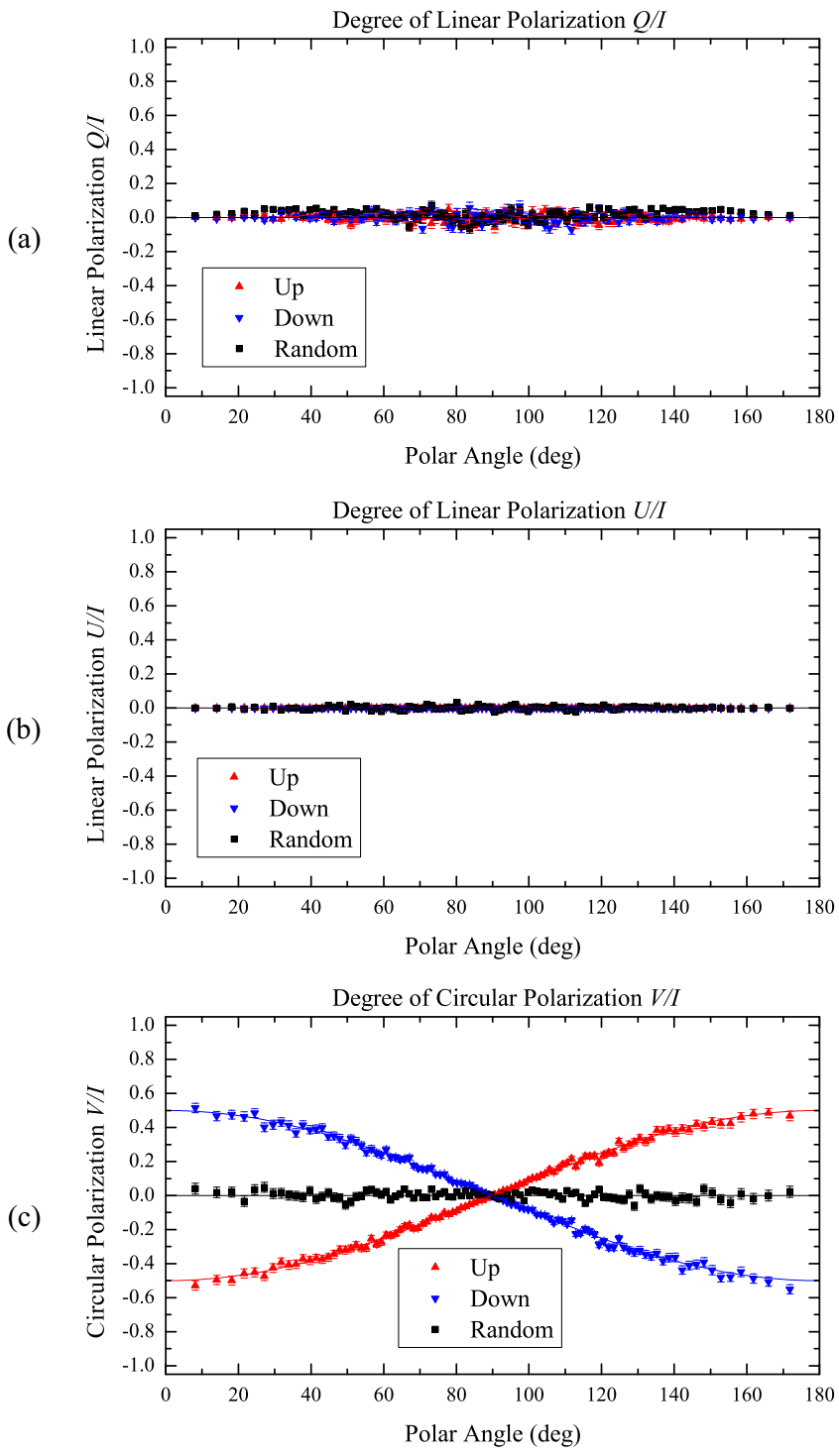


Figure 2.4: Polarization of radiation from a bulk zincblende semiconductor as calculated by Poldiode. The three sets of data in each plot show the simulation results for different electron spin orientations. The solid curves indicate theoretically expected values. (a) and (b) indicate that no linear polarization is generated in bulk devices while (c) shows a difference in circular polarization for spin-up and spin-down electrons. The maximum value of $V/I$ in this case is 1/2.

(a)

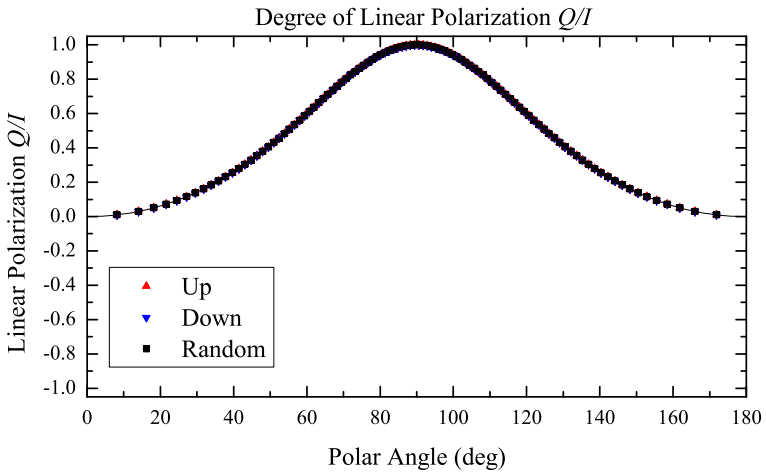


(b)

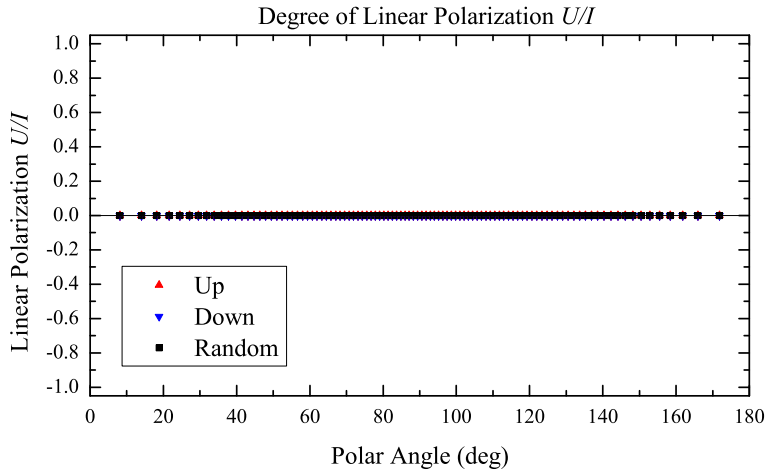


(c)

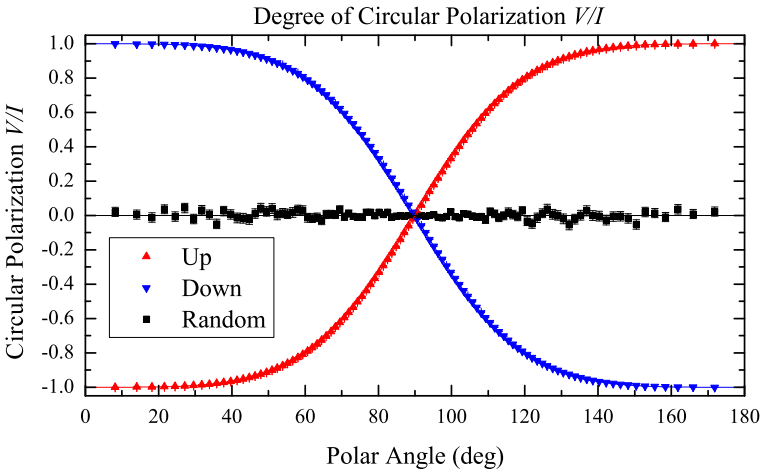


Figure 2.5: Polarization of radiation from a quantum well spin-LED structure. Three different initial electron spin orientations are shown. The theoretical values from Equations 2.17–2.19 are indicated by the solid curves. (a) Nonzero linear polarization $Q/I$ can be measured, but is independent of electron spin. (b) No linear polarization $U/I$. (c) Circular polarization takes on its maximum value of 1 and is different for the two electron spin orientations.

wave with electric field

$$\mathbf{E} = \left[\mathbf{E}_{\|} e^{-i\delta_{\|}} + \mathbf{E}_{\perp} e^{-i\delta_{\perp}}\right] e^{-i(\mathbf{k}\cdot\mathbf{x}-\omega t)}, \tag{2.25}$$

where $\mathbf{E}_{\|}$and $\mathbf{E}_{\perp}$, respectively, are the components of the electric field parallel and perpendicular to the plane of incidence. If the reflection and refraction is completely specular,[3] the Fresnel Equations give the magnitudes of the transmitted, $\mathbf{E}'$, and reflected, $\mathbf{E}''$, waves. For $\mathbf{E}_{\|}$ these are [9]

$$\left[\frac{E'}{E}\right]_{\|} = \frac{2\tilde{n}\tilde{n}'\cos\theta_i}{\frac{\mu}{\mu'}\tilde{n}'^2\cos\theta_i + \tilde{n}\sqrt{\tilde{n}'^2 - \tilde{n}^2\sin^2\theta_i}} \tag{2.26}$$

$$\left[\frac{E''}{E}\right]_{\|} = \frac{\frac{\mu}{\mu'}\tilde{n}'^2\cos\theta_i - \tilde{n}\sqrt{\tilde{n}'^2 - \tilde{n}^2\sin^2\theta_i}}{\frac{\mu}{\mu'}\tilde{n}'^2\cos\theta_i + \tilde{n}\sqrt{\tilde{n}'^2 - \tilde{n}^2\sin^2\theta_i}}, \tag{2.27}$$

whereas for $\mathbf{E}_{\perp}$ they are

$$\left[\frac{E'}{E}\right]_{\perp} = \frac{2\tilde{n}\cos\theta_i}{\tilde{n}\cos\theta_i + \frac{\mu}{\mu'}\sqrt{\tilde{n}'^2 - \tilde{n}^2\sin^2\theta_i}} \tag{2.28}$$

$$\left[\frac{E''}{E}\right]_{\perp} = \frac{\tilde{n}\cos\theta_i - \frac{\mu}{\mu'}\sqrt{\tilde{n}'^2 - \tilde{n}^2\sin^2\theta_i}}{\tilde{n}\cos\theta_i + \frac{\mu}{\mu'}\sqrt{\tilde{n}'^2 - \tilde{n}^2\sin^2\theta_i}}. \tag{2.29}$$

Once the amplitudes of the reflected and transmitted waves have been calculated, the reflection and transmission probabilities can be calculated using the time-averaged normal component of the Poynting vector:

$$\mathbf{S}\cdot\mathbf{n} = \frac{1}{2}\Re\left[\mathbf{n}\cdot(\mathbf{E}\times\mathbf{H}^*)\right], \tag{2.30}$$

where $\mathbf{n}$ is the unit vector normal to the interface. Since $\theta_i = \theta_r$, the reflection probability is simply given by

$$P = \frac{|E''|^2}{|E|^2}. \tag{2.31}$$

The photon propagation direction and polarization information are updated once it is deter-

[3] Specular reflection is a reasonable assumption given the use of MBE grown material and good lithography techniques for device fabrication.

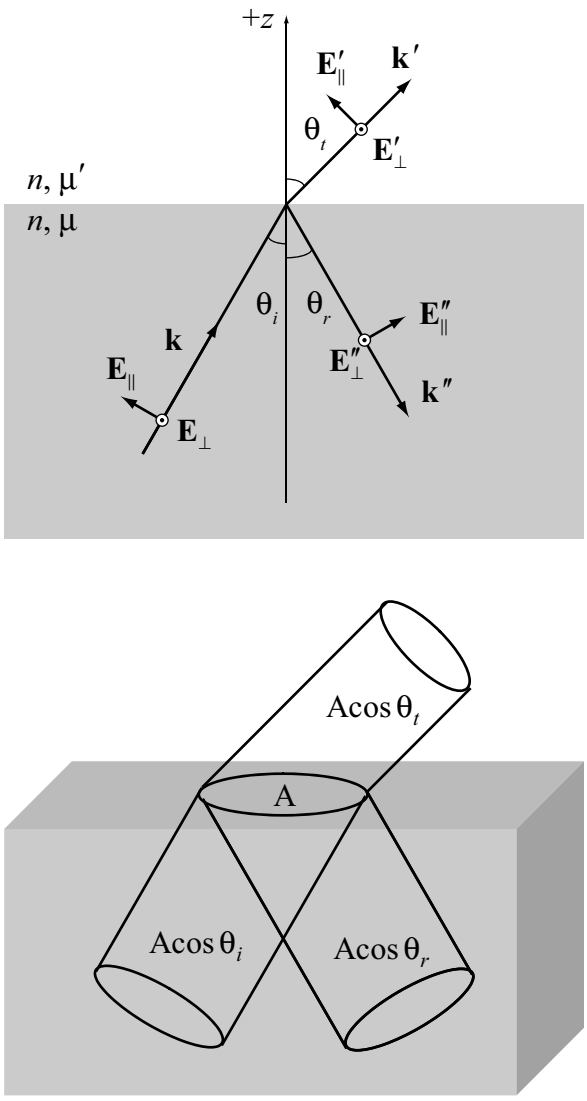


Figure 2.6: Polarization change at interface and transmission probability. (a) The incident wave, **k**, is partially reflected, **k**′, and partially transmitted, **k**′′. (b) The transmission probability is determined by incident, reflected, and transmitted power flux normal to the interface

mined if the photon has been reflected or transmitted.

One complication in this calculation comes about because the polarization state of the photon must be broken down into components that are parallel and perpendicular to the plane of incidence. Considering the possibility of a photon striking the circular side walls of the mesa, this is a nontrivial issue. To overcome this obstacle, the coordinate system in which the photon's polarization is expressed is transformed by use of the Euler angles into a coordinate system in which equations 2.26–2.29 can be applied. If $\mathbf{x}$ is a vector in the original coordinate system and $\mathbf{x}'$ is the corresponding vector in the new system, the transformation from $\mathbf{x}$ to $\mathbf{x}'$ is given by [10]

$$\mathbf{x}' = \lambda \mathbf{x} \tag{2.32}$$

where

$$\lambda = \begin{pmatrix} \cos\gamma\cos\beta - \cos\alpha\sin\beta\sin\gamma & \cos\gamma\sin\beta + \cos\alpha\cos\beta\sin\gamma & \sin\gamma\sin\alpha \\ -\sin\gamma\cos\beta - \cos\alpha\sin\beta\cos\psi & -\sin\gamma\sin\beta + \cos\alpha\cos\beta\cos\gamma & \cos\gamma\sin\alpha \\ \sin\alpha\sin\beta & -\sin\alpha\cos\beta & \cos\alpha \end{pmatrix} \tag{2.33}$$

and $\alpha$, $\beta$, and $\gamma$ are angles chosen such that $\mathbf{E}_\perp \parallel \hat{\phi}'$ and $\mathbf{E}_\parallel \parallel \hat{\theta}'$.

After the probability for transmission or reflection has been calculated and the photon's polarization information updated, the coordinate system is transformed back to its original state through the transformation $\lambda^{-1}$.

### 2.2.4 Information Recorded by Poldiode

When a photon is transmitted from the diode structure into the surrounding air, it is then propagated to the position of an imaginary photodetector where information about that photon is collected. This information includes

- the position at which the photon is detected
- the interface (side, top, or bottom) from which the photon was emitted

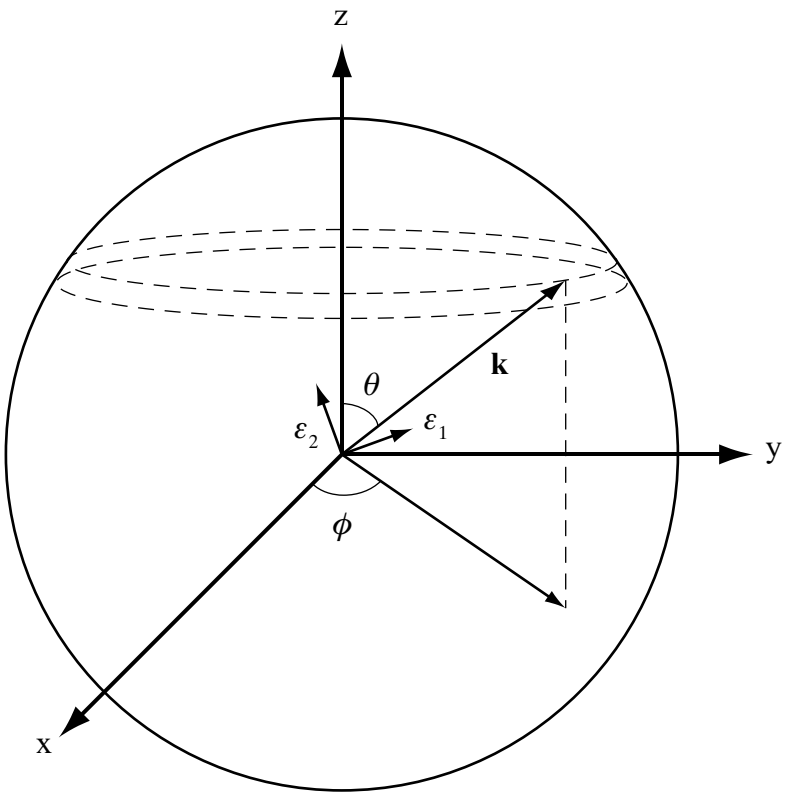


Figure 2.7: Angular histogram binning for the spin-LED simulation. Azimuthal symmetry allows for integration over $\phi$ to improve statistics.

- the number of internal reflections the photon experienced
- the polarization information for each photon

The polarization information that is recorded for each photon is given by the four normalized Stokes parameters described in §2.2.1.3 and Appendix A.

After all of the photons have been generated, the data are binned and ensemble averages are calculated for each of the normalized Stokes parameters. Because the detector subtends a unit of solid angle $d\Omega = \sin\theta d\theta d\phi = -d\cos\theta d\phi$ (see Figure 2.7), the data are binned in the polar angle by $d\cos\theta$. The circular LED is placed at the origin of the coordinate system so that azimuthal symmetry allows for integration over $\phi$ to improve statistics.

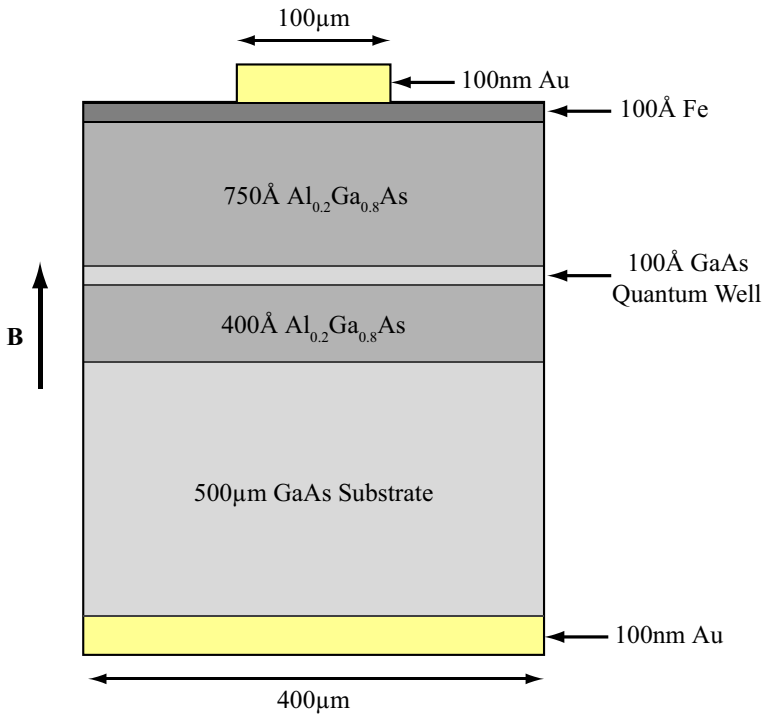


Figure 2.8: GaAs/$Al_{0.2}Ga_{0.8}As$ quantum well structure used for Poldiode. A 100 Å Fe spin-aligning contact was included to determine its effect on photon polarization.

## 2.3 Quantum Well Simulation

Quantum well spin-LED structures are used extensively to study electrical injection into semiconductors. This device design is preferable to bulk *p-n* junction diodes because the quantum mechanical selection rules that govern the transition probabilities between the various conduction and valence band states give the maximum circular polarization for this structure (see Figure 2.5). Poldiode was therefore used to study the effects of reflection and refraction on the EL from a GaAs/AlGaAs quantum well spin-LED.

### 2.3.1 Simulation Inputs

The device structure, shown in Figure 2.8, was a 400 µm circular mesa consisting of a 200 µm *p*-type GaAs substrate, 400 Å of *p*-type$Al_{0.2}Ga_{0.8}As$, followed by a 100 Å undoped GaAs quantum well, and a 750 Å thick *n*-type $Al_{0.2}Ga_{0.8}As$ layer. A 100 Å Fe *n*-type contact covered the top semiconductor layer to simulate the effect of this thin-film spin-aligning

| Material | $n$ | $k$ | $1/\alpha \equiv \lambda/4\pi k$ (μm) |
|---|---|---|---|
| GaAs | 3.646 | 0.089 | 0.701 |
| $Al_{0.2}Ga_{0.8}As$ | 3.32 | 0 | $\infty$ |
| Fe | 3.05 | 3.77 | 0.0166 |
| Au | 0.17 | 4.63 | 0.0135 |

Table 2.3: Optical properties of materials used for quantum well simulation.

contact on photon polarization. 100 nm of Au on the bottom of the semiconductor substrate provided the $p$-type contact while another 100 nm of Au was supplied to simulate a 50 μm radius bonding pad to the Fe layer. The optical properties used for each of the layers are given in Table 2.3.

Conduction electrons in the device were assumed to be in one of three states: spin up $|\uparrow\rangle$, spin down $|\downarrow\rangle$, or having a random spin orientation ($a|\uparrow\rangle + b|\downarrow\rangle$ such that $|a|^2 = |b|^2 = 1/2$). For each of these three electron spin states 25 million photons were generated and tracked as they traversed the device.

### 2.3.2 Radiation Pattern and Statistics

The radiation pattern of the simulated quantum well spin-LED is shown in Figure 2.9. The radiation patterns for all three electron spin orientations were identical so only the results for the random spin orientation are shown. A small number of photons were emitted in the range $90° < \theta < 180°$, but they accounted for less than 0.3% of all emitted radiation and were therefore left out of this plot. It is worthwhile to note that the photons emitted in this angular range are not due to emission from the bottom of the device, but from side emission. The short absorption length, $1/\alpha = 0.701$ μm, in the GaAs substrate makes it all but impossible for a photon created in the quantum well to traverse the 500 μm of substrate material.

As expected, the radiation pattern is most intense at $\theta = 0$ and drops off significantly as $\theta$ approaches 90°. This is partially due to the angular dependence of conduction band to heavy-hole transitions given in Equation 2.2, but the effect is primarily due to Snell's law. Near $\theta = 0$, a small change in angle corresponds to a small change in the refracted

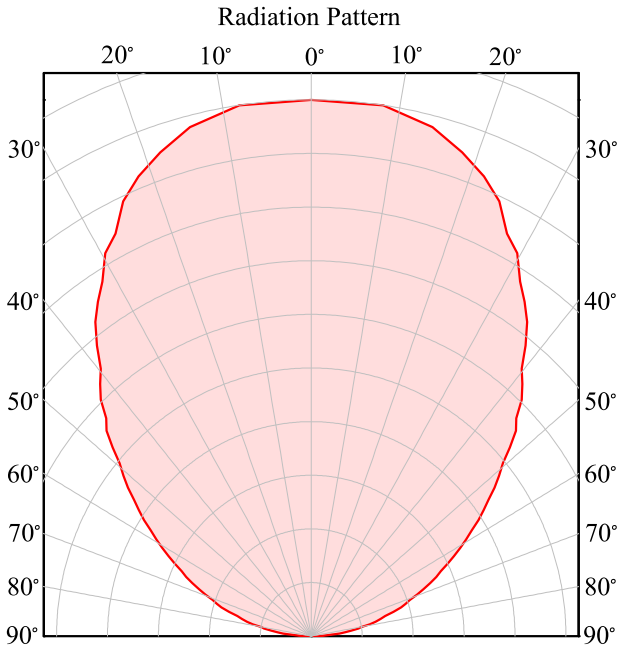


Figure 2.9: Radiation pattern for the quantum well spin-LED simulation. The radiation patterns for all three electron spin orientations were identical.

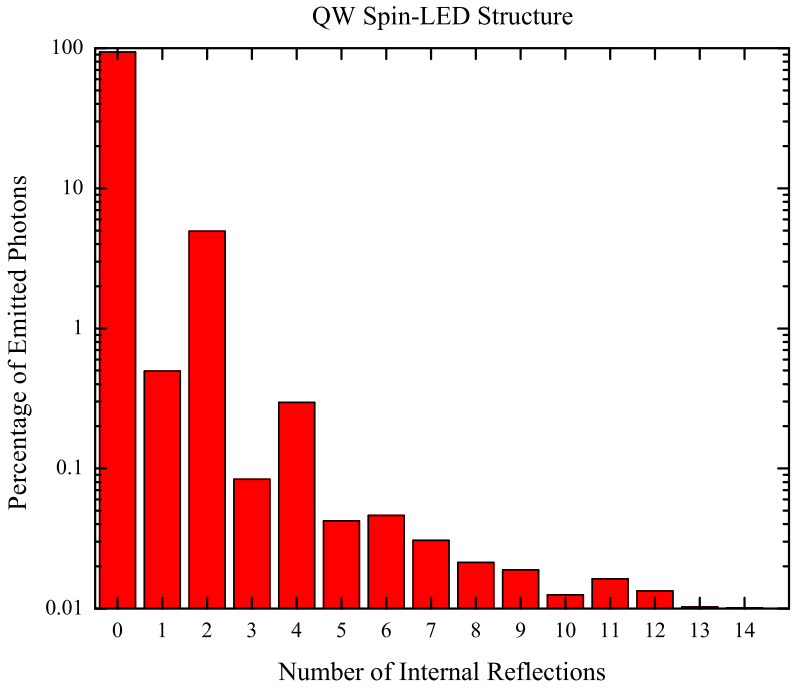


Figure 2.10: Number of internal reflections. 94% of the emitted photons experienced no internal reflections while 5% experienced two internal reflections. The peaks at 2 and 4 occur because of internal reflections within the Fe layer.

angle. However, as the angle of incidence increases towards the critical angle much larger changes are observed.

The number of internal reflections that the emitted photons experienced is shown in Figure 2.10. The vast majority, 94%, of photons experienced no internal reflections. A much smaller fraction, 5%, experienced two internal reflections while 0.5% and 0.3% experienced one and four internal reflections, respectively.

The peaks at two and four reflections in Figure 2.10 stand out immediately upon visual inspection. The reason for these peaks can be understood by considering the case of reflection and refraction at normal incidence. For the quantities defined in Figure 2.6a, the reflection probability at normal incidence is given by

$$\left|\frac{E''}{E}\right|^2 = \left|\frac{\tilde{n}' - \tilde{n}}{\tilde{n}' + \tilde{n}}\right|^2 . \tag{2.34}$$

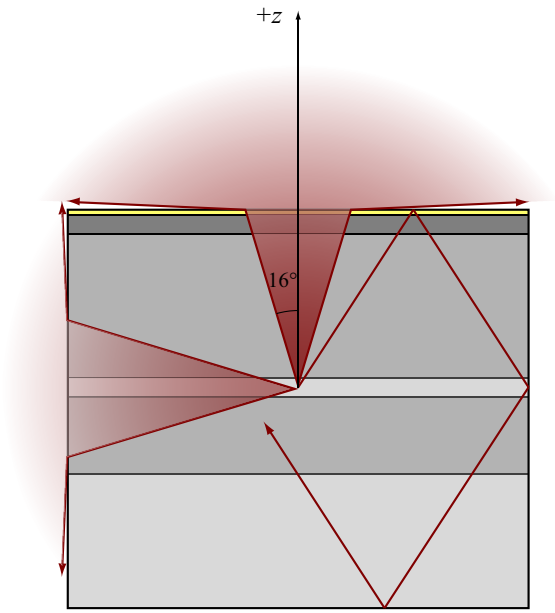


Figure 2.11: Photon trapping within the device. Any photon that is radiated with an emission angle not in the ranges $0° < \theta < 16°$ or $84° < \theta < 106°$ cannot escape.

Imagine a photon that is created with $\mathbf{k} = k_z\hat{z}$ in the active region. The photon will travel up through the $Al_{0.2}Ga_{0.8}As$ layer and through the thin Fe region. Plugging in the values for $\tilde{n} = n + ik$ from Table 2.3, the probability for the photon to undergo a reflection at the Fe/air interface is 60% and the probability for a reflection at the $Al_{0.2}Ga_{0.8}As$/Fe interface is 51%. There is therefore a 18% probability that the photon will, once it is in the Fe layer, undergo two reflections at the boundaries of this region and then escape the device.

It is also interesting to note that the external quantum efficiency of this spin-LED is only 2.45% and that side emission accounts for only 0.6% of all radiation. The small external quantum efficiency is due to two factors: the small critical angle of 16° and the significant probability for reflection within the device. Because of the small critical angle and the geometry of the structure, any photon with $16° < \theta < 84°$ or $106° < \theta < 164°$ will never be able to escape the device (see Figure 2.11)

The small percentage of radiation from side emission is primarily due to height of the GaAs substrate and the proximity of the quantum well to the top surface. Most photons created within the angular range acceptable for side emission will be generated far away from the sides of the mesa. As the photon propagates to the side, a significant portion

of its path will lie inside the strongly absorbing GaAs substrate. Designing a quantum well spin-LED for side emission will therefore require a substrate that will not absorb the radiation from the well. The GaAs/$In_xGa_{1-x}As$ system satisfies this requirement because the radiation from the $In_xGa_{1-x}As$ quantum well lies beneath the absorption edge of the GaAs substrate.

### 2.3.3 Polarization Properties

The radiation pattern and statistics on reflection and refraction within the LED structure provide interesting information and can assist in the design of an optical train to maximize signal, but the polarization properties of the emission determine the coupling of this radiation to the electron spin orientation. The normalized Stokes parameters that describe the polarization state of the light are displayed in Figure 2.12. These results should be compared to Figure 2.5 to show the effects that reflection and refraction have on the light emitted from a spin-LED.

#### 2.3.3.1 Linear Polarization *Q/I*

The $\hat{\phi}$, $\hat{\theta}$ basis was chosen to represent the polarization state of the light. $Q/I$ therefore represents the degree of linear polarization along these axes. From Figure 2.12a, the light is significantly polarized along the $\hat{\phi}$ direction. The maximum for this linear polarization occurs not at 90° as is the case for the initial photon polarization, but at ~105°. The linear polarization drops to zero as $\theta$ approaches 0° and 180°. The azimuthal symmetry of the device forces any linear polarization component along $\hat{\theta}$ to be equal to that along $\hat{\phi}$, making $Q/I = 0$ at those angles.

The maximum at 105° can be understood in terms of the reflection and transmission probabilities for the two components of linear polarization at the GaAs/air interface. First recall that the photons that are emitted in the angular range $90° < \theta < 180°$ are all due to side emission from the mesa. The $\hat{\phi}$ component of polarization will be transmitted with greater probability (see equations 2.26–2.29) than the $\hat{\theta}$ component, giving rise to an enhancement of $Q/I$. This effect convoluted with the initial linear polarization distribution

(a)

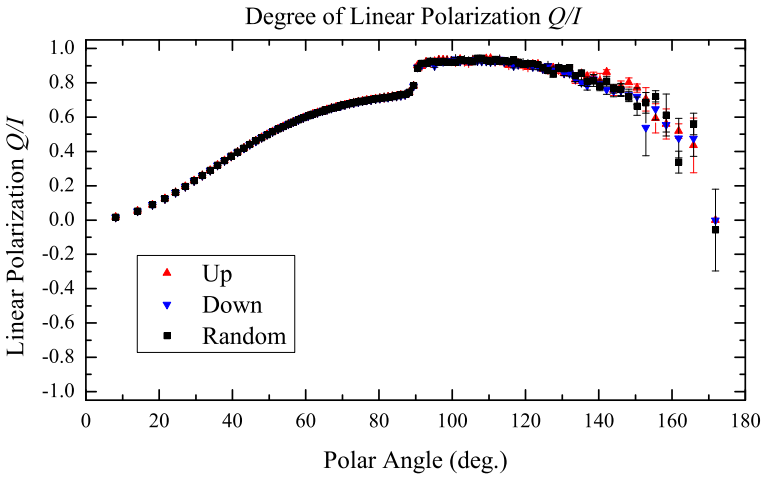


(b)

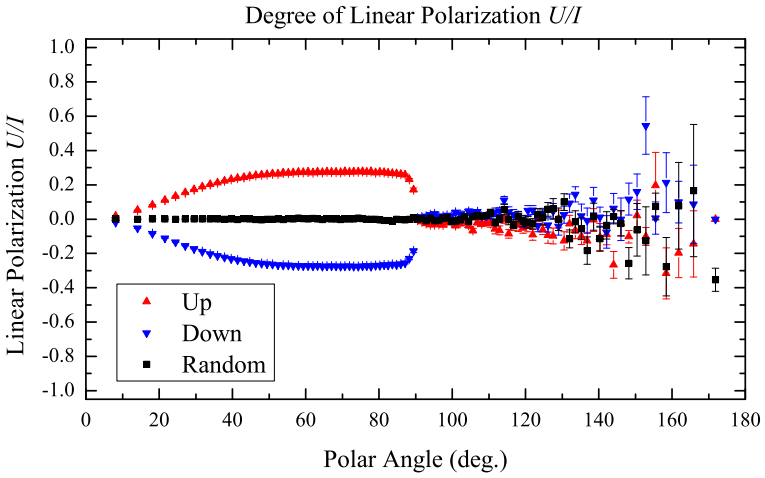


(c)

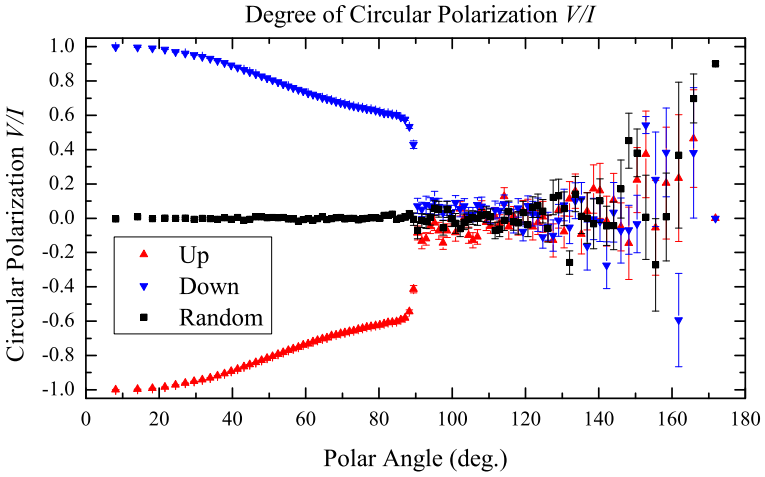


Figure 2.12: Polarization properties of radiation from the QW device simulated by Poldiode. (a) Linear polarization $Q/I$ is independent of electron spin orientation. (b) Linear polarization $U/I$ is spin dependent and assumes a maximum value of 0.28 for $45° < \theta < 85°$. (c) Circular polarization $V/I$ is significantly enhanced over the initially generated distribution shown in Figure 2.5c, especially for $60° < \theta < 90°$.

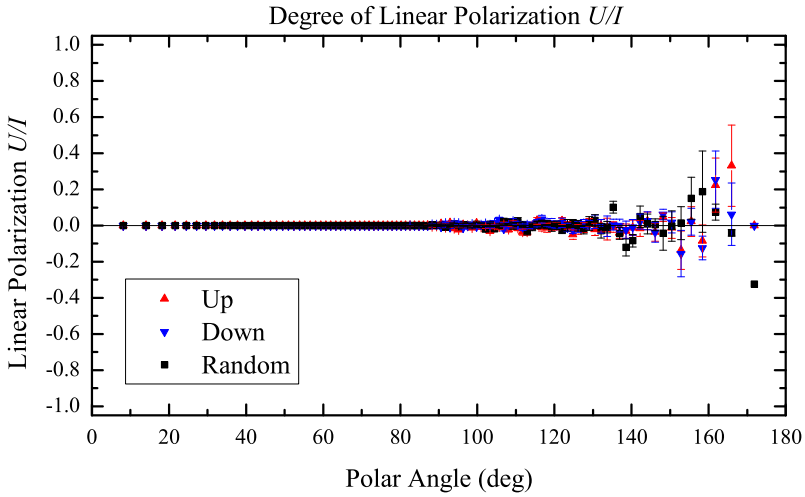


Figure 2.13: $U/I$ for a quantum well spin-LED without a Fe layer. There is no linear polarization along $\left(\hat{\phi}+\hat{\theta}\right)/\sqrt{2}$ and $\left(\hat{\phi}-\hat{\theta}\right)/\sqrt{2}$.

of the photons created in the spin-LED give rise to this maximum.

#### 2.3.3.2 Linear Polarization *U/I*

$U/I$ represents the linear polarization along $\left(\hat{\phi}+\hat{\theta}\right)/\sqrt{2}$ and $\left(\hat{\phi}-\hat{\theta}\right)/\sqrt{2}$. Upon photon creation, the expected ensemble average value for $U/I$ is 0 regardless of polar angle. Refraction in the various semiconductor and metal layers, however, gives rise to non-zero $U/I$ in the range $0° < \theta < 90°$. Moreover, this phenomenon is dependent upon the spin orientation of the conduction electron involved in the recombination process. How does this come about?

Calculation of the amplitudes of the reflected and refracted electric field components rely upon the complex index of refraction, $\tilde{n}$, not simply its real part, $n$. Because $n$ and $k$ are close in magnitude for the Fe layer, refraction at the $Al_{0.2}Ga_{0.8}As$/Fe and Fe/air interfaces introduces a significant phase shift to the circular polarization of the light, resulting in the distribution for $U/I$ shown in Figure 2.12b. The absence of this effect for $90° < \theta < 180°$ adds supporting evidence for this assertion. Figure 2.13 shows $U/I$ for the same quantum well spin-LED device, but without the Fe contact layer. $U/I$ is 0 for this device,

independent of the polar angle. This confirms that the effect seen in the simulation is due to the optical properties of the iron spin-aligning contact.

If the Faraday geometry is to be used for optical measurement of spin injection from Fe, an off-axis measurement of $U/I$ may be made to determine the efficiency of the spin injector. However, this measurement technique is imprecise because it is subject to variations in the optical properties of the spin injector used. Also, the signal strength would suffer because of the decrease in light intensity away from $\theta = 0°$.

#### 2.3.3.3 Circular Polarization *V/I*

The circular polarization of the spin-LED is depicted in Figure 2.12c. As expected, $V/I$ is spin dependent, achieving its maximum value at $\theta = 0$. Comparing this to Figure 2.5c, there is a slight supression of the external value of $V/I$ for $20° < \theta < 65°$, but there is a significant enhancement of this quantity for $65° < \theta < 90°$. As in the case for $U/I$, the reason for this is the Fe contact layer. $V/I$ is zero for $90° < \theta < 180°$. The large error bars for this angular range reflect the variance in photon polarization and small statistics.

For most spin injection measurements, lenses are employed in the optical train to improve collection efficiency. Because these lenses can subtend a significant solid angle, integration of $V/I$ over this solid angle introduces a correction factor to the calculation of the spin injection efficiency. As a function of the angle subtended by the optical train, the correction factor, $C(\theta)$[4], is weighted by the intensity distribution of the radiation and is given by

$$\frac{1}{C(\theta)} = \frac{\int_0^\theta \left(\frac{V}{I}\right) I d\theta'}{\int_0^\theta I d\theta'}. \tag{2.35}$$

For the quantum well spin-LED device simulated in this section, the correction factor is shown in Figure 2.14.

In general, $C(\theta)$ depends upon the exact device structure as well as the optical properties of each device layer. Any new device structure for spin injection must be simulated by Poldiode and a new correction factor calculated.

[4]It has been assumed that the the detector is on-axis with the LED so there no $\phi$-dependence.

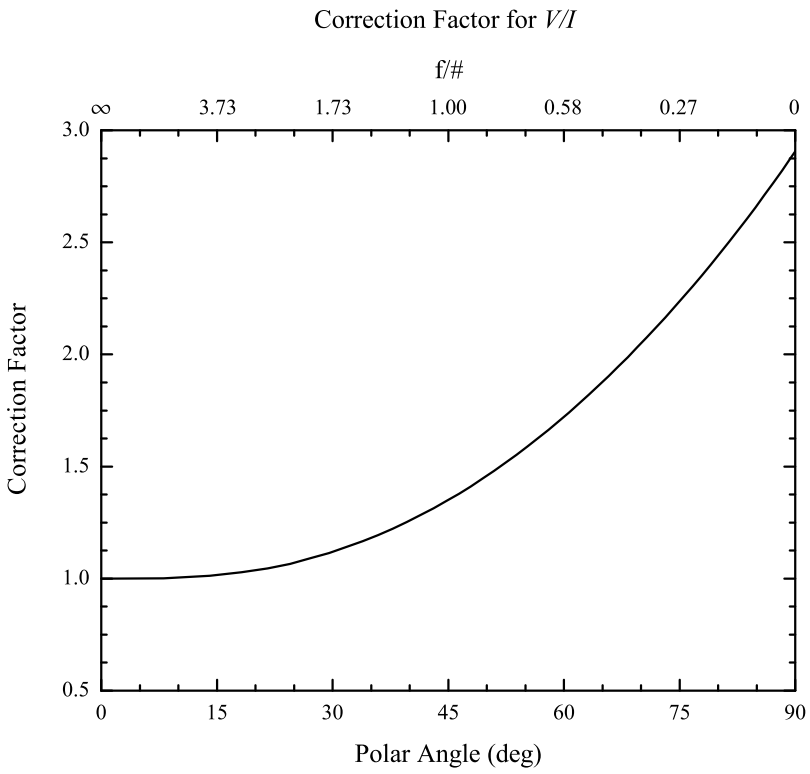


Figure 2.14: Correction factor for $V/I$. The correction factor is given as a weighted average of the degree of circular polarization.

## 2.4 Summary

The spin-LED structure is useful for the measurement of spin injection efficiency. However, the correlation between an injected electron's spin orientation and the polarization of radiation from such a device is structure dependent. Poldiode, a Monte Carlo ray-tracing spin-LED simulator, was developed to address these issues and to determine the feasibility of side emission measurements.

For the typical GaAs/AlGaAs system used in spin injection measurements, side emission measurements are not possible due to the strongly absorbing GaAs substrate present in these devices. This problem could be resolved by substrate thinning, but the desire to measure emission from the sides of these devices would make sample handling difficult at best. A better solution is to use a different material system, such as GaAs/InGaAs, where absorption in the semiconductor substrate is not an issue. Spin injection measurements could then be made without the need for large external magnetic fields to align the contact magnetization along the hard axis of the material.

The polarization state of light emitted from a quantum well spin-LED is affected strongly by refraction, but only slightly by reflection. Only 5% of the photons emitted from this type of device undergo internal reflection, accounting for its small influence on photon polarization. Linear polarization $Q/I$ does not allow for differentiation between initial spin states of conduction electrons, but $U/I$ does. This differentiation, however, is dependent upon the optical properties of the spin-aligning contact. For the device under consideration in §2.3, $U/I$ attains a maximum of 0.28.

Circular polarization is the quantity of greatest interest for spin-LEDs. The circular polarization state can be significantly altered because of the spin-aligning contact material, but still retains a strong correlation to the electron spin state. In order to accurately relate $V/I$ back to the electron's spin, a correction due to the angular dependence of $V/I$ must be made. This correction factor can be calculated using the results of Poldiode.

# References


[1] D. Z. Y. Ting and T. C. McGill, Opt. Eng. **34**, 3545 (1995).

[2] S. J. Lee, Appl. Optics **40**, 1427 (2001).

[3] J. D. Albrecht and D. L. Smith, Phys. Rev. B **68**, 035340 (2003).

[4] G. Schmidt, D. Ferrand, L. W. Molenkamp, A. T. Filip, and B. J. van Wees, Phys. Rev. B **62**, R4790 (2000).

[5] X. Cartoixá, Ph.D. thesis, California Institute of Technology, 2003.

[6] S. Ross, *A First Course in Probability Theory*, 6 ed. (Prentice Hall, Englewood Cliffs, NJ, 2001).

[7] G. F. Koster, J. O. Dimmock, W. R. G., and S. H., *Properties of the Thirty-Two Point Groups*, 1 ed. (M.I.T. Press, Cambridge, MA, 1963).

[8] S. M. Sze, *Physics of Semiconductor Devices*, 2nd ed. (John Wiley & Sons, Inc., New York, YEAR).

[9] J. D. Jackson, *Classical Electrodynamics*, 3rd ed. (John Wiley & Sons, Inc., New York, YEAR).

[10] J. B. Marion and S. T. Thornton, *Classical Dynamics of Particles and Systems*, 4 ed. (Saunders, Philadelphia, PA, 1995).

# Chapter 3 Spin-LED Design and Fabrication

## 3.1 Introduction

It is one thing to create a model to predict the behavior of a physical system. It is quite another to actually construct this system and test the predictions of the model against nature. Having formulated a computer simulation to predict the correlation between the circular polarization of electroluminescence from a spin-LED and the spin orientation of the conduction electrons within the device, a spin-LED was fabricated to (1) verify the experimental results observed by others, (2) extend the list of ferromagnetic metals from which spin injection has been measured, and (3) determine the validity of the model described in Chapter 2. This chapter details the design (§3.2) and fabrication (§3.3) of this device.

## 3.2 Device Design

The design of a spin-LED differs from conventional LED design in several important ways. In a conventional LED the overall intensity and radiation pattern are quantities that should be maximized. Thus, metallic reflecting cups and index-matching epoxies are often components that are employed to maximize light output [1]. A spin-LED, on the other hand, seeks to maximize the polarization of electroluminescence. Intensity takes a backseat to the preservation of carrier spin information. The components that are helpful in normal LED design only serve to confuse the polarization signal through extraneous reflection and refraction. Instead, one must be conscious of the spin lifetime, $\tau_s$, the properties of the metal-semiconductor interface, and the valence bands involved in carrier recombination.

| Reference | Material | $\tau_s$ (ns) | T (K) | $N_D(\text{cm}^{-3})$ |
|---|---|---|---|---|
| Kikkawa [2] | GaAs | 100 | 5 | $1 \times 10^{16}$ |
| Beschoten [3] | GaN | 20 | 5 | $3.5 \times 10^{16}$ |
| Murzyn [4] | InSb | 0.3 | 300 | $2 \times 10^{17}$ |
| Murzyn [4] | InAs | 1.6 | 300 | $3.8 \times 10^{16}$ |

Table 3.1: Spin lifetimes for various semiconductor materials. The long spin lifetime of GaAs at low temperatures makes it ideal for spin injection measurements.

### 3.2.1 Design Considerations

Table 3.1 lists the spin lifetimes for several different III–V semiconductor materials. The long spin lifetime of conduction electrons in GaAs makes this material ideal for spin injection measurements. Although cryogenic temperatures are not well-suited for deployment of commercially available devices, the aim here was not to create a production device, but rather to show proof of the device concept. Spin injection into the AlGaAs/GaAs material system was therefore chosen for this study.

One additional note on lifetimes: spin lifetime is important, but only in its relation to the lifetime of the carrier of that spin. In a *p*-type semiconductor, the electron lifetime for radiative recombination[1] is given by

$$\tau_n = \frac{1}{\beta p}, \tag{3.1}$$

where $\beta$ is the radiative recombination coefficient and $p$ is the hole density in the material. For GaAs at room temperature, $\beta = 7.2 \times 10^{-10}\,\text{s/cm}^3$ [5]. If the acceptor doping is $N_A = 1 \times 10^{18}\,\text{cm}^3$, the minority carrier lifetime would be 1.4 ns. As temperature decreases the radiative recombination coefficient increases and the minority carrier radiative lifetime becomes even shorter. Taking care to appropriately choose $N_A$ in the *p*-type region, then, allows the electron lifetime to be engineered such that $\tau_n \ll \tau_s$. Doing this ensures that the spin information that is transported across the metal-semiconductor interface is preserved until the electron undergoes a recombination event.

[1] Electron lifetime, of course, is affected by other recombination mechanisms (Auger, single- and multiple-level trap-mediated recombination). However, these recombination processes do not contribute to the optical radiation from the LED, which is the quantity of interest.

As discussed in §1.3.3, spin injection from a ferromagnetic metal into a semiconductor relies upon the existence of a tunnel barrier. The Schottky barrier that naturally forms at a metal-semiconductor interface fills this role and has been used by others to achieve significant levels of injection. Doping levels at the metal-semiconductor interface, however, must be chosen carefully—too small a value of $N_D$ will leave the Schottky barrier too wide for a significant tunneling current to flow, while too large a value of $N_D$ will narrow the barrier to the point that the barrier resistivity no longer dominates that of the semiconductor.

It is also important to note that the doping of the *n*-type region must only be high in the vicinity of the contact. Low or moderate doping levels must be used throughout the remainder of this region because spin-LEDs measure the spin polarization of the overall electron population, not just the spin polarization of the injected carriers. Doping level also impacts spin lifetime. It has been found experimentally that a doping level of $N_D = 10^{16}\,\mathrm{cm}^{-3}$ maximizes the spin lifetime in GaAs [2].

In order to improve the measured polarization signal from the spin-LED, it is also advantageous to include a quantum well in the device design. The well serves two functions: (1) it enables spectral resolution of conduction band to light-hole and conduction band to heavy hole transitions, thereby increasing the polarization signal as discussed in §2.2.1.3, and (2) it confines the observed recombination events to a narrow region of the device. The question of whether an event occurred within the quasi-neutral or space charge regions is moot.

Figure 3.1 displays the energy of the ground state energy for a $Al_{0.2}Ga_{0.8}As/GaAs/Al_{0.2}Ga_{0.8}As$ quantum well structure as a function of well width at room temperature, 77 K, and 0 K. As the well width increases, the ground state energy approaches the bandgap of bulk GaAs. For low temperatures, a 100 Å quantum well is sufficient to separate the quantum well energy from that of the bulk by 0.03 eV. The quantum well luminescence peak should therefore be separated from that of the substrate by 16 nm.

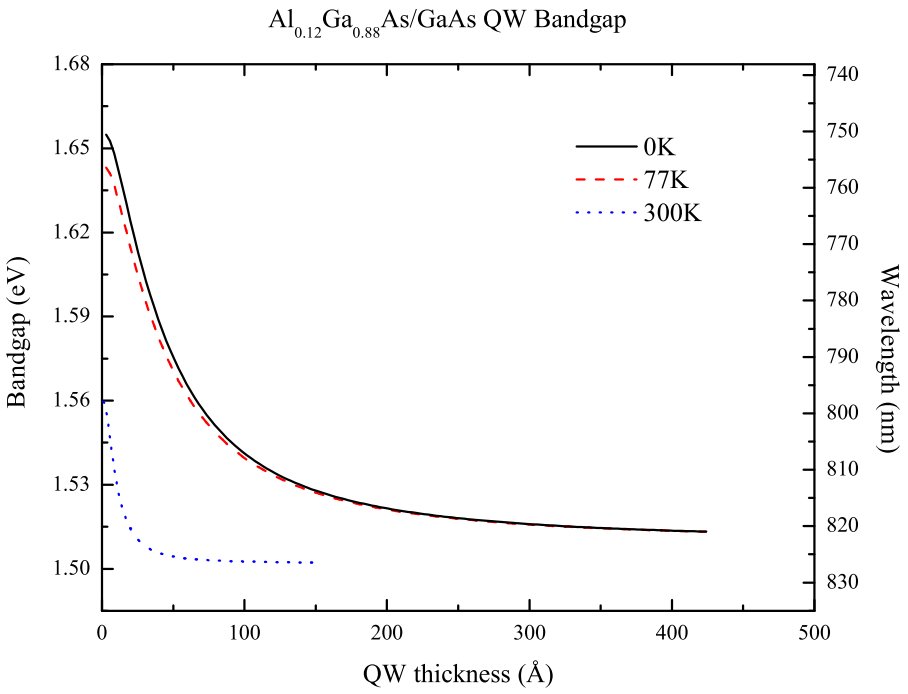


Figure 3.1: Quantum well ground state energy as a function of well width.

### 3.2.2 Simulation via SimWindows

Taking all of these factors into account, a spin-LED structure was designed using SimWindows[2], a 1-D device modeling program. The device consisted of a 200 nm $p$-GaAs buffer layer followed by 400 Å of $p$-$Al_{0.2}Ga_{0.8}As$, both with $N_A = 10^{18}\,cm^3$, a 100 Å undoped GaAs quantum well, and topped off by 750 Å of $n$-$Al_{0.2}Ga_{0.8}As$ ($10^{16}\,cm^3$). The $n$-type layer was segmented into three different doping regions: 500 Å at $10^{16}\,cm^3$, a 150Å $2 \times 10^{18}$–$2 \times 10^{19}\,cm^3$ transition region, and 100 Å at $2 \times 10^{19}\,cm^3$ to decrease the width of the tunnel barrier. A 0.5 V Schottky barrier was also included at the $n$-type contact in the model. The band diagram for this structure can be seen in Figure 3.2.

At 2 V applied bias, the space charge region reaches to the border of the doping transition (see Figure 3.3). Referring to Figure 3.4, the SHR recombination rate accounts for the majority of recombination events. Radiative recombination, however, does occur to significant levels within the quantum well.

### 3.2.3 Spin Aligning Contact Materials

The discussion of the spin-LED device design would not be complete without taking into consideration the material used to align the electron spins. In addition to the properties of the tunnel barrier present between the metal and semiconductor, the spin polarization

$$P = \frac{N_\uparrow(E_F) - N_\downarrow(E_F)}{N_\uparrow(E_F) + N_\downarrow(E_F)}, \tag{3.2}$$

where $N_\sigma(E)$ is the spin-dependent density of states, of the metal must also be accounted for when designing an efficient spin injection system. Notice that $P$ is calculated using the density of states *at the Fermi level* since only these electrons are available for conduction. If the resistivity of the tunnel barrier is spin-independent, the polarization of electrons within the semiconductor can only be as high as this quantity. Table 3.2 summarizes the spin polarization for several different contact materials.

Based on this information and the desire to study spin injection in the absence of an

[2]Simwindows is freely available from `http://www.simwindows.com`. Version 1.5.0 was used for this work.

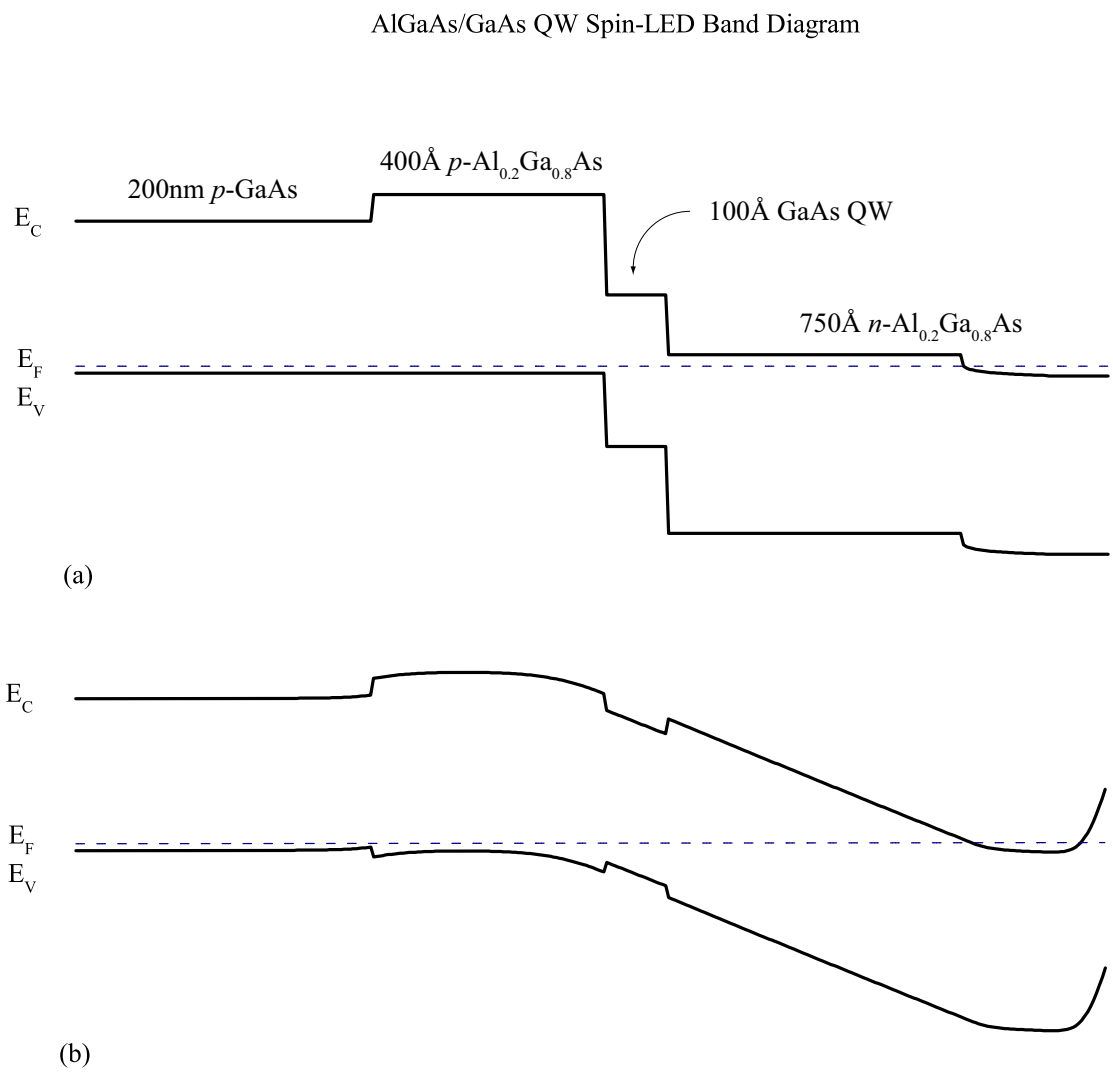


Figure 3.2: Band diagram for the AlGaAs/GaAs QW spin-LED. (a) Flat band diagram and (b) thermal equilibrium at zero applied bias, including a 0.5 V Schottky barrier as calculated by SimWindows. The flat band diagram does not clearly indicate the location of the quantum well due to the abrupt doping changes on both sides of the well.

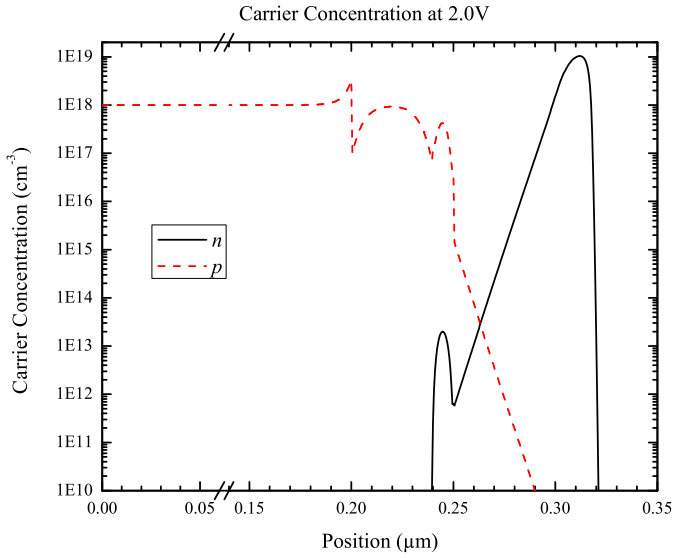


Figure 3.3: Carrier concentrations at 2 V applied bias. The quantum well runs from 0.24–0.25 μm. The space charge region extends to the border of the doping transition in the *n*-type material because of the low doping on this side.

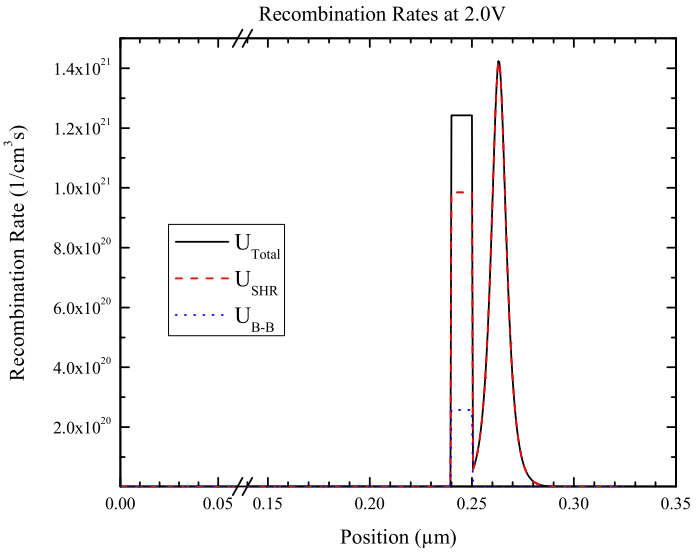


Figure 3.4: Recombination rates at 2 V applied bias. Only the Shockley-Hall-Read (SHR) and band-to-band (radiative) recombination models were included in the device simulation. Radiative recombination predominantly occurs in the quantum well in this model.

| Material | Polarization (%) |
|---|---|
| NiFe | 37 ± 5 |
| Co | 42 ± 2 |
| Fe | 44 ± 2 |
| Ni | 43 ± 2 |
| NiMnSb | 58 ± 2.3 |
| LSMO | 78 ± 4.0 |
| $CrO_2$ | 90 ± 3.6 |

Table 3.2: Contact polarization at $E_F$ for various magnetic films as determined by point contact Andreev reflection. Adapted from [6].

externally applied field, two materials were chosen for this study: Fe and Co-Cr.

#### 3.2.3.1 Iron

The exchange integral

$$K = \iint \psi_1(\mathbf{x}_1)\,\psi_2(\mathbf{x}_2)\,\frac{e^2}{|\mathbf{x}_1 - \mathbf{x}_2|}\psi_1^*(\mathrm{x}_2)\,\psi_2^*(\mathbf{x}_1)\,d^3\mathbf{x}_1 d^3\mathbf{x}_2 \tag{3.3}$$

for a two-electron system with wavefunctions $\psi_n(\mathbf{x}_n)$ causes the parallel spin state for the $d$-band valence electrons of transition metals such as Fe, Co, and Ni to be energetically favorable, giving rise to ferromagnetism. Fe has a magnetization of $\sim 2.41\,\mu_B$/atom compared with 1.72 and $0.61\,\mu_B$/atom for Co and Ni, respectively [7]. As discussed in the previous section, however, it is not the magnetization of the material that matters, but the spin polarization at the Fermi level. On these grounds, these three materials are on equal footing.

Iron, however, does have a distinct advantage when considering the optical properties. For light with an energy $h\nu = 1.53\,\mathrm{eV}$, the absorption index is 3.77 for Fe, 4.45 for Ni, and 4.78 for Co [8]. The absorption lengths for those materials at that wavelength are therefore 16.6, 14.1, and 13.1 nm for Fe, Ni, and Co, respectively. For a given contact thickness, iron will transmit more light than these other materials. For this reason, Fe was chosen as the elemental ferromagnet of choice for spin injection.

#### 3.2.3.2 Cobalt-Chromium

One objection to the validity of spin-LED injection measurements is the need for large external magnetic fields to provide out-of-plane magnetization for the spin-aligning contact This is because the shape anisotropy for these micromagnets causes the easy-axis for magnetization to lie in the plane of the thin metallic film. Crystalline anisotropy is of no help in the specific case of Fe. Iron preferentially magnetizes along the $\langle 100 \rangle$ crystallographic direction, but the large number of equivalent directions ensures that contact magnetization will naturally lie in the plane. A large external field must therefore be applied in order to align the magnetization along the hard axis in order to perform spin injection measurements in the Faraday or Kerr geometries used in these experiments.

The presence of a large magnetic field should only affect elliptically polarized light through the introduction of a phase difference between its right-circularly polarized and left-circularly polarized components via Faraday rotation. However, a cleaner and simpler experiment would be one in which the easy axis for contact magnetization naturally lies out of the plane of contact. In this ideal situation, the contact may be magnetized, the external field turned off, and spin injection may be made with $\mathbf{H} = 0$. Cobalt-chromium alloys can satisfy this requirement if the Cr content is 10–27 at.% [9].

The growth of thin-film Co-Cr results in the formation of Co-rich columns surrounded by Cr-rich material radiating out from these columns in a "chrysanthemum" pattern (see Figure 3.5). The paramagnetic Cr-rich material creates domain boundaries between neighboring Co-rich columns, essentially creating a hexagonal array of Co columnar nanomagnets. In hcp Co, crystalline anisotropy promotes an easy magnetization axis along [0001]. The shape anisotropy of the columns and this crystalline anisotropy both conspire to provide an out-of-plane easy axis.

Following the work of Oldham [10] on electron beam evaporation as a deposition technique for this material, thin-film Co-Cr was also studied as a possible spin injector.

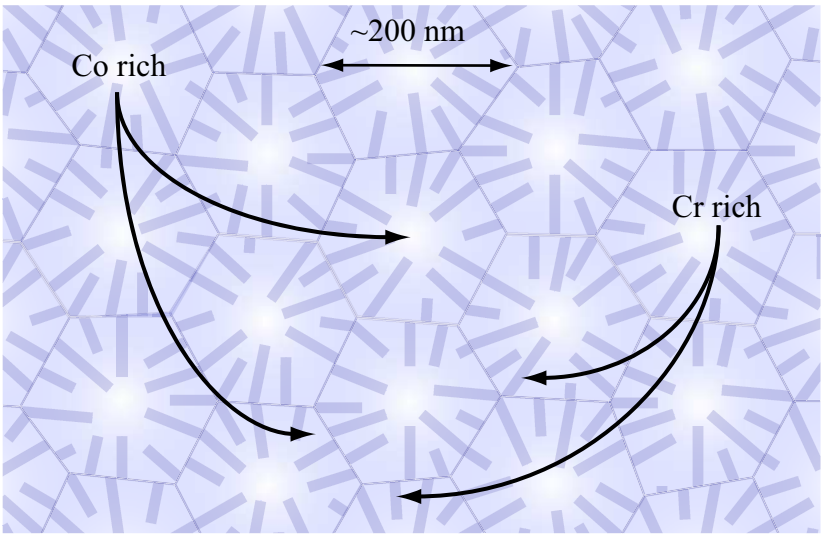


Figure 3.5: Top-down view of the Co-Cr microstructure with out-of-plane easy magnetization axis. Co-rich columns are separated by lines of paramagnetic Cr-rich material. Shape anisotropy of the columns and crystalline anisotropy of hcp Co both work together to provide an out-of-plane easy magnetization axis.

## 3.3 Fabrication

### 3.3.1 Device Growth

The quantum well spin-LED structure discussed in §3.2.2 and shown in Figure 3.2 was grown via molecular beam epitaxy (MBE) at the Jet Propulsion Laboratories (JPL) in a Veeco Applied EPI Gen III system configured for III–V material growth.[3] Diagnostic tools available on this system include RHEED intensity analysis, equivalent beam pressure, and optical flux monitoring for growth rate calibration, as well as RGA for group V species state (monomer, dimer, or tetramer) determination and mass spectroscopy for further analysis of the growth process.

The structure, Sb0643,[4] was grown at a target growth rate of 2.5 Å/s on a 2 in (100) $5\times10^{18}$–$5\times10^{19}$ $cm^{-3}$ Zn doped $p$-GaAs substrate heated to 584±2 °C. Dopants used in this device growth were Si and Be for $n$- and $p$-type material. In order to create the transition from the 400Å low-doped ($10^{16}$ $cm^{-3}$) $n$-type region to the highly doped ($2 \times 10^{19}$ $cm^{-3}$)

[3]Device growth performed by Cory Hill.

[4]The "Sb" in the label simply denotes that this growth was performed in a III–V growth chamber typically used for antimonide growth. No antimony was intentionally included in the structure.

Schottky barrier narrowing region, the Si cell temperature was raised during device growth from 1030 °C to 1280 °C. However, because it was desirable to limit the width of the transition and highly doped regions.[5] the growth was stopped after the completion of the low-doped section in order to raise the Si cell temperature to 1230 °C.[6] During this 3 min. and 20 sec. pause in the semiconductor growth, the substrate was maintained in an As flux to stabilize the surface. The next 150 Å of material was then grown while increasing the Si cell temperature at a rate of 50 °C/s.

After the final 100 Å of highly doped *n*-type $Al_{0.2}Ga_{0.8}As$ was grown, the substrate was cooled to room temperature and a ~20 Å As cap was deposited. Because no *in situ* spin-aligning contact deposition method was available, this As cap served to protect the semiconductor surface after removal from the ultra-high vacuum (UHV) growth environment and during wafer transit. The capping layer was removed prior to contact deposition at Caltech.

Figures 3.6 and 3.7 show AFM micrographs of this As capping layer. The surface was found to have a rms roughness of 1.22 nm. In addition, As particles formed on the wafer surface. These particles were pyramidal in shape, had an average height of 1.235 μm and an average area of 6.836 $\mu m^2$. The average particle density was ~780 $mm^2$ and the roughness caused by these particles was observable upon close examination by the naked eye.

Upon arrival at Caltech, Sb0643 was cleaved into quarters to allow for the deposition of different contact materials upon the same device structure. Each quarter was degreased and reintroduced into UHV for As cap removal and contact deposition. The capping layer was removed by heating the substrate to 400 °C for 1 hour. Chamber pressure was also monitored during this process to ensure complete layer removal. Figure 3.8 shows an AFM micrograph of the surface of Sb0643 after cap removal. The scan lines visible in this image are an instrument artifact and only show up in scans of smooth surfaces. By performing a section analysis along one of these scan lines,[7] the rms surface roughness was found to be 0.134nm. In addition, no large particles were found on the semiconductor surface, leading

[5]Recall that the Schottky barrier should be narrow enough to allow a significant tunneling current, but wide enough to dominate the resistivity of the semiconductor (see §1.3.3).

[6]The maximum ramp rate of the Si cell was 50 °C/s.

[7]Performing the analysis along a the artifact removes the effect of the instrument error ~ cos ($\theta$) by always sampling the data at the same phase $\theta + 2n\pi$.

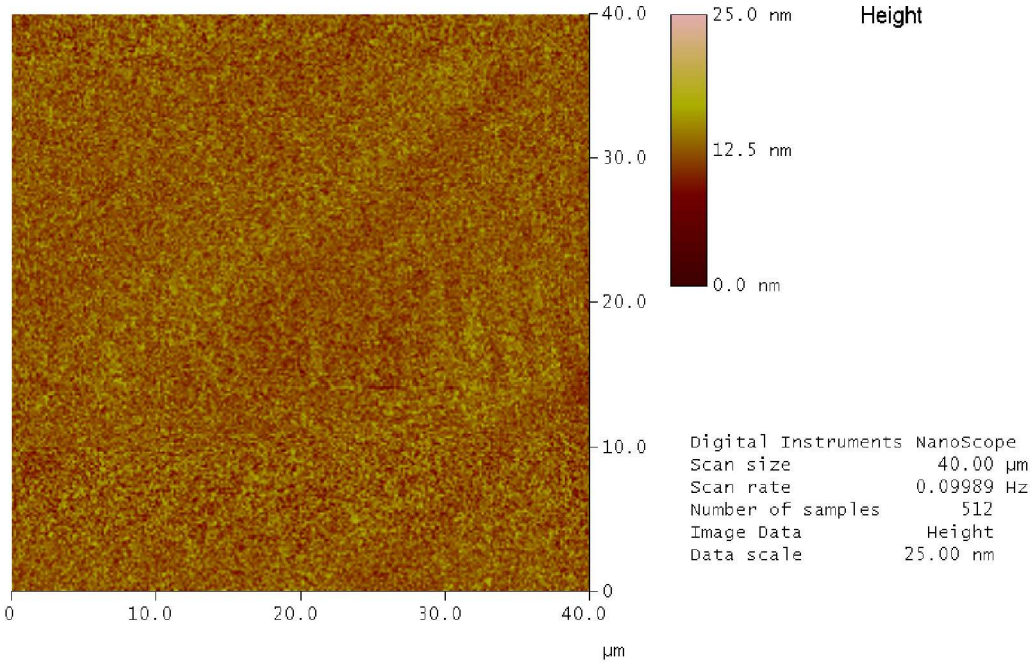


Figure 3.6: AFM micrograph of Sb0643 as grown. This micrograph is representative of the capping layer in an area absent of As particles. The rms surface roughness is 1.216 nm.

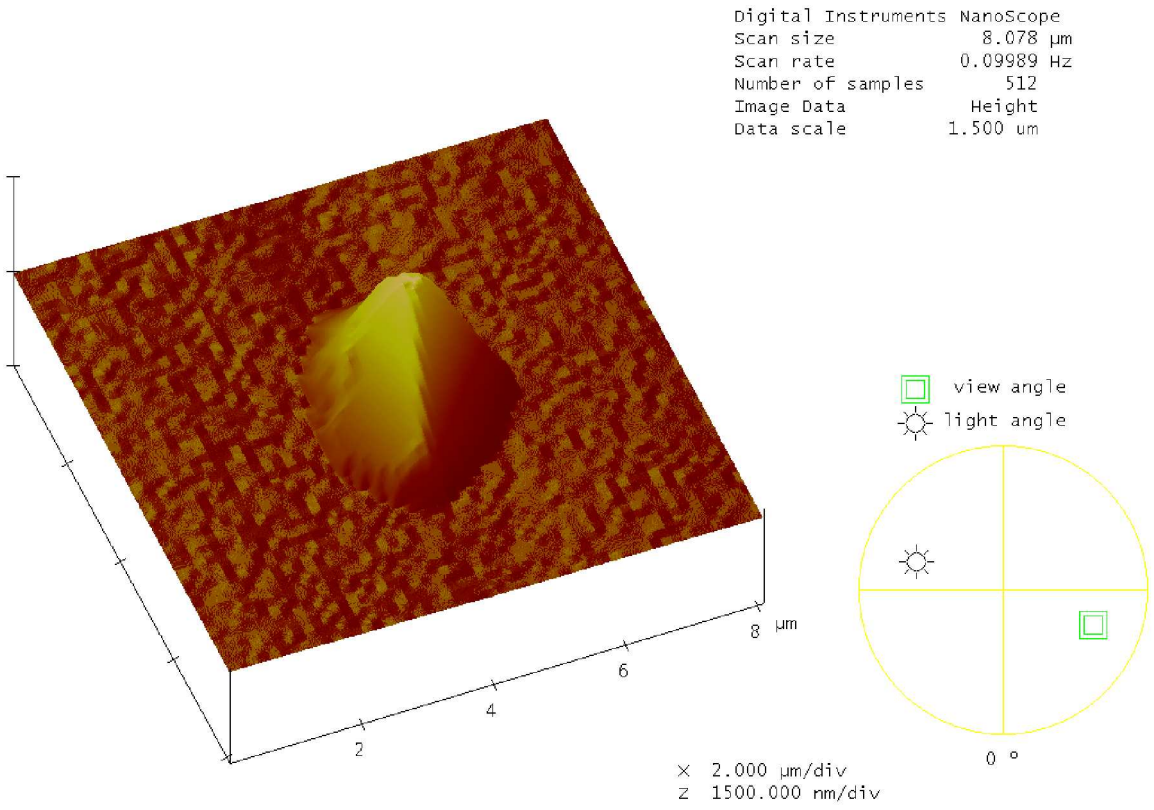


Figure 3.7: Arsenic particle formed during growth. These were unintentionally created during growth of the As capping layer and subsequently removed by heating before metalization. The particle density was ~780 $mm^{-2}$.

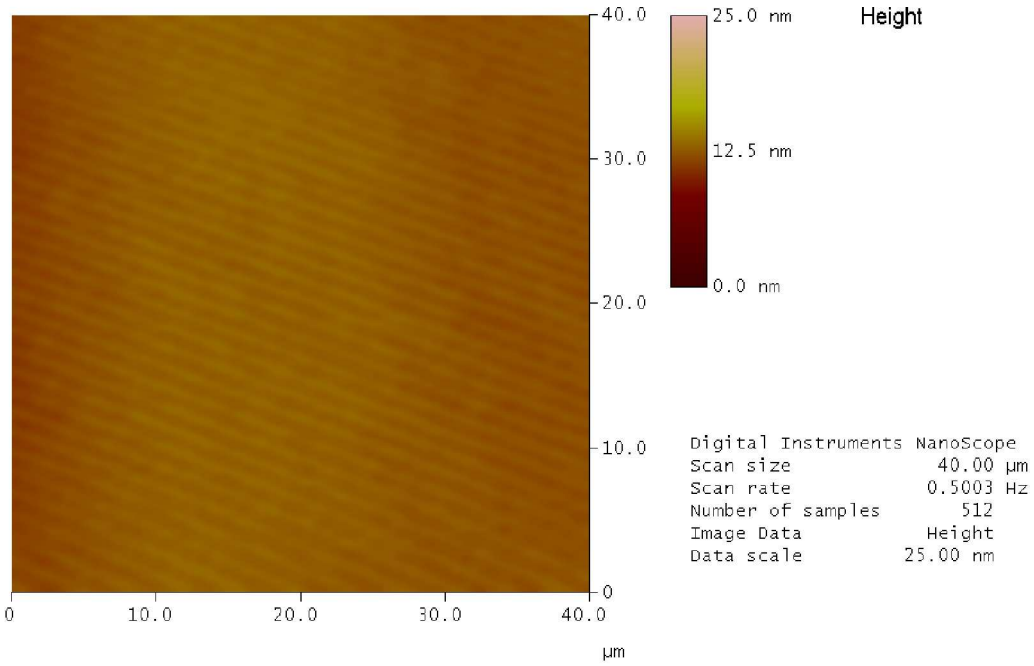


Figure 3.8: AFM micrograph of Sb0643 after As cap removal. The scan lines present are instrument artifacts. Accounting for these artifacts, the rms surface roughness was found to be 0.134 nm.

to the conclusion that this procedure very effectively removes the capping layer.

### 3.3.2 Spin Aligning Contact Deposition

Iron and Co-Cr spin-aligning contacts were both deposited on Sb0643 via electron beam evaporation (EBE). The UHV metalization chamber utilized a Thermionics Model 100-0040 electron gun with four 2.2 $cm^3$ crucibles to hold source material. The electron beam was supplied by thermionic emission from a tungsten filament and guided to heat the source material by a magnetic field from a permanent magnet stationed in the electron gun assembly as well as the potential difference between the filament and crucible provided by a 6 kV Thermionics SEB-06 power supply. Control of the beam spot location on the source

material was achieved by variation of this potential difference. The system also provided substrate heating to allow for deposition temperature control.

Oldham [10] demonstrated deposition of Co-Cr with 16.7 at.% Cr from a single $Co_{0.94}Cr_{0.06}$ EBE target. The reason for the difference between the source and deposited layer composition arises from the difference in vapor pressures for Co and Cr. He found that in general, the atomic fraction of Cr in the deposited material was 2–3 times higher than that in the source. Following this work, a 2.2 $cm^3$ Co-Cr target with an alloy composition consisting of 94 at.% Co and 6 at.% Cr was used.

During EBE of both spin-aligning contact materials, a transition regime of violent bubbling and spitting of source material was observed. If kept in this regime, the source material would shake so violently that it would jump out of the graphite crucible liner. Although both Fe and Co-Cr sources were at least 99.9% pure, it is possible that the heating of impurities in these materials could cause this behavior. It was found, however, that the bubbling and spitting stopped once the cathode filament current was raised above a certain value. The operating procedure for contact deposition, then, was to slowly increase ($\sim 0.1$ mA every 30 sec.) the filament current with electron beam centered on the target material until the onset of spitting. Once this regime was encountered, the filament current was rapidly increased to $\sim 1.5$ mA. Once the system settled in a stable state, the filament current was again increased until the desired deposition rate achieved as measured by a quartz crystal deposition monitor.

Using this procedure, 100 Å thick Fe and Co-Cr layers were each deposited on Sb043 at room temperature. Both samples were capped with an additional 25 Å of Au using the same deposition system in order to prevent oxidation of the spin-aligning contact. Henceforth, the samples will be referred to as Sb0643-Fe and Sb0643-CoCr. A third sample was prepared without EBE contact deposition as a control. This sample will simply be referred to as Sb0643.

### 3.3.3 Processing

Following semiconductor growth and spin-aligning contact deposition, each sample was processed into devices using standard photolithography techniques.

Mesas were formed by a chemically assisted ion beam etch (CAIBE), whereby $Xe^+$ ions sputtered material weakened through chemical reaction with a small influx of $Cl_2$ gas. This process produces good mesa geometry, but can lead to higher surface recombination velocities than achieved with wet etching techniques [11]. Wet etching, however, would require different processes for the removal of the Fe and Co-Cr layers. CAIBE was chosen because it works for all materials and the process recipe could be applied to all three samples under consideration. 100, 150, and 200 μm radius mesas were formed on each sample, and the mesa heights were 550 nm for both Sb0643-Fe and Sb0643-CoCr, and 740 nm for Sb0643. The reason for the difference in mesa heights was due to the slow etch rate for the metal layers in the first two samples.

After mesa formation, the samples were uniformly coated with 200 nm of $SiO_2$ grown by plasma enhanced chemical vapor deposition (PECVD).[8] The deposition was done at a rate of 40 Å/s at a temperature of 250° C. The insulator created a location for the placement of the *n*-type contact bonding pad as well as passivated the surface of the device side walls [12].

The $SiO_2$ was removed from the top of each mesa and from the *p*-type contact region surrounding the devices using 20:1 buffered oxide etch. 100 nm thick TiAu contacts were subsequently deposited via DC magnetron sputtering. The *n*-type contact on the top of each mesa was patterened into a series of 5 μm thick concentric rings connected by a central line in order to ensure that current was supplied uniformly to the device while leaving enough exposed area for efficient light emission. Current spreading in the spin-aligning contacts created even better uniformity for Sb0643-Fe and Sb0643-CoCr. Figure 3.9 shows a schematic of the final device structure and Figure 3.10 shows the processed devices.

The samples were then cleaved into 3.5 mm×2.5 mm pieces, each containing six devices (see Figure 3.10a), and wire-bonded to a ceramic T05 header. The headers, manufactured

[8] $SiO_2$ deposition was performed by Sam Keo at JPL.

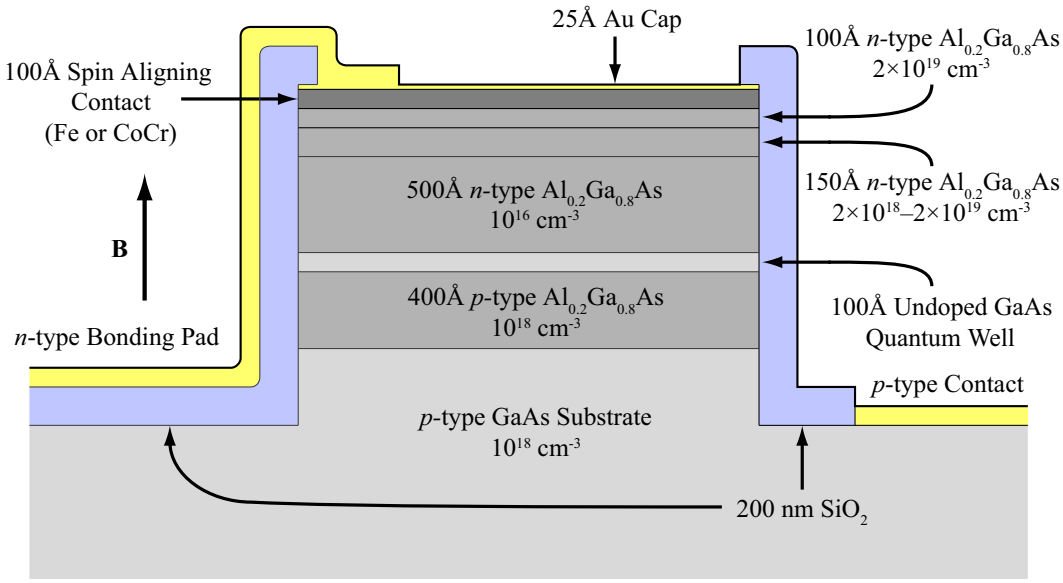


Figure 3.9: Spin-LED device structure.

by Coors Ceramics Company, were non-magnetic so that the injection measurements would not be skewed by header magnetization.

At this stage, the samples were ready for electrical and optical characterization as well as spin injection measurement.

## 3.4 Summary

The design of a spin-LED device has been considered. Many different factors can impact the ability of this device to measure spin injection efficiency. The important design parameters are the following (see §3.2.1):

- semiconductor material choice
- donor doping level, $N_D$
- acceptor doping level, $N_A$
- quantum well width and depth
- spin-aligning contact material choice

(a)

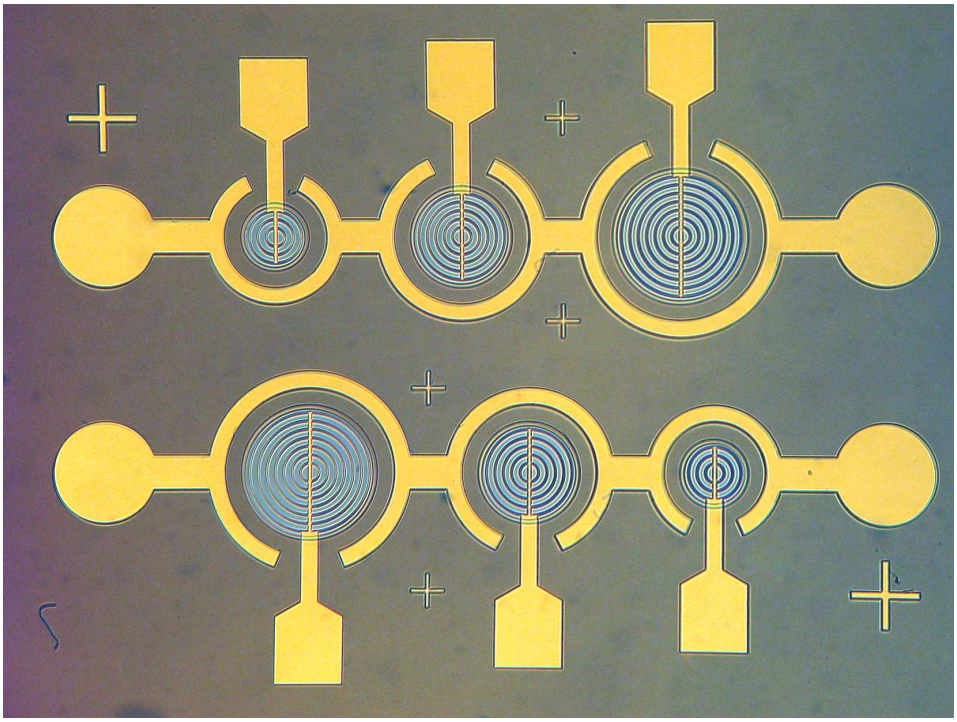

(b)

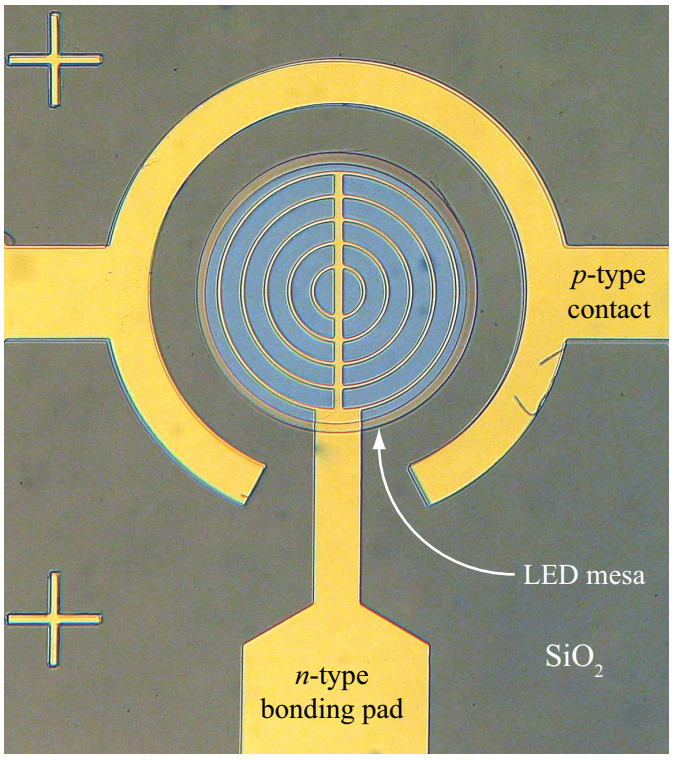


Figure 3.10: Photographs of the finished spin-LED. (a) Six devices representative of one complete unit cell of the photolithography mask. Mesa radii are 200 μm, 150 μm, and 100 μm. (b) Close-up picture of a 150 μm radius device. The photographs are from Sb0643-CoCr, but are identical for the other two samples.

Factoring in these design considerations, a spin-LED structure was grown via MBE. Fe and Co-Cr, a perpendicular magnet for the alloy concentration range 10–27 at.% Cr, were deposited through EBE as spin-aligning contacts. A control sample was also produced without any magnetic contact. These samples were subsequently patterened into LED structures through standard photolithography techniques and wire-bonded to nonmagnetic T05 headers for characterization and spin injection measurement.

# References


[1] S. M. Sze, *Physics of Semiconductor Devices*, 2nd ed. (John Wiley & Sons, Inc., New York, YEAR).

[2] J. M. Kikkawa and D. D. Awschalom, Phys. Rev. Lett. **80**, 4313 (1998).

[3] B. Beschoten, E. Johnston-Halperin, D. K. Young, M. Poggio, J. E. Grimaldi, S. Keller, S. P. DenBaars, U. K. Mishra, E. L. Hu, and D. D. Awschalom, Phys. Rev. B **63**, art. no. (2001).

[4] P. Murzyn, C. R. Pidgeon, P. J. Phillips, J. P. Wells, N. T. Gordon, T. Ashley, J. H. Jefferson, T. M. Burke, J. Giess, M. Merrick, B. N. Murdin, and C. D. Maxey, Physica E **20**, 220 (2004).

[5] Y. P. Varshni, Physica Status Solidi **19**, 459 (1967).

[6] R. J. Soulen, J. M. Byers, M. S. Osofsky, B. Nadgorny, T. Ambrose, S. F. Cheng, P. R. Broussard, C. T. Tanaka, J. Nowak, J. S. Moodera, A. Barry, and J. M. D. Coey, Science **282**, 85 (1998).

[7] C. Kittel, *Introduction to Solid State Physics*, 7th ed. (John Wiley & Sons, Inc., New York, 1996).

[8] *Handbook of Chemistry and Physics*, edited by D. R. Lide (CRC Press, Boca Raton, 2003).

[9] Y. Maeda, M. Asahi, and M. Seki, Jpn. J. Appl. Phys. Part 2 - Lett. **25**, L668 (1986).

[10] N. C. Oldham, Ph.D. thesis, California Institute of Technology, 2004.

[11] S. A. Campbell, *The Science and Engineering of Microelectronic Fabrication*, 2nd ed. (Oxford University Press, New York, 2001).

[12] C. J. Huang, J. R. Chen, and S. P. Huang, Mater. Chem. Phys. **70**, 78 (2001).

# Chapter 4 Spin-LED Characterization

## 4.1 Introduction

Proper characterization of the spin-LED devices was necessary to ensure that the fabrication discussed in §3.3 matched the device design as detailed in §3.2. This chapter describes the analysis of Sb0643, Sb0643-Fe, and Sb0643-CoCr through several different means. The quality and crystal structure of the semiconductor and spin-aligning contacts are first considered and their interfacial properties examined (§4.2). A discussion of the magnetic properties of Sb0643-CoCr follows (§4.3), where the usefulness of this material as a perpendicular magnet is explored. Next (§4.4), the three different samples are characterized electrically. Finally, the luminescence (photoluminescence and electroluminescence) properties of these LED structures are analyzed (§4.5).

## 4.2 Material Characterization

### 4.2.1 Transmission Electron Microscopy

In order to test the quality of the semiconductor and spin-aligning contact growths, unprocessed samples of Sb0643-Fe and Sb0643-CoCr were subjected to analysis by transmission electron microscopy (TEM).[1] The instrument used for this analysis was a Phillips EM430. This instrument offers better than 2.3 Å point-to-point resolution from an accelerating voltage of 300 kV and is well-suited for high resolution TEM (HRTEM) imaging, a technique useful for studying, among other things, defects and atomic arrangement at interfaces.

A note about high resolution transmission electron microscopy: this imaging method is a phase-contrast technique whereby an image is produced through diffraction of the elec-

[1] TEM imaging was performed by Carol Garland.

tron wavefront through a thin sample.[2] Because of this, the aquired images are sensitive to variations in sample thickness and instrument optics in non-intuitive ways. Detailed analysis of the images gathered through this technique rely upon precise knowledge of the microscope operating conditions. Care must be taken in the interpretation of HRTEM images.

In order to speed analysis, the unprocessed samples of Sb0643-Fe and Sb0643-CoCr were epoxied together at their top Au contact layers. The resulting specimen was then polished, dimpled, and thinned by ion milling for HRTEM imaging.

Figure 4.1 shows the entire semiconductor growth as well as the Fe and Au layers for Sb0643-Fe (see the device design in §3.2 for comparision). Lines have been added at the heterojunction interfaces as a guide to the eye due to the low contrast difference between neighboring layers. The dashed line in the middle of the $n$-$Al_{0.2}Ga_{0.8}As$ layer indicates the location of the change in doping from $10^{16}\,cm^{-3}$ to $2\times10^{18}\,cm^{-3}$. The $p$-$Al_{0.2}Ga_{0.8}As$ layer and undoped GaAs quantum well were confirmed to be 401 Å and 98 Å thick, respectively.

The $n$-$Al_{0.2}Ga_{0.8}As$ layer was 725 Å thick, 25 Å off its target thickness of 750 Å. Because the $p$-$Al_{0.2}Ga_{0.8}As$ and quantum well regions matched their design thicknesses almost exactly, it is likely that the low-doped $n$-$Al_{0.2}Ga_{0.8}As$ layer was also correctly grown. After this layer was grown, however, the growth was paused for 3 min. and 20 sec. while the Si cell temperature was raised. One possible cause for the discrepancy in thicknesses, then, is that the growth rate changed slighly while the doping level was increased.

Higher magnification HRTEM images of the Fe/$Al_{0.2}Ga_{0..8}As$ and Co-Cr/$Al_{0.2}Ga_{0..8}As$ interfaces are displayed in figures 4.2 and 4.3. Based on analysis of these images, the thickness of the Fe and Au were found to be 86 Å and 46 Å for Sb0643-Fe while the CoCr and Au thicknesses for Sb0643-CoCr were 87 Å and 32 Å.

The metal-semiconductor interface in both figures shows epitaxial growth of the spin-aligning contacts. The transition from Fe to $Al_{0.2}Ga_{0.8}As$ in Figure 4.2 is abrupt—a clear distiction is apparent between the As-terminated surface of the semiconductor layer and the beginning of the iron growth. The transition region for the Co-Cr/$Al_{0.2}Ga_{0.8}As$ interface is not as distinct, but is only 1–2 monolayers wide and the growth is still epitaxial. Smooth

[2] See references [1] and [2] for more information about phase-contrast imaging.

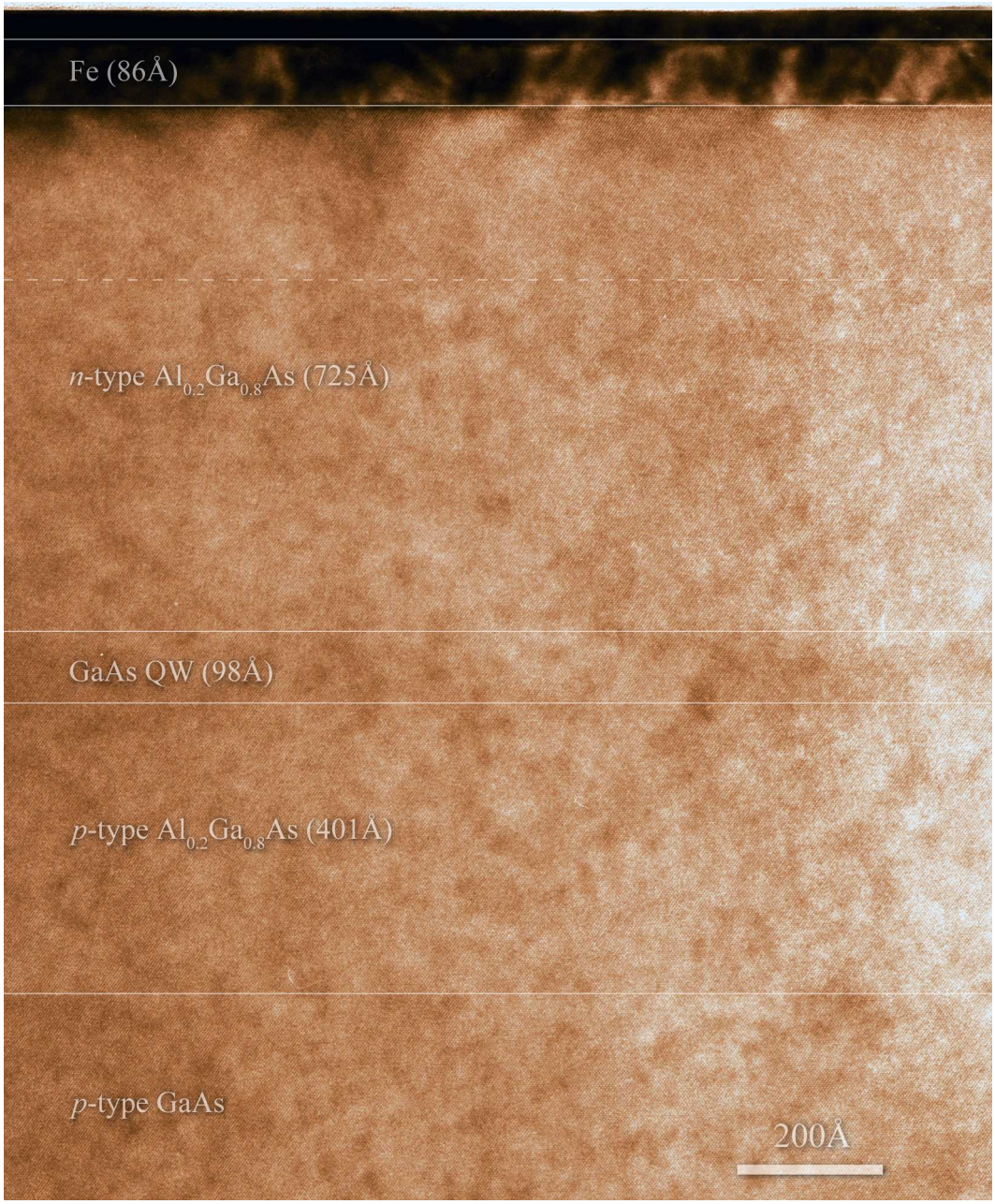


Figure 4.1: TEM micrograph of Sb0643-Fe showing each growth layer. Lines at the semiconductor heterojunctions have been added to aid the eye in distinguishing the layers due to low contrast differences between neighboring layers.

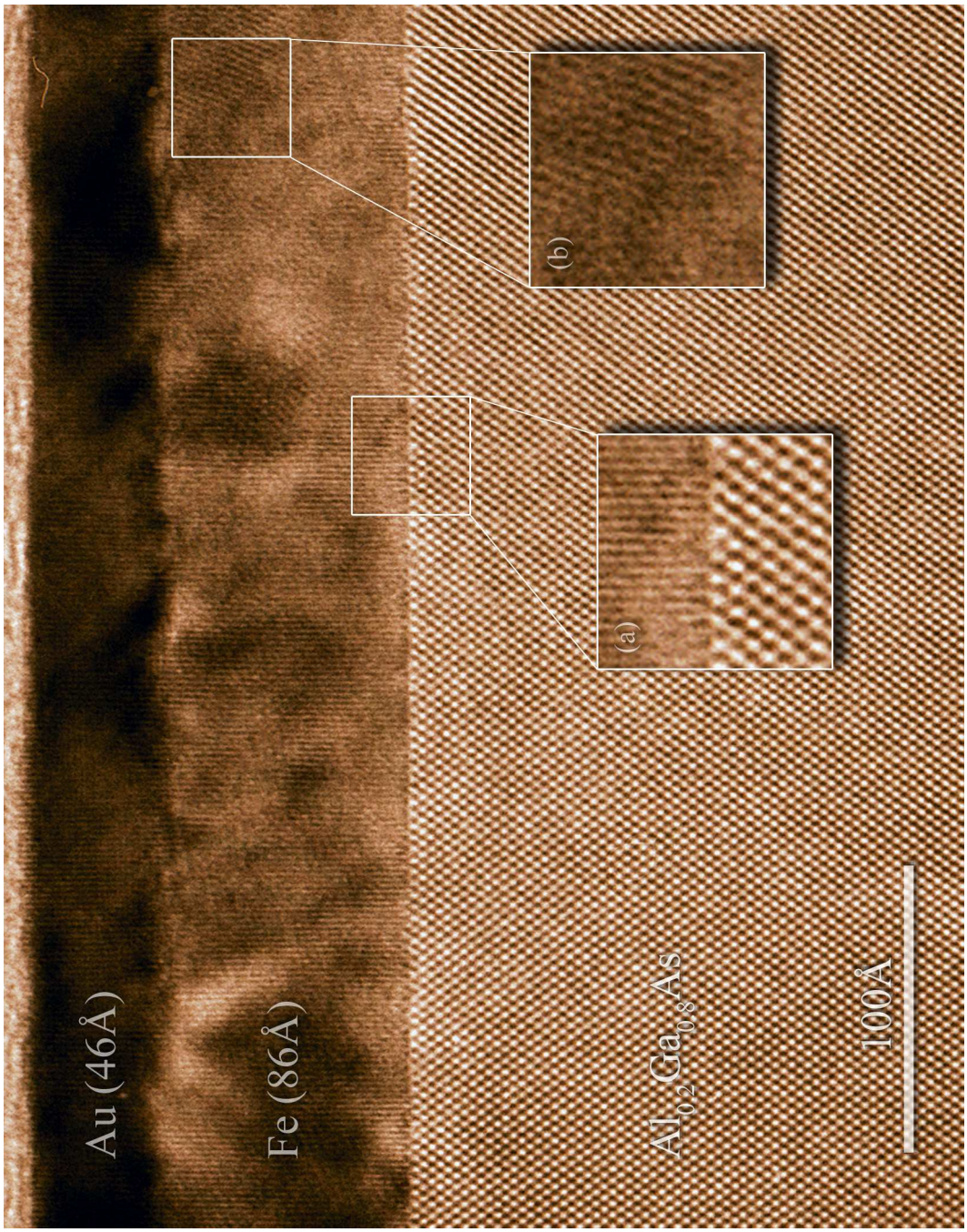


Figure 4.2: HRTEM micrograph of the Fe/$Al_{0.2}Ga_{0.8}As$ interface. Epitaxial growth of Fe on the semiconductor is evidenced by (a). Region (b), however, shows that the growth is not entirely epitaxial, but that the Fe film is polycrystalline. Both this and the roughness of the Fe/Au interface are due to the room temperature deposition of these materials.

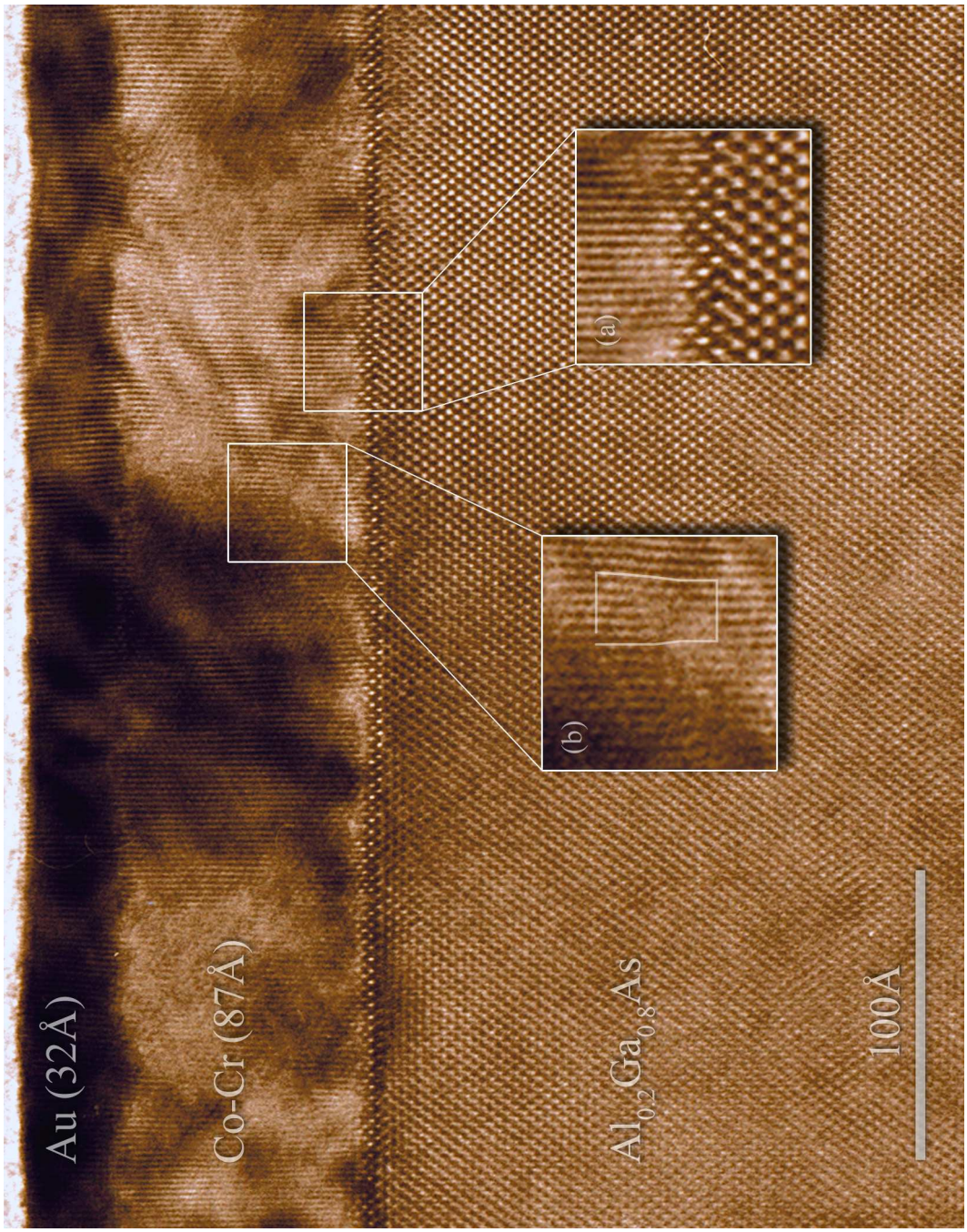


Figure 4.3: HRTEM micrograph of the Co-Cr/$Al_{0.2}Ga_{0.8}As$ interface. As in the case with Sb0643-Fe, (a) indicates epitaxial growth. A Burgers circuit in (b) shows the presence of an edge dislocation.

| Material | Structure | Lattice Constant (Å) | Lattice Mismatch (%) |
|---|---|---|---|
| GaAs | zincblende | 5.65 | - |
| Co | hcp | $a = 2.51$, $c = 4.07$ | - |
| Co [3] | bcc | 2.83 | 0.2 ($2 \times a$) |
| Cr | bcc | 2.88 | 1.95 ($2 \times a$) |
| Fe | bcc | 2.87 | 1.59 ($2 \times a$) |
| Au | fcc | 4.08 | -44.2 (Co), -42.2 (Fe) |

Table 4.1: Lattice mismatch for contact materials in Sb0643-Fe and Sb0643-CoCr [4]. The mismatches listed for Cr and Fe are for twice the lattice constant, $a$, of those materials.

boundaries at both of these interfaces show that the As cap that was deposited to preserve the interfaces (see §3.3.1) served its purpose. The smoothness of these interfaces also corroborates the AFM data proving that the As layer was completely removed prior to contact deposition. The roughness of the Fe/Au and Co-Cr/Au interfaces, on the other hand, was due to the low surface mobility of adatoms at room temperature deposition of these materials.

Examination of these TEM images show that there is a 2 to 1 correspondence between columns of atoms in the metal and the semiconductor. The reason for this correspondence can be understood by looking at the lattice constants for these materials (see Table 4.1). Iron has a lattice constant of 2.87 Å, which is almost exactly half the lattice constant of GaAs, 5.65 Å. The 1.59% lattice mismatch between these two materials is still enough, however, to cause some relaxation within the Fe layer. Several edge dislocations can be seen in Figure 4.2. Also, the Fe growth starts epitaxially, but polycrystalline material forms due to the lattice mismatch and growth temperature.

Cobalt, the predominant element in the Co-Cr thin film, naturally occurs in a hcp phase. For thin films of Co epitaxially grown on GaAs, however, Co will will grow in a body-centered cubic (bcc) structure with a lattice constant of 2.83 Å and lattice mismatch of 0.2% [3]. After about 5 nm of growth, Co will relax into its hexagonal close-packed (hcp) structure [5]. However, the Co-Cr film in Sb0643-CoCr is only 87 Å thick, which is clearly insufficient for this relaxation to occur. Because of the bcc structure of the Co-Cr, the deposited film, unfortunately, does not have the microstructure needed for perpedicular magnetism (see §3.2.3.2). This is one case in which epitaxial growth is actually not advan-

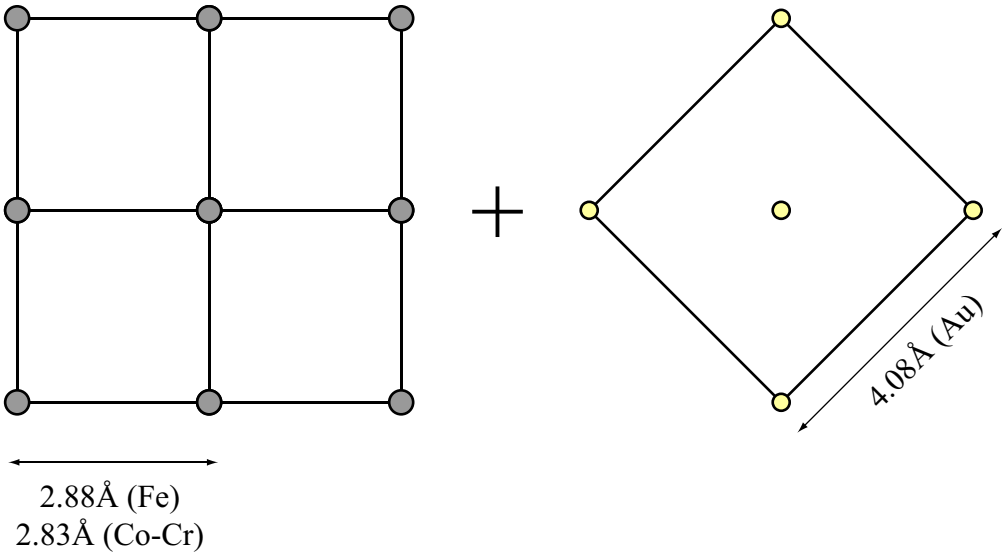


Figure 4.4: Lattice matching for bcc Co-Cr or Fe and fcc Au.

tageous.

One can also see from the HRTEM images that the gold layer was deposited epitaxially on both Fe and Co-Cr. The lattice constant of face-centered cubic (fcc) Au is 4.08 Å, much larger than that of either spin-aligning contact metal. How can the epitaxial growth be explained?

Figure 4.4 shows the top monolayer of the bcc Co-Cr or Fe as well as the beginning monolayer of the fcc Au. The lattice constant of Au may be 4.08 Å, but the nearest-neighbor difference is 2.89 Å. Au will therefore grow oriented at a 45° angle so that the [100] direction in Co-Cr or Fe aligns with the [100] direction of Au. The epitaxial growth of Au further supports the conclusion that the Co-Cr layer was bcc.

### 4.2.2 Proton Induced X-Ray Emission and Rutherford Backscattering

Because of different vapor pressures for Co and Cr during electron-beam evaporation, it was necessary to measure the alloy concentration of the Co-Cr film. To perform this analysis, proton induced X-ray emission and Rutherford backscattering (RBS) were employed.[3]

For both PIXE and RBS, $\alpha$ particles ($He^{++}$) are used to probe the properties of the

[3]PIXE and RBS analysis performed by Charles Evans & Associates.

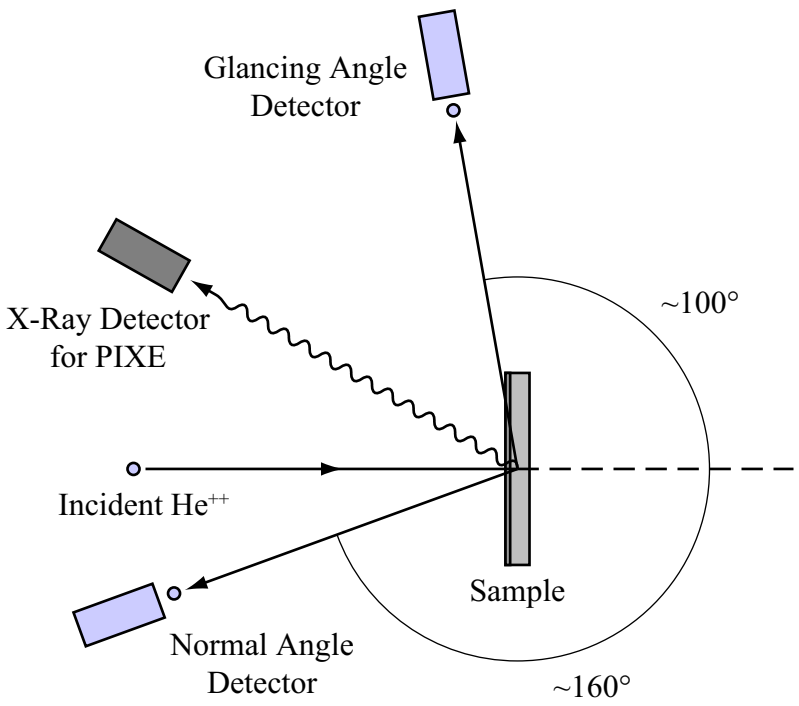


Figure 4.5: Schematic of the RBS and PIXE system. In RBS, the energy of backscattered $\alpha$ particles is measured and is used for sample composition and thickness determination. In PIXE, the X-ray spectrum (generated due to the interactions between the energetic $\alpha$ particles and core electrons in the sample) is measured and used to determine sample composition to within 1%. Angles shown are those used in the characterization of Sb0643-CoCr.

sample near the surface (see Figure 4.5). The 100 nA $He^{++}$ beam is provided by a particle accelerator, which energizes the particles to 2.275 MeV. As the $\alpha$ particles travel through the sample under test, they occasionally are scattered through Coulombic interactions with the constituent atoms. In PIXE, the $\alpha$ particle ionizes one of the core electrons of an atom. As electrons from higher atomic orbitals transition to the now vacant energy level, X-rays are emitted at characteristic energies. The X-ray spectrum is measured, allowing for determination of the sample composition to within 1%.

Rutherford backscattering, on the other hand, measures the energies of the backscattered $\alpha$ particles. For an $\alpha$ particle of mass $M_\alpha$ interacting with an atom of mass $M$, the ratio of the energy of the $\alpha$ particle just before the collision to that just after the collision is

given by the kinematic factor

$$K = \frac{E_{\text{scattered}}}{E_{\text{incident}}} = \left[ \frac{\sqrt{1 - \left(\frac{M_\alpha}{M} \sin\theta\right)^2} + \frac{M_\alpha}{M} \cos\theta}{1 + M_\alpha/M} \right]^2, \tag{4.1}$$

where $\theta$ is the scattering angle. This gives a characteristic scattering energy for a given angle, which allows for constituent element determination. Note that $E_{\text{incident}}$ in Equation 4.1 is not necessarily the beam energy, 2.275 MeV. As the particles travel through the sample, they lose a portion of their energy through interactions with the electrons and nuclei in the surrounding medium. Because of this, an $\alpha$ particle scattered from a particular atom at one depth in the sample will have a different energy than one scattered at the same angle from an identical atom at a different depth. The particles lose energy not only as they traverse the sample material to a scattering center, but also on the way back out of the specimen. Therefore, if the layer density is known the energy spread of the backscattered particles can be used to calculate layer thickness.

The probability that an ion will be scattered into a given solid angle is given by the scattering cross section

$$\frac{d\sigma}{d\Omega} = \left(\frac{Z Z_\alpha e^2}{4E_\alpha}\right)^2 \left(\frac{4}{\sin^4\theta}\right) \left[ \frac{\left[\sqrt{1 - \left(\frac{M_\alpha}{M} \sin\theta\right)^2} + \cos\theta\right]^2}{\sqrt{1 - \left(\frac{M_\alpha}{M} \sin\theta\right)^2}} \right], \tag{4.2}$$

where $Z$ and $Z_\alpha = 2$ are the atomic numbers of the target atom and the $\alpha$ particle, respectively. Typically, $M \gg M_\alpha$ so the $1/\sin^4\theta$ dependence dominates $d\sigma/d\Omega$. Because of this, measurement of large-angle deflections will yield higher signals.

The Co-Cr alloy composition in Sb0643-CoCr was determined by PIXE to be 12 at.% Cr and 88 at.% Co. Although on the low side, this falls within the range 10–27 at.% Cr required for perpendicular magnetization (see §3.2.3.2). The raw RBS data for this sample is shown in Figure 4.6 and the layer compositions and thicknesses derived from these data are shown in Figure 4.7. These measurements confirm that the aluminum concentration of the $Al_xGa_{1-x}As$ layer matched the design specification of 20%.

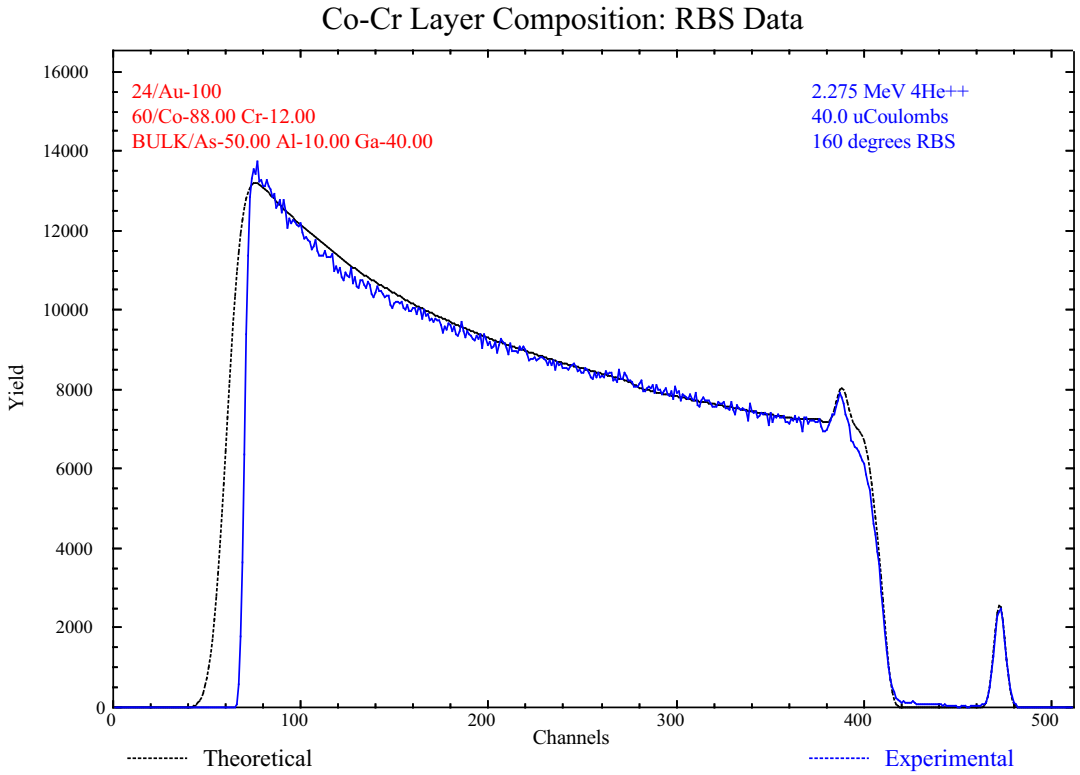


Figure 4.6: Raw RBS data from Sb0643-CoCr. The detector channels shown on the $x$-axis correspond to backscattered $\alpha$ particle energy. The peak seen near 470 results from the Au capping layer, the peak at ~390 is from the Co-Cr film, and the broad background from 80 to 420 is from the underlying $Al_{0.2}Ga_{0.8}As$.

| Density (RBS) | Percent Atomic Concentration | | | | | | Thickness (RBS) |
|---|---|---|---|---|---|---|---|
| ($10^{22}$ at./cm$^3$) | Al | Co | Cr | Ga | As | Au | (Å) |
| 5.90 | - | - | - | - | - | 100 | 24 |
| 8.89 | - | 88 | 12 | - | - | - | 60 |
| 4.97 | 10 | - | - | 40 | 50 | - | - |

Table 4.2: Layer thicknesses and composition as determined by RBS. The layer thicknesses were calculated using the assumed densities listed here. The density assumed for Co-Cr was a weighted average of the densities of Co and Cr based upon the alloy concentration.

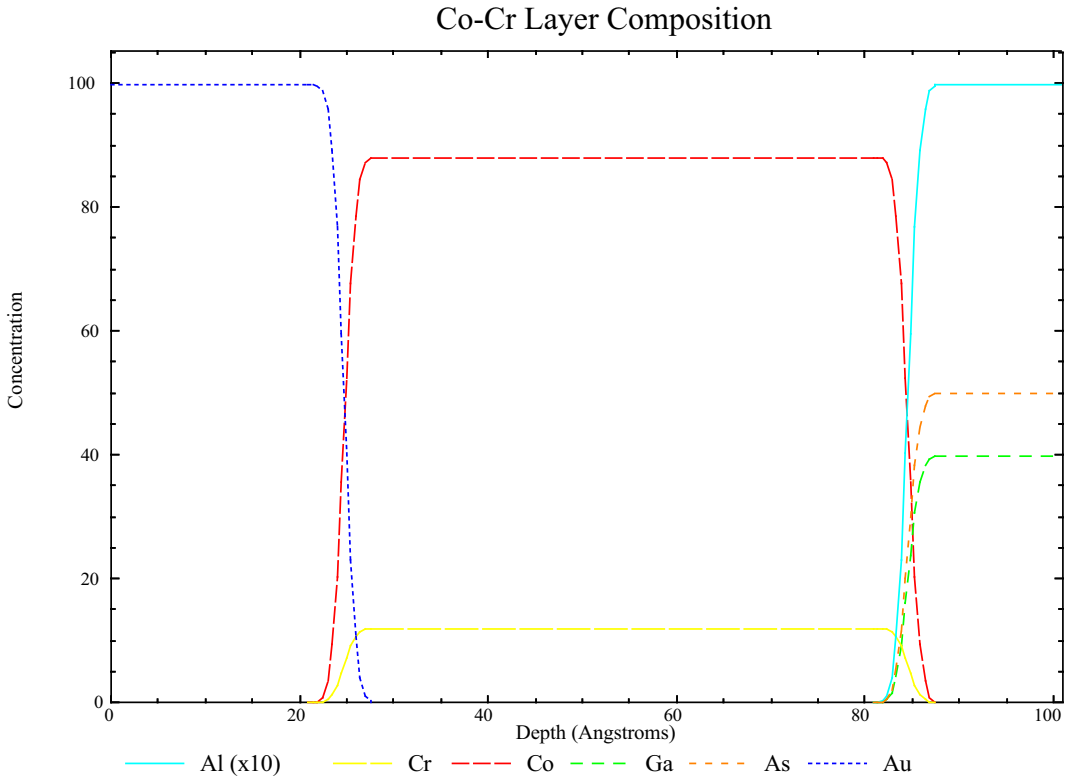


Figure 4.7: Layer thicknesses as determined by RBS. The Co-Cr layer thickness was determined by RBS to be 60 Å. This measurement technique, however, depends upon an assumed layer density and is not reliable unless the actual layer density is known.

Table 4.2 summarizes the PIXE and RBS results, including the layer densities used for thickness calculations. The layer density of Au was assumed to be its bulk value while that of the Co-Cr film was an average of that for bulk hcp Co and bcc Cr weighted by the alloy composition. Based on these assumed densities, Rutherford backscattering measured the Co-Cr thickness to be 60 Å and the Au thickness to be 24 Å. This is in contrast to the TEM measured thicknesses of 87 Å of Co-Cr and 32 Å of Au. Errors in the accuracy of the fit may account for some of this observed difference, but the precision of these fits were stated at 10% for Au and 20% for Co-Cr. How can this discrepancy be accounted for?

One possibility is that the thin film densities of the metallic layers are different from those assumed for the RBS thickness calculations because of the epitaxial growth of these materials. Armed with the knowledge of the film thicknesses from the direct TEM measurement, the actual layer densities can be calculated:

$$d_r = \frac{d_{\mathrm{RBS}} t_{\mathrm{RBS}}}{t_r}, \tag{4.3}$$

where $d_{\mathrm{RBS}}$ is the density assumed in the calculation of the RBS measured thickness, $t_{\mathrm{RBS}}$, and $t_r$ is the directly measured layer thickness. From this equation, the densities of the Co-Cr and Au films are $6.13 \times 10^{22}$ at./cm$^3$ and $4.43 \times 10^{22}$ at./cm$^3$, respectively. These densities would require $c$-axis lattice constants of 4.07 Å for Co-Cr and 5.64 Å for Au, 25–30% higher than the natural lattice spacing. This is clearly unphysical. Although density differences may account for a small error, this cannot be more that a couple of percent at most.

A mechanism that may shorten the thickness of a layer as measured by RBS is channeling (see Figure 4.8). If the crystal is aligned with respect to the beam of $\alpha$ particles, the energy loss due to glancing angle scattering events with the lattice will be suppressed. This serves to sharpen the energy peak as observed by the detector, making the material appear to be thinner than it actually is. Samples are typically tilted and rotated to reduce the effects of channeling. For this specific measurement, the specimen was tilted off-axis by 3°. This angle is sufficient to expose the atomic nuclei in a column along a channeling path.[4]

[4]The scattering cross section, given by integrating Equation 4.2 over solid angle, is 1129 barnes for the

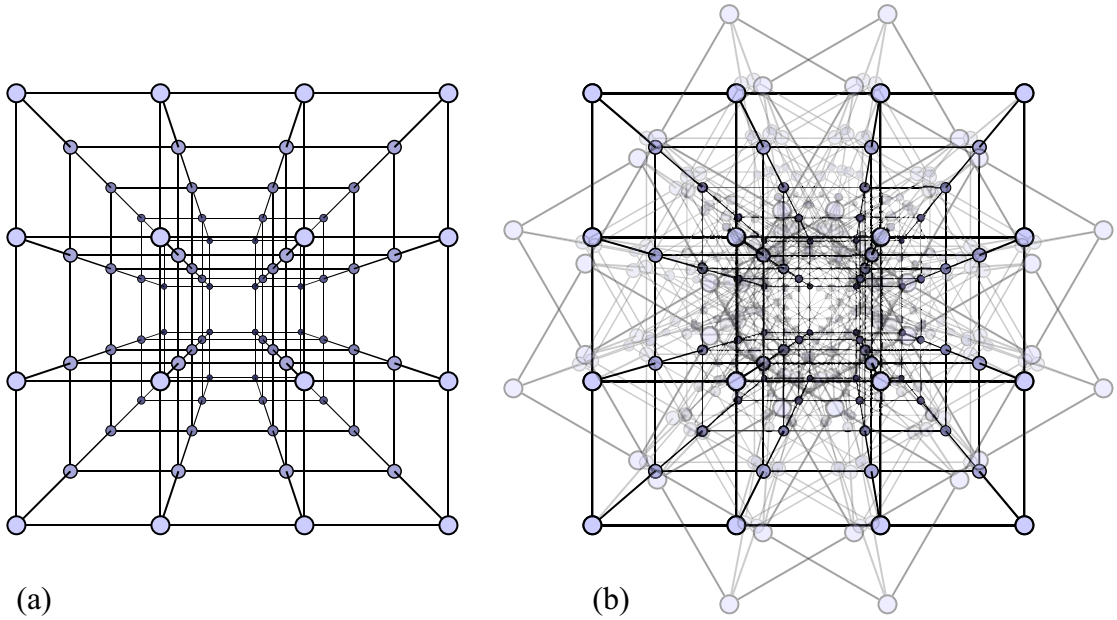


Figure 4.8: Channeling effects in RBS. (a) A straight path can be seen down the [100] direction of this simple cubic lattice. (b) Tilting and rotating obscures the channel.

The reason for the difference in measured thicknesses between RBS and TEM remains uncertain. The thicknesses as obtained from the HRTEM images, however, are more trustworthy because they are direct physical measurements. These values are therefore used for any subsequent calculations.

## 4.3 Magnetic Characterization

As mentioned previously (§3.2.3.2), Co-Cr was selected as a spin-aligning contact because it exhibits perpendicular magnetism for a certain range of alloy compositions. The use of a good perpendicular magnet as a spin injector should obviate the need for large external magnetic fields to be applied during spin-LED spin injection measurements. Unfortunately, the HRTEM micrographs of the Co-Cr/$Al_{0.2}Ga_{0.8}As$ interface indicate epitaxial bcc growth of the metal layer. Despite the negative implications of this for perpendicular magnetism in Sb0643-CoCr, confirmation of the magnetization, or lack thereof, was necessary. The magnetic properties of Sb0643-CoCr were therefore studied by vibrating sample magnetometry

Co-Cr alloy.

(VSM).[5]

In VSM, the sample is placed between the poles of an electromagnet and is oscillated with an amplitude $A$. Sensing coils placed near the sample measure the emf induced by these oscillations. The voltage in the coils is given by

$$V = mAfS, \tag{4.4}$$

where $m$ is the magnetic moment of the sample, $f$ is the frequency of vibration, and $S$ is the sensitivity of the VSM sensing coils. The instrument used for these measurements was a Lake Shore Model 7400 VSM. For a sample size of 10 mm × 10 mm, the rms noise for this VSM is 0.28 μemu and the signal-to-noise ratio (SNR) is 79.3 at a data collection rate of 10 s/pt.

In characterizing the magnetic properties of a sample, four quantities are of interest:

$H_c$ coercive field, the field required to demagnetize the material

$M_s$ saturation magnetization, the maximum magnetization possible for the material

$M_r$ remnant magnetization or retentivity, the magnetization that remains in the sample when the external field is turned off

$S_r \equiv \frac{M_r}{M_s}$ squareness, a measure of the ability of the material to retain its magnetization.

Hysteresis loops, where the magnetization of the sample as a function of the applied magnetic field is measured from saturation in one direction to saturation in the opposite direction and back again, are useful in identifying these four quantities. Ideally, a good permanent magnet will have high coercivity, high saturation magnetization, high remnant magnetization, and a squareness of 1. Also, the demagnetization curve, or second quadrant of the hysteresis loop, should be nearly linear.

Hysteresis loops for the in-plane and out-of-plane magnetizations of Sb0643-CoCr are shown in Figures 4.9 and 4.10. The sample holder magnetization has been subtracted

[5] VSM measurements were conducted by Brad Dodrill at Lake Shore Cryotronics.

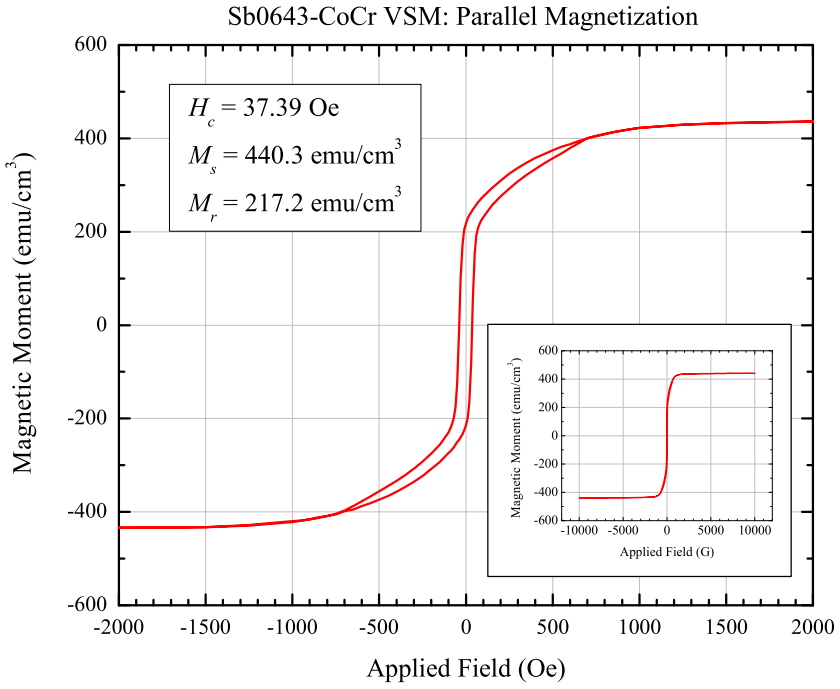


Figure 4.9: In-plane magnetization of Sb0643-CoCr. The inset shows the full range of measurement.

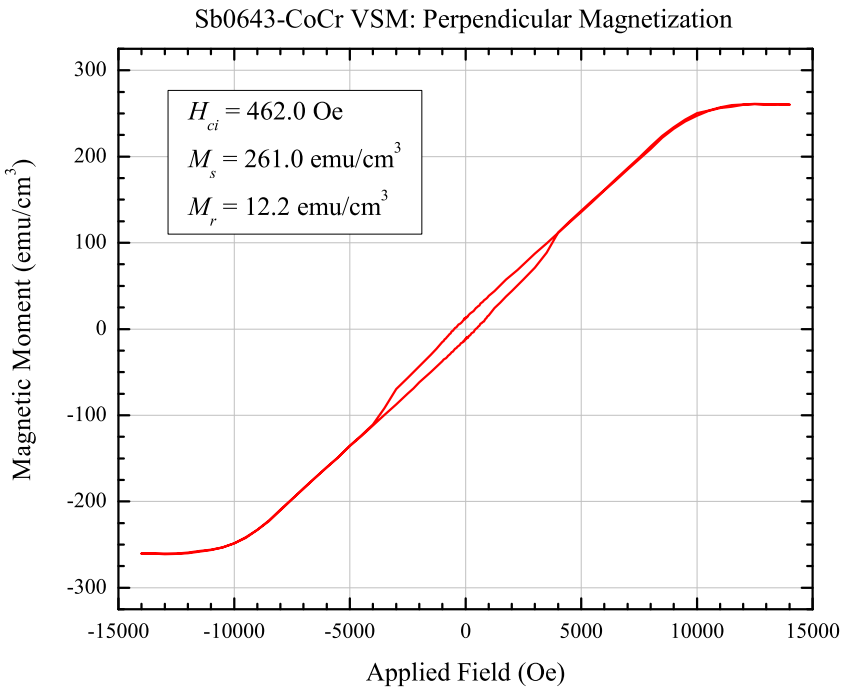


Figure 4.10: Perpendicular magnetization of Sb0643-CoCr.

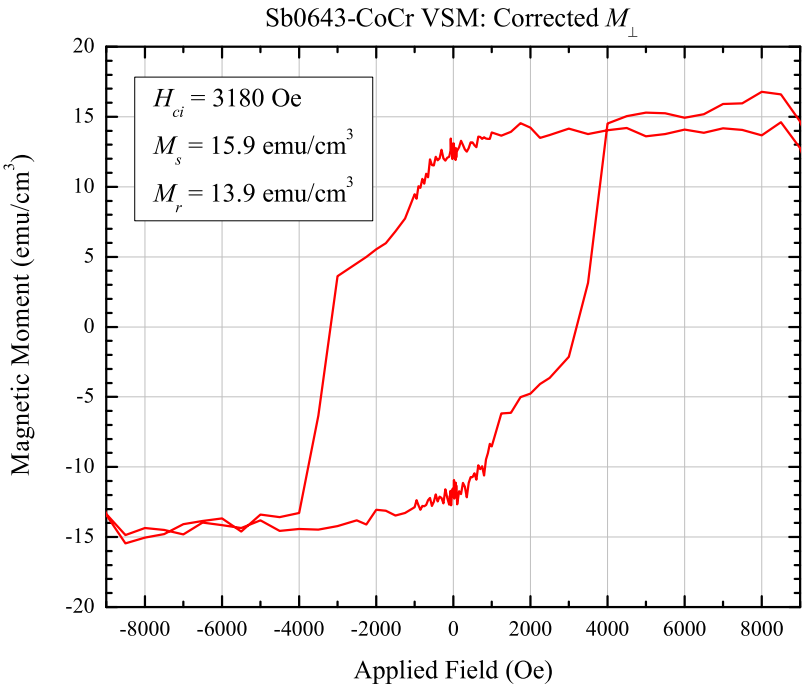


Figure 4.11: Perpendicular magnetization of Sb0643-CoCr with paramagnetic correction.

from these data and a linear correction applied in order to account for the diamagnetic contribution of the substrate. Inspection of the out-of-plane magnetization reveals a small permanent moment that lies on top of a linear paramagnetic background. This is not entirely surprising because of the composition of the specimen and its crystal structure. The magnetization of the film with this paramagnetic background subtracted off is displayed in Figure 4.11.

The magnetic properties of Sb0643-CoCr are summarized in Table 4.3. The measured saturation magnetization of the Co-Cr film was 440.3 emu/cm$^3$. These results are in line with those of Oldham [6]. For a $Co_{0.94}Cr_{0.06}$ sample he measured $H_{c,\parallel}$ = 46.12 Oe and $H_{c,\perp}$ = 578.18 Oe while for a $Co_{0.83}Cr_{0.17}$ sample he measured $H_{c,\parallel}$ = 47.79 Oe and $H_{c,\perp}$ = 264.83 Oe, both grown on Si (100) substrates. The in-plane coercive field is slightly smaller for Sb0643-CoCr, but the out-of-plane magnetization lies between the values he observed.

| Applied Field Orientation | $H_c$ (Oe) | $M_s$ (emu/cm$^3$) | $M_r$ (emu/cm$^3$) | $S_r$ |
|---|---|---|---|---|
| $H_\parallel$ | 37.39 | 440.3 | 217.2 | 0.49 |
| $H_\perp$ | 462.0 | 261.0 | 12.2 | 0.047 |
| $H_\perp$ (corrected) | 3180 | 13.9 | 12.2 | 0.87 |

Table 4.3: Magnetic properties of Sb0643-CoCr. The perpendicular magnetization corrected for the paramagnetism of Co shows good squareness, but small saturation magnetization.

## 4.4 Electrical Characterization

### 4.4.1 Current-Voltage Measurements

The current-voltage characteristics of an ideal abrupt *pn* junction diode are given by

$$J = J_s\left(e^{qV/kT} - 1\right) \tag{4.5}$$

$$J_s = \frac{qD_n p_{n0}}{L_p} + \frac{qD_p n_{p0}}{L_n}, \tag{4.6}$$

where $J$ is the current density in the diode, $D_{n(p)}$ is the diffusion coefficient for electrons (holes), $L_{p(n)} = \sqrt{D_{p(n)}\tau_{p(n)}}$ is the minority carrier diffusion length, and $p_{n0}$ ($n_{p0}$) is the minority carrier concentration at thermal equilibrium [7].

Equation 4.5, the ideal diode equation, was derived under the assumption that no recombination current exists in the space-charge region of the diode and that the series resistance, $r_s$, of the diode is small. In general, these assumptions are not always valid. Factoring in the effects of series resistance and recombination in the depletion region, a more general expression for the current density in a real *pn* diode is

$$J = J_s\left[\exp\left(\frac{q\left(V - JAr_s\right)}{\eta kT}\right) - 1\right], \tag{4.7}$$

where $A$ is the device area and $\eta$ is the ideality factor. When the diffusion current dominates, $\eta = 1$, while $\eta = 2$ if the current is dominated by recombination. Under the conditions $V \gg JAr_s$, $qV/\eta kT \gg 1$, the current density will be linear on a semilog plot and the ideality factor can be calculated by the slope of this line.

The current-voltage characteristics for Sb0643, Sb0643-Fe, and Sb0643-CoCr at room

| | Series Resistance (Ω) | | |
|---|---|---|---|
| Radius (μm) | Sb0643 | Sb0643-Fe | Sb0643-CoCr |
| 100 | 3.53 | 3.76 | 4.42 |
| 150 | 3.83 | 4.20 | 4.71 |
| 200 | 4.80 | 4.01 | 5.46 |

Table 4.4: Diode series resistance at RT.

temperature (RT) are displayed in Figures 4.12–4.14. Each plot contains the current density as a function of applied bias for the 200, 150, and 100 μm devices on each sample. The ideality factor for each device is also indicated in the legend of each plot. A significant difference between the performance of the 200 μm device and the 150 and 100 μm devices in Sb0643 is attributed to processing variations. Reverse bias breakdown, as determined by visual inspection of a linear plot of the current-voltage characteristics, occurred at −4.8 V for Sb0643, −4 V for Sb0643-Fe, and −3.4 V for Sb0643-CoCr.

It is interesting to note the differences between the *JV* characteristics for the three samples. Aside from the processing error in the 200 μm device, Sb0643 exhibits much lower reverse bias leakage current than either Sb0643-Fe or Sb0643-CoCr. This is because the *n*-type contact area for this sample is much smaller than for either the Fe or Co-Cr samples.

The series resistance of the diode can be calculated through knowledge of the conductivity, $G = dI/dV$, where $I = JA$ is the total current flowing through the device. Differentiating Equation 4.7 with respect to $V$ and rearranging the terms gives [8]

$$\frac{I}{G} = \frac{\eta kT}{q} + Ir_s. \tag{4.8}$$

The slope of a plot of $I/G$ versus $I$ yields $r_s$. The calculated series resistance values for the three sets of devices can be found in Table 4.4.

### 4.4.2 Current-Voltage Temperature Dependence

Because the spin injection measurements for these samples was to be performed at low temperature, the temperature dependence of the 200 μm diodes' electrical behavior was

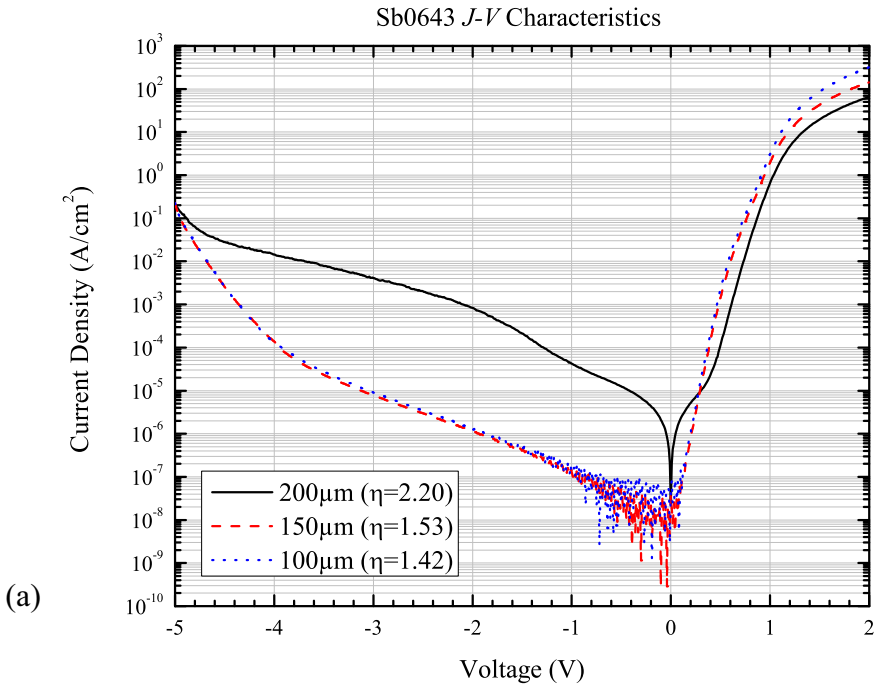


(a)

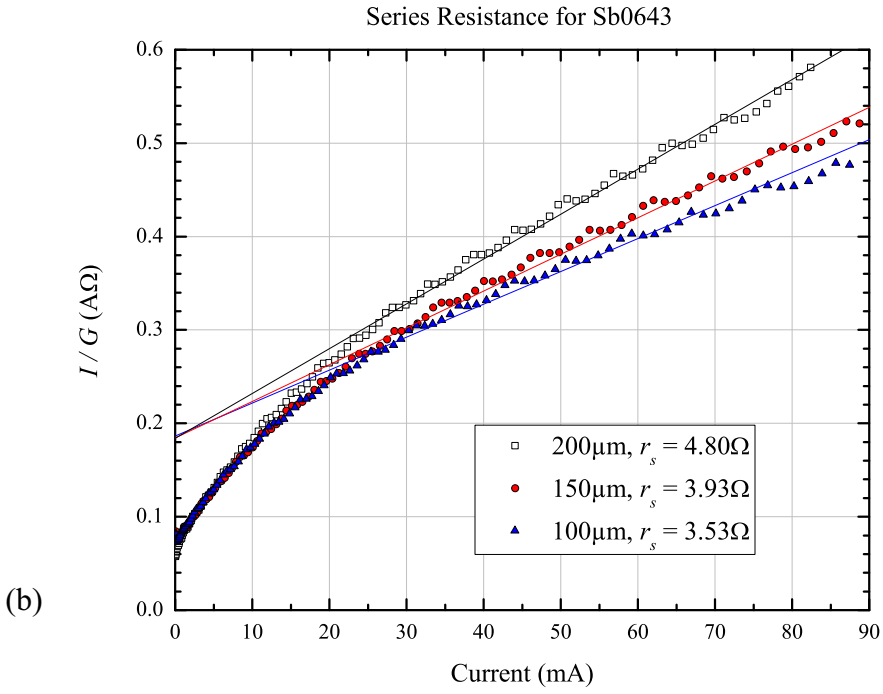


(b)

Figure 4.12: Sb0643 *JV* characteristics and series resistance at RT. (a) The significant difference in performance between the 200 μm device and the 150 μm and 100 μm devices is due to variations in device processing. (b) Series resistance for Sb0643.

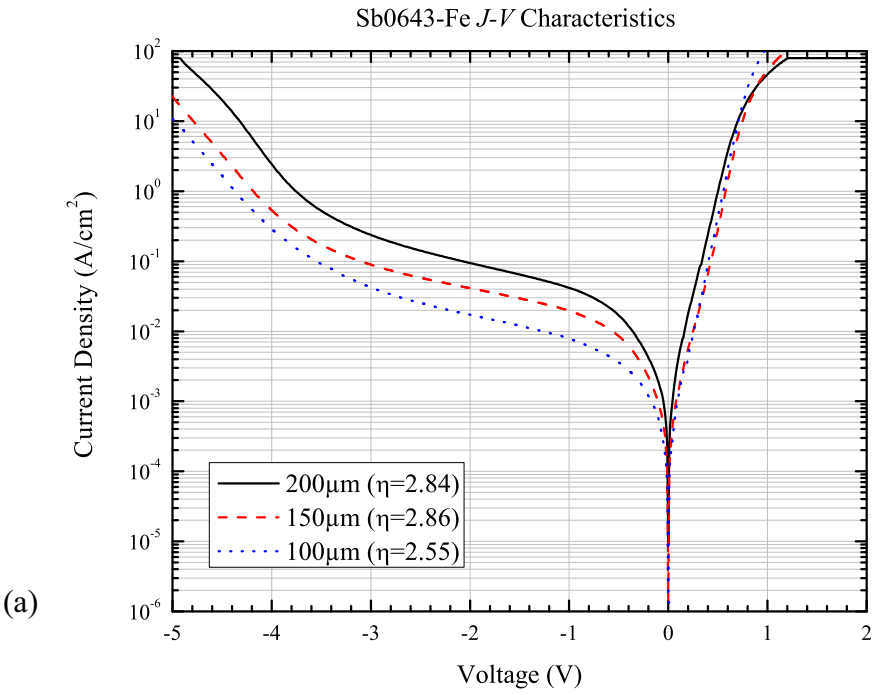


(a)

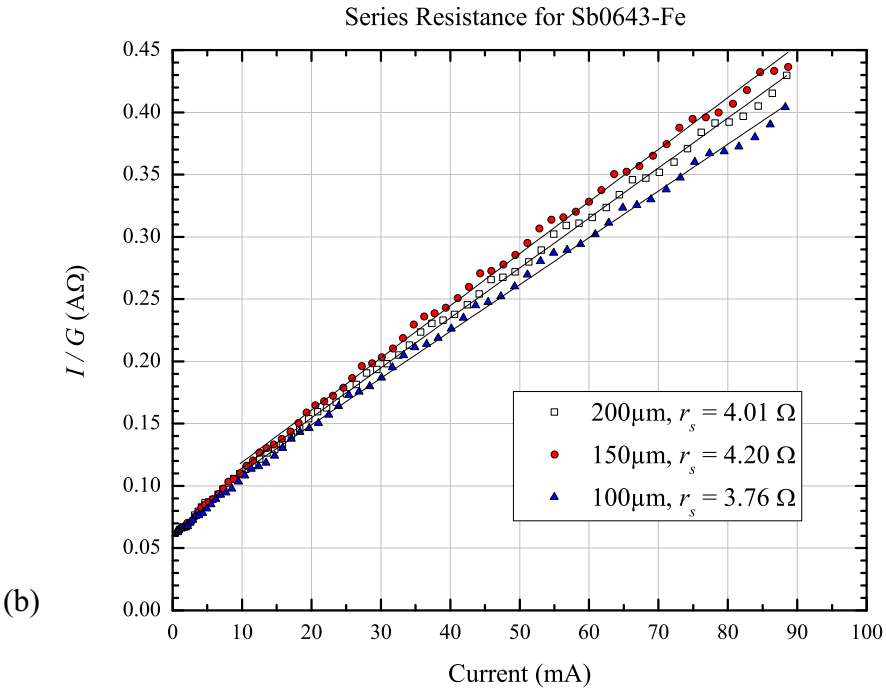


(b)

Figure 4.13: Sb0643-CoCr *JV* characteristics at RT.

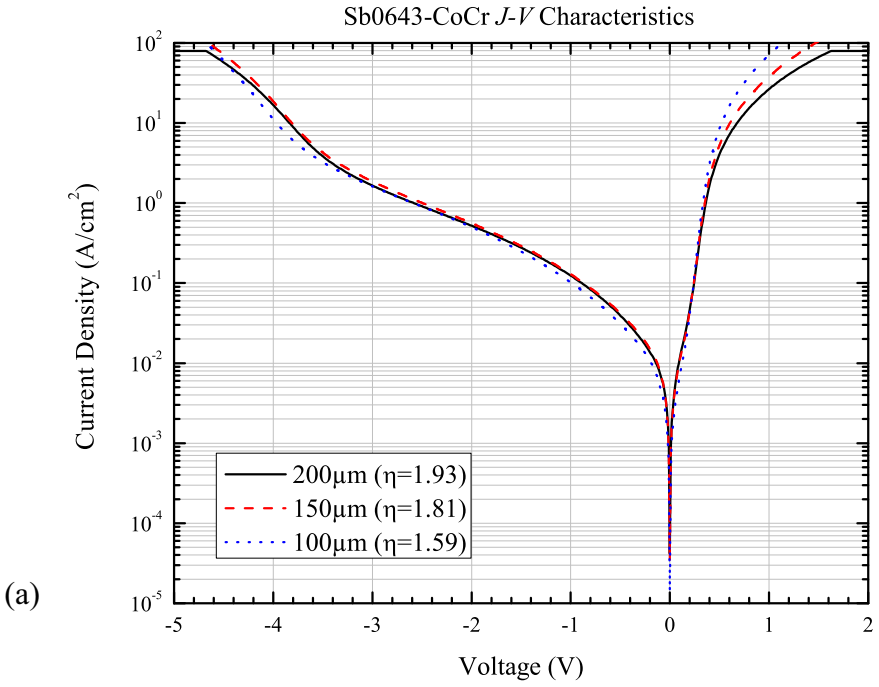


(a)

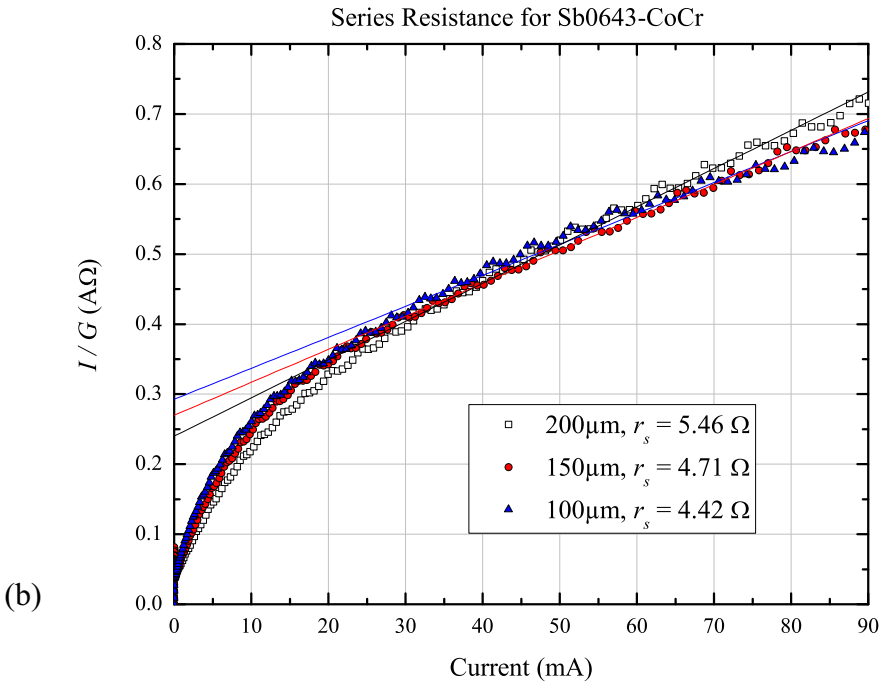


(b)

Figure 4.14: Sb0643-CoCr *JV* characteristics and series resistance at RT.

| | | Ideality Factor $\eta$ | | |
|---|---|---|---|---|
| $T$ (K) | $kT/q$ (eV) | Sb0643 | Sb0643-Fe | Sb0643-CoCr |
| 300 | 0.0259 | 1.28 | 1.31 | 1.10 |
| 260 | 0.0225 | 1.42 | 1.33 | 1.13 |
| 220 | 0.0191 | 1.44 | 1.39 | 1.13 |
| 180 | 0.0156 | 1.45 | 1.55 | 1.18 |
| 140 | 0.0121 | 1.64 | 1.91 | 1.25 |
| 100 | 0.00867 | 1.81 | 3.21 | 1.41 |
| 84 | 0.00728 | 2.21 | 3.79 | 1.60 |

Table 4.5: Diode ideality factors at different temperatures. The ideality factor increases for decreasing temperature, indicating that the recombination current is becoming a larger fraction of the overall device current.

studied. Figures 4.15–4.17 display the $JV$ as well as $GV$ characteristics for a range of temperatures from 300 K to 84 K. As expected, current displayed an overall decrease with decreasing temperature. This reflects a change in the ideality factors, as shown in Table 4.5. The ideality factor for each sample monotonically increases because the device current shifts from being diffusion dominated to space-charge recombination dominated at lower temperatures.

## 4.5 Optical Characterization

The optical spectrum of an unprocessed sample of Sb0643 was probed via photoluminescence (PL). For these measurements, the 514.5 nm line of a 5 W maximum power $Ar^+$ ion laser was used as an excitation source. At this wavelength, the absorption length of the laser light is 146 nm in $Al_{0.2}Ga_{0.8}As$ and 114 nm in GaAs at room temperature, so the entire device structure was illuminated by the laser. The laser was chopped at 1.6 kHz for lock-in detection and the spot size of the beam at the sample was $\sim$10 mm$^2$. A CVI Laser CM110 1/8 m monochromator was used for spectral resolution and a Hamamatsu R943-02 GaAs photomultiplier tube was used as for detection.

The PL spectra for Sb0643 at room temperature, 77 K, and 4.2 K are shown in Figure 4.18. The intensities of the spectra have been normalized in this plot to the quantum well luminescence peak. The separation between the quantum well and bulk peaks becomes

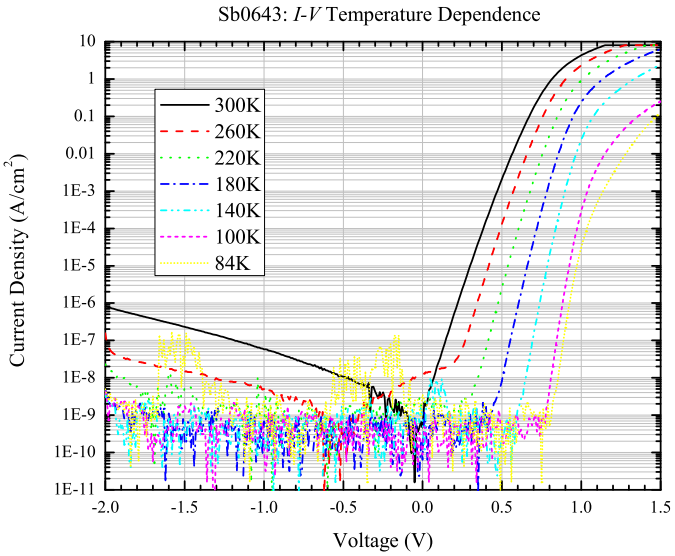


Figure 4.15: Temperature dependence of the Sb0643 *J-V* characteristics.

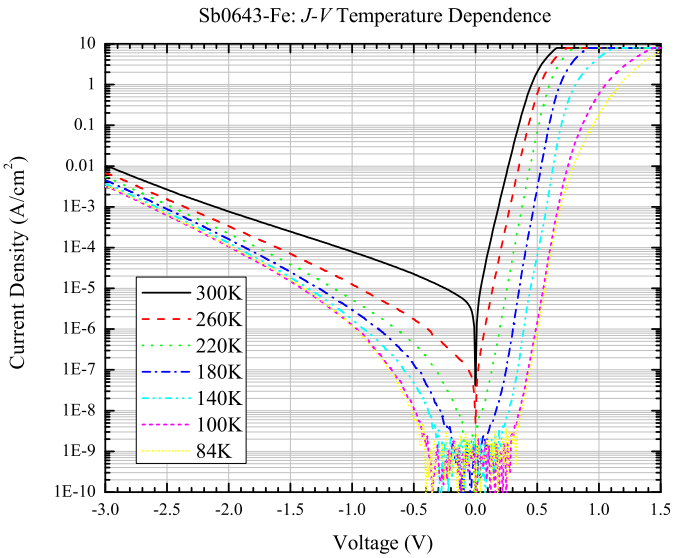


Figure 4.16: Temperature dependence of the Sb0643-Fe *J-V* characteristics.

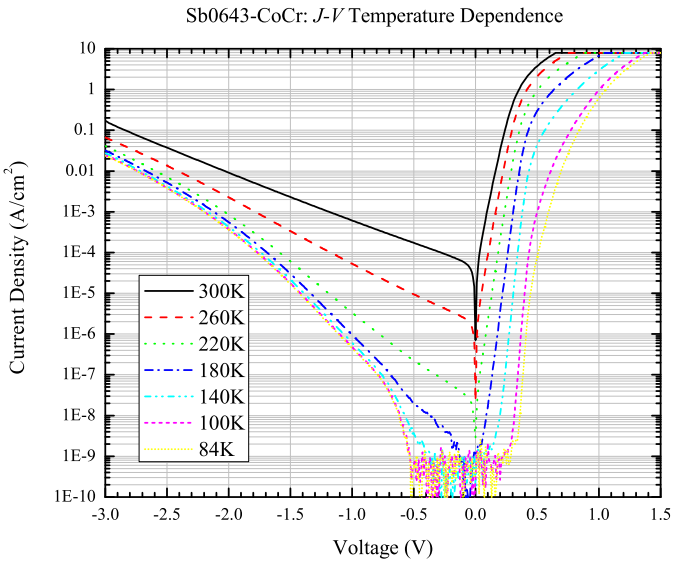


Figure 4.17: Temperature dependence of the Sb0643-CoCr *J*-*V* characteristics.

| Temperature (K) | QW Peak (eV) | FWHM (meV) | $kT$ (meV) |
|---|---|---|---|
| 300 | 1.481 | 28.3 | 25.9 |
| 77 | 1.533 | 13 | 6.7 |
| 4.2 | 1.537 | 10 | 0.36 |

Table 4.6: Quantum well PL peak properties at 300 K, 77 K, and 4.2 K.

more pronounced as temperature decreases. The difference between the low energy tail of the quantum well peak and the $Al_{0.2}Ga_{0.8}As$ peak is only truly discernible at 4.2 K. The quantum well line width is smaller than that of the bulk because the confinement of the well reduces the number of degrees of freedom for carriers in that region. The full width at half-maximum (FWHM) of the quantum well peak is equal to $kT$ at room temperature.

Electroluminescence (EL) from the processed LEDs was not observable at room temperature. Low temperature measurements did reveal strong luminescence signals for Sb0643 and Sb0643-Fe, but that of Sb0643-CoCr was significantly weaker. A current of 10 mA was used for both Sb0643 and Sb0643-Fe, but ten times that amount (100 mA) was required in order to observe the EL from Sb0643-CoCr.

Spectra for the 200 μm devices for Sb0643, Sb0643-Fe, and Sb0643-CoCr are shown

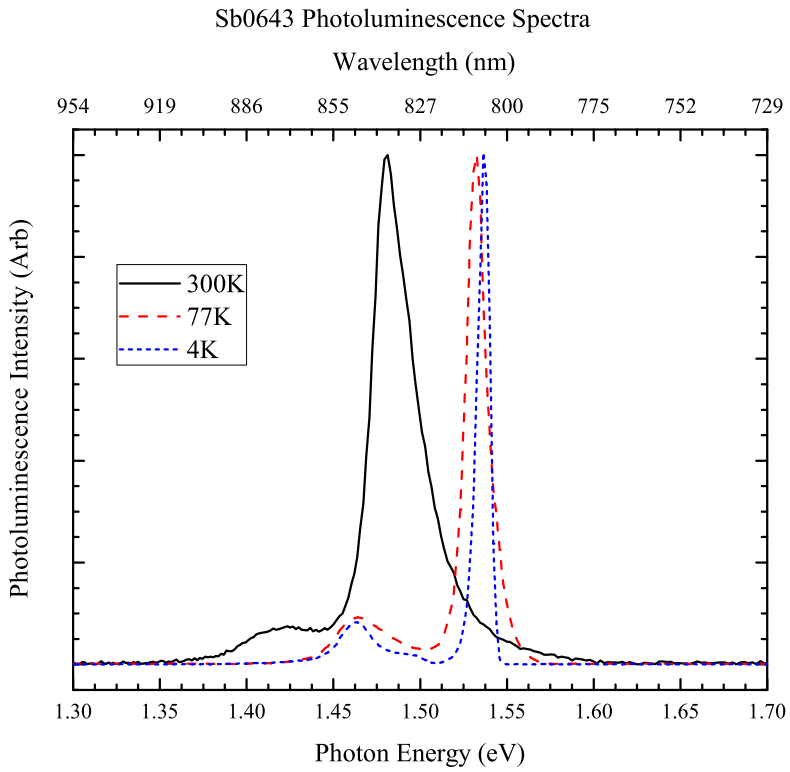


Figure 4.18: Photoluminescence spectrum of Sb0643 at 300 K, 77 K, and 4.2 K. The ratio of quantum well to bulk luminescence peaks remained constant as a function of temperature. The intensities of the spectra for the three different temperatures have been normalized for ease of peak comparison. Excitation was from the 514.5 nm line of a 5 W $Ar^+$ ion laser.

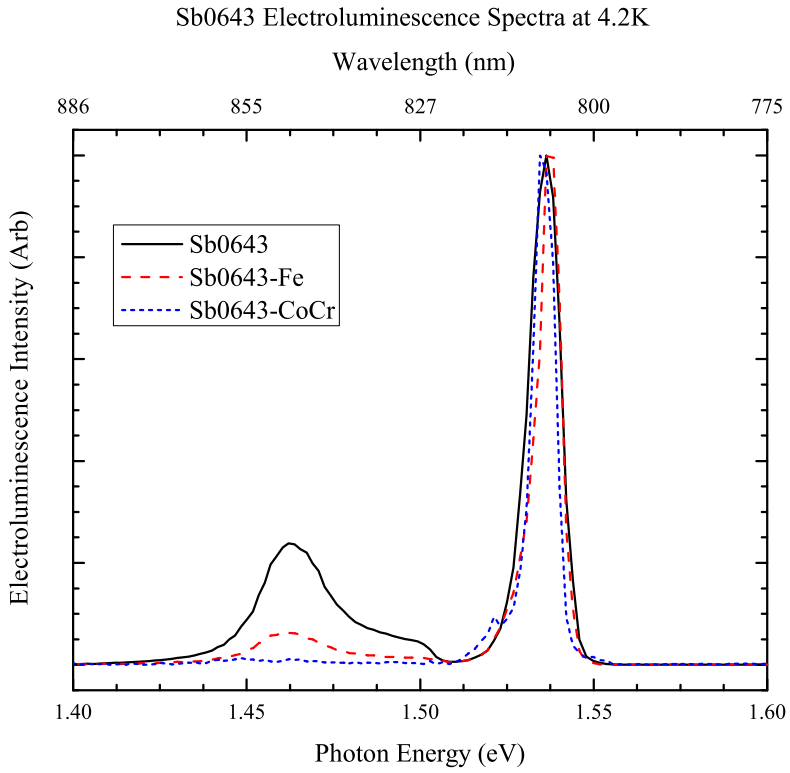


Figure 4.19: Electroluminescence spectra at 4.2 K for Sb0643, Sb0643-Fe, and Sb0643-CoCr. Device currents were 10 mA for both Sb0643 and Sb0643-Fe, and 100 mA for Sb0643-CoCr. The bulk luminescence is not visible in Sb0643-CoCr due to increased absorption in the spin aligning contact relative to the other two samples.

in Figure 4.19. These were the measured spectra for the devices that were used for the spin injection measurements to be discussed in §5.3. As in the case with PL, the data were normalized to the quantum well luminescence peak. The bulk GaAs and $Al_{0.2}Ga_{0.8}As$ peaks are not even visible in this spectrum. As mentioned in §3.2.3.1, the absorption length in Co at 1.5 eV is 13.1 nm as compared with 16.6 nm for Fe. At lower energies the difference is even higher [9]. The FWHM for each of the quantum well EL peak in each sample was 8 meV and the locations of each of the peaks agreed with the PL results.

## 4.6 Summary

The material, magnetic, electrical, and optical properties of the Sb0643 and the related spin-aligning samples were studied in preparation for a measurement of spin injection in these devices. It was found that the EBE-deposited Fe and Co-Cr films were both deposited epitaxially on the semiconductor structure and that the semiconductor structure matched its design parameters well. Unfortunately, the epitaxial growth of Co-Cr prevented the formation of the microstructure needed for good perpendicular magnetization. Regardless, the high value of spin polarization at the Fermi level in Co (see Table 3.2) makes this film an interesting one to study via spin-LED injection experiments.

The Co-Cr alloy composition was determined to be 12% Cr by PIXE measurements. Rutherford backscattering confirmed these findings and gave layer thicknesses of 60 Å for Co-Cr and 24 Å for Au, in contrast to 87 Å for Co-Cr and 32 Å for Au as measured directly by HRTEM.

The lack of perpendicular magnetism for the Co-Cr film as predicted by HRTEM was confirmed by VSM. Although strong perpendicular magnetism was not observed, the perpendicular saturation magnetization was found to be 261 emu/cm$^3$.

Electrically, the three sets of samples displayed acceptable diode characteristics. Although some variations existed in device performance, the diode idealities were found to lie within the range $1.42 < \eta < 2.86$ at room temperature. As a function of temperature, diode ideality was found to increase monotonically as temperature decreased, showing that recombination current in the space-charge region of these devices increased in proportion to the diffusion current.

The quantum well luminescence peak showed up as the strongest contribution to both PL and EL spectra. Although room temperature electroluminescence was not observable, the spectra were strong at 4.2 K, the temperature at which the spin injection measurements were to be performed.

# References

[1] B. Fultz and J. M. Howe, *Transmission Electron Microscopy and Diffractometry of Materials*, 2 ed. (Springer-Verlag, New York, 2002).

[2] D. B. Williams and C. B. Carter, *Transmission Electron Microscopy: A Textbook for Materials Science* (Plenum Press, New York, 1996), Vol. 3.

[3] Z. Ding, P. M. Thibado, C. Awo-Affouda, and V. P. LaBella, J. Vac. Sci. Technol. B **22**, 2068 (2004).

[4] C. Kittel, *Introduction to Solid State Physics*, 7th ed. (John Wiley & Sons, Inc., New York, 1996).

[5] C. J. Palmstrom, C. C. Chang, A. Yu, G. J. Galvin, and J. W. Mayer, J. Appl. Phys. **62**, 3755 (1987).

[6] N. C. Oldham, Ph.D. thesis, California Institute of Technology, 2004.

[7] S. M. Sze, *Physics of Semiconductor Devices*, 2nd ed. (John Wiley & Sons, Inc., New York, YEAR).

[8] D. K. Schroder, *Semiconductor Material and Device Characterization*, 2 ed. (John Wiley & Sons, Inc., New York, 1998).

[9] *Handbook of Chemistry and Physics*, edited by D. R. Lide (CRC Press, Boca Raton, 2003).

# Chapter 5 Spin Injection Experiment: Design and Measurement

## 5.1 Introduction

The polarization of emission from the spin-LED was modeled (Chapter 2) and an LED designed, fabricated (Chapter 3), and characterized (Chapter 4). The critical parameter for a spin-LED, though, is the circular polarization of its electroluminesce. This chapter describes the efforts to achieve this goal. The experimental apparatus employed for Stokes polarimetry is discussed in §5.2, including a description of the apparatus itself as well as the measurement procedure. The spin injection results for the Fe, Co-Cr and control samples are presented and an analysis of these data is given in §5.3.

## 5.2 Experiment Design

As discussed previously, the circular polarization of electroluminescence from an electron-hole recombination event is intimately tied to the spin state of the electron involved in that process (see §2.2.1.3). A method for measuring the polarization state of the radiation from these devices is therefore needed in order to characterize spin injection. A diagram of the setup that was devised to accomplish this task is displayed in Figure 5.1.

### 5.2.1 Measurement Apparatus

The dewar system was a Janis Model 14CNDT custom cryostat designed with large optical access for increased light collection. The windows were ZnSe to enhance infrared and far infrared transmission (not necessary for this particular experiment). Temperature control of the sample was provided by flow of liquid helium and a heating element placed on the

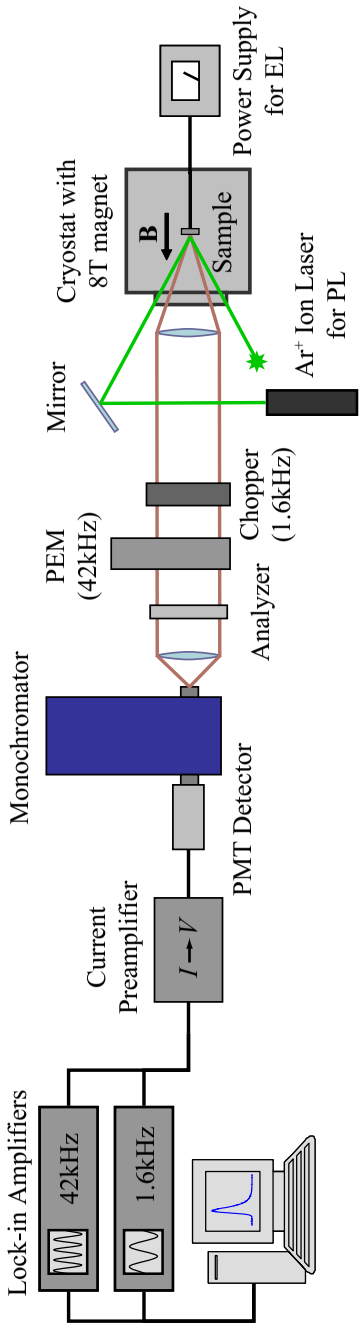


Figure 5.1: Schematic diagram of the spin injection measurement setup.

sample mount. Current was supplied to the LEDs by a Keithley 237 Source Measurement Unit operating in current sourcing mode.

An American Magnetics superconducting magnet with a maximum magnetic field of 8 T provided the field necessary to orient the contact magnetization perpendicular to the growth plane. Only field operation in the direction of light emission (as indicated in Figure 5.1) was possible due to a non-operational current reversing switch.[1] Field strength was monitored by a Hall magnetometer placed adjacent to the sample on the sample mount. References [1–4] detail the cryostat cool-down procedure and magnet operation.

A 50 mm diameter lens with a focal length of 20 cm ($f/\# = 4$) placed directly outside the cryostat window provided beam collimation while a second 50 mm diameter lens with a 5 cm focal length focused the beam onto a monochromator for spectral analysis. The monochromator was a CVI laser CM110 1/8 m model equipped with gold-plated mirrors for increased transmission in the infrared. Gold-plated optics were used in hopes to increase the observed signal because the electroluminescence spectra of the samples were not visible at room temperature. The slit widths of the monochromator were set to 0.15 mm and the grating ruling was 600 g/mm, giving an overall resolution of $\sim 1$ nm at a wavelength of 800 nm. A mechanical chopper operated at 1.6 kHz provided signal modulation for lock-in detection of the luminescence intensity.

Also included in the optical train were a photoelastic modulator (PEM) operating at 42 kHz and an analyzer (a linear polarizer optimized for near infrared operation) oriented at $-45^\circ$ from horizontal. The effect of this combination of optical elements was to generate intensity fluctuations at the detector that allowed for the light polarization to be measured (see Appendix B for a the PEM theory of operation). Circular polarization, described by the Stokes parameter $V$, was proportional to the component of the intensity modulated the operation frequency of the PEM while linear polarization, the Stokes parameter $U$, was proportional to the the component at twice that frequency (Appendix A reviews the Stokes parameters). The complete polarization state of the light could be measured by rotating the

[1] The voltages monitored by the op-amp circuit that drives the current reversing switch were out of specification. This circuit sensed a non-existent current in the superconducting coils and would therefore not allow polarity reversal.

combination of the PEM and analyzer by an angle of 45° to measure $Q$[2], but this was not done because the linear components of the polarization were not of interest. One advantage of using this scheme for Stokes polarimetry is that the polarization of the light entering the detection system is held constant. Polarization-dependent effects in the monochromator and photodetector are therefore not an issue.

A Hamamatsu R943-02 GaAs photomultiplier tube (PMT) was used for detection. The photocurrent produced by the PMT was converted into a voltage by a Stanford Research Systems SR570 Low-Noise Current Preamplifier. The output of the current preamp was fed into two separate lock-in amplifiers using the reference frequencies of the chopper and PEM to measure $I$ and $V$. Data from the lock-in amplifiers was recorded by a computer connected to the instruments via a GPIB interface. RS232 connections to the monochromator and PEM from the same computer also controlled these devices. Computer control was accomplished via a LabView virtual instrument that was written for this task.

### 5.2.2 Measurement Procedure

Once a sample was loaded into the cryostat, the sample space was cooled to 4.2 K by the flow of liquid helium. After reaching this temperature, the sample orientation was fixed so that illumination of the sample by an external lamp produced an image of the devices on the entrance slit of the monochromator. The monochromator was then set to the quantum well luminescence peak, 807 nm, and additional alignment of the lenses was performed to optimize the EL signal.

The intensity of the light as measured by the detector is [5]

$$I_{\text{det}} = I + U\left[J_0(A) - 2J_2(A)\cos(2\omega t)\right] + 2V J_1(A)\cos(\omega t), \tag{5.1}$$

where $I$ is the intensity of the light before going through the polarimetry setup, $J_k(x)$ are Bessel functions, $A$ is the amplitude of retardation caused by the PEM, and $\omega = 2\pi f$ is the angular frequency of operation for the PEM. It can be noted from this equation that the

[2]The same task could be accomplished by introducing a half-wave plate into the optical train between the PEM and analyzer. The axis of this optical element would be aligned with the axes of the PEM to measure $U$, or rotated by an angle of 22.5° to measure $Q$.

signal for $V$ as measured by lock-in amplification will be maximized when the retardation amplitude, $A$, maximizes $J_1$. This maximum occurs at slightly greater than quarter-wave retardation.

The quantity of interest in this experiment is the normalized Stokes parameter $V/I$. However, because of losses due to the frequency dependence of the gain in the signal conditioning electronics, the relationship between $I$ and $V$ is not as simple as Equation B.9 would indicate. A correction factor $C$ is necessary to relate $V_{\text{meas}}/I_{\text{meas}}$ as measured to the correct value, $V/I$. Prior to each run, calibration was done to determine the value of $C$. This was accomplished by introducing a GaAs linear polarizer and quarter-wave plate into the optical train to produce light known to be 100% circularly polarized. Typical correction factors were around 1.5.

Once the calibration was performed, measurements of $V/I$ were made as a function of the exernally applied magnetic field up to 2 T to ensure that the Fe and Co-Cr films would achieve saturation [6]. Twenty data points were collected at each field strength at a collection rate of 1 pt/s.

## 5.3 Spin Injection Measurement and Analysis

The results for the spin injection measurements for Sb0643, Sb0643-Fe, and Sb0643-CoCr are shown in Figure 5.2. The error bars for Sb0643-CoCr are large compared to those for the other two samples because of the much lower EL intensity.

As these results indicate, no spin injection was observed in these devices. Data were also recorded at an applied field strength of 4 T to ensure that saturation of the contact magnetization had been reached. These data also indicated zero spin injection.

Although a similar structure by Hanbiki [6] with Fe contacts did exhibit circular polarization and hence spin injection, no such effect was seen here. What accounts for this difference? To answer this question, the current transport mechanism through the metal-semiconductor interface was explored.

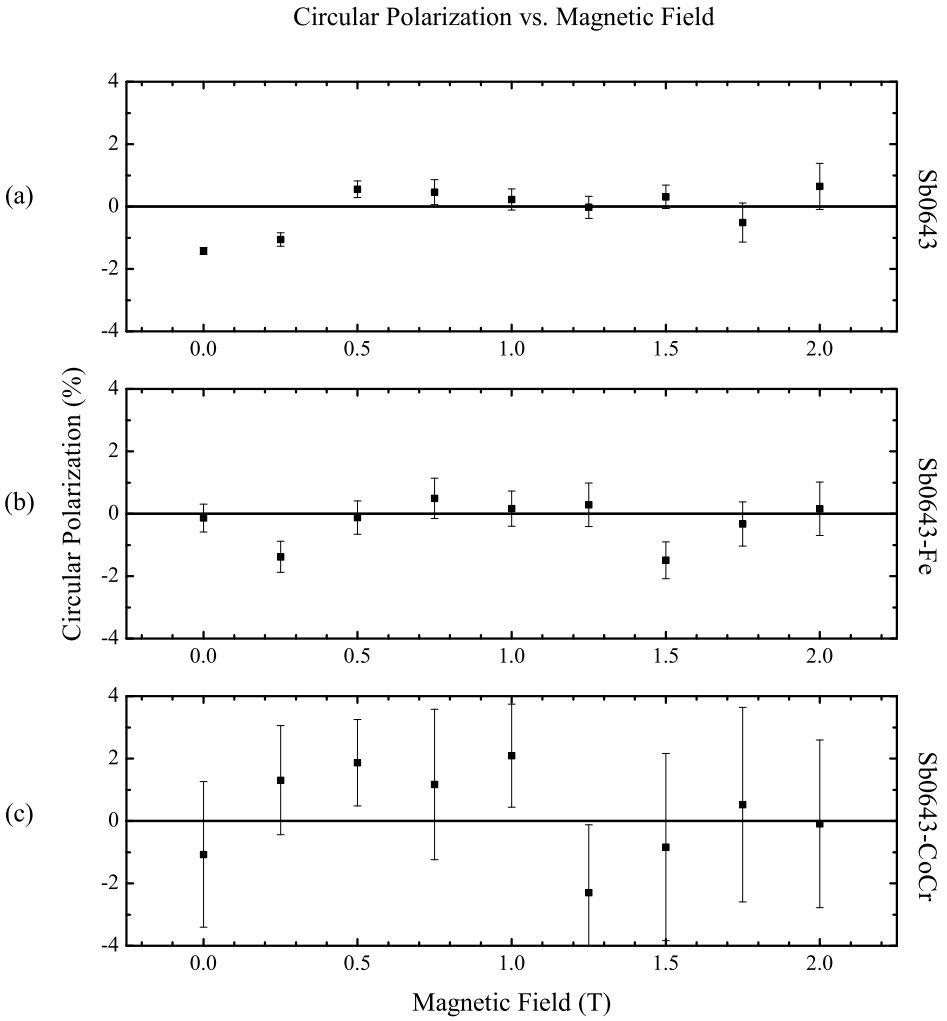


Figure 5.2: Spin injection results from control, Fe, and Co-Cr samples.

### 5.3.1 Assessment of Tunneling Current

Due to the conductivity mismatch problem (§1.3.1), some kind of resistive barrier is needed between the ferromagnetic metal and semiconductor so that the injection properties of the barrier dominate the spin transport. Smith and Silver have shown that this condition is met for normal metal-semiconductor Schottky tunnel barriers [7]. The device under consideration has been designed with this in mind, but is this requirement fulfilled?

The identification of tunneling as the conduction mechanism can be confirmed through application of the Rowell criteria [8, 9]. These three conditions, when satisfied, provide good evidence for tunneling as the dominant process. The conditions are:

1. that the current depends exponentially upon the barrier thickness
2. that the conductance, $G = dI/dV$, has a parabolic voltage dependence
3. that the resistance should weakly decrease with increasing temperature

For Schottky barriers, the first of these conditions is difficult to test due to the triangular shape of the tunnel barrier. The second and third conditions have been used by Hanbiki to prove that their observed spin injection in their Fe/GaAs spin-LEDs occurred through tunneling [10].

For Sb0643-CoCr, the conductance near zero applied bias is shown in Figure 5.3. According to the Brinkman-Dynes-Rowell (BDR) asymmetric tunnel barrier model, the conductance of the barrier should be

$$\frac{G(V)}{G(0)} = 1 - \left(\frac{A_0\,\Delta\phi}{16\,\bar{\phi}^{3/2}}\right) eV + \left(\frac{9}{128}\frac{A_0^2}{\bar{\phi}}\right)(eV)^2 \tag{5.2}$$

$$A_0 = 4\,\frac{(2m)^{1/2}\,d}{3\hbar} \tag{5.3}$$

$$G(0) = \left(3.16\times 10^{10}\,\frac{\bar{\phi}^{1/2}}{d}\right)\exp\left(-1.025\,d\,\bar{\phi}^{1/2}\right), \tag{5.4}$$

where $\Delta\phi = \phi_2 - \phi_1$, $\bar{\phi} = (\phi_1 + \phi_2)/2$, and $\phi_1$, $\phi_2$, and $d$ are the barrier heights and width as defined in the inset of Figure 5.3. Using this model, the barrier height was found to be $\phi_B = 0.50\,\text{eV}$ and the barrier width was $d = 5.18\,\text{Å}$. The parameters from this fit should not

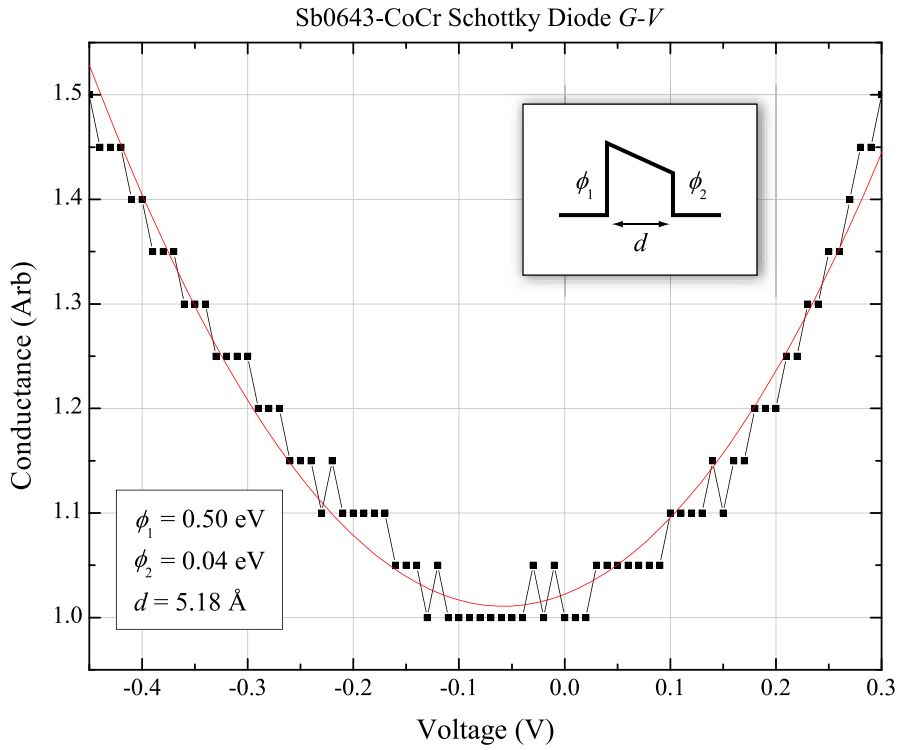


Figure 5.3: Sb0643-CoCr Schottky diode *G-V* characteristics. The conductance has been fitted using the BDR asymmetric barrier model, obtaining the barrier heights and width shown here. The tunnel barrier parameters are pictorially represented in the inset.

be considered true to the actual barrier. Rather, the second Rowell criterion is considered to be met if these values are reasonable.

To obtain a better idea of the Schottky barrier properties, current-voltage and capacitance-voltage characteristics were measured. The results from these measurements are shown in Figure 5.4. The *I-V* measurements give a barrier height of 0.726 eV while *C-V* indicates that $\phi_B = 0.46\,\text{eV}$. The difference between the two may be due to defects and in general, *C-V* barrier height measurements are considered more trustworthy [11]. In this case, the *C-V* measured barrier height matches nicely with $\phi_B$ as obtained by the BDR model fit.

Returning to the discussion on tunneling, the third Rowell criterion remains to be checked. Recall that the requirement is that the zero bias specific contact resistance must have a weak insulating temperature dependence. Figure 5.5a shows this dependence. Although the resistance does decrease with increasing temperature, the temperature dependence is stronger than that seen in the literature for tunneling [10]. It is concluded, therefore, that tunneling is not the dominant mechanism in current transport.

The current in a Schottky diode is composed of two components—thermionic emission and tunneling. Tunneling will dominate when the Schottky barrier is thin enough to allow for a significant probability for electron transmission. Otherwise, thermionic emission of carriers over the barrier will dominate. The specific contact resistance for thermionic emission-controlled current is

$$R_C = \frac{k}{qA^\star T} \exp\left(\frac{q\phi_B}{kT}\right), \tag{5.5}$$

where $A^\star$ ($8\,\text{A/K}^2\text{cm}^2$ in GaAs) is the effective Richardson constant [12]. If the contact resistance is determined by thermionic emission, a semilog plot of $R_C T$ versus $1/T$ should yield a straight line with a slope $q\phi_B/k$. Such a plot is shown in Figure 5.5b. The linearity of the data in this plot confirms that thermionic emission was the dominant process for conduction.

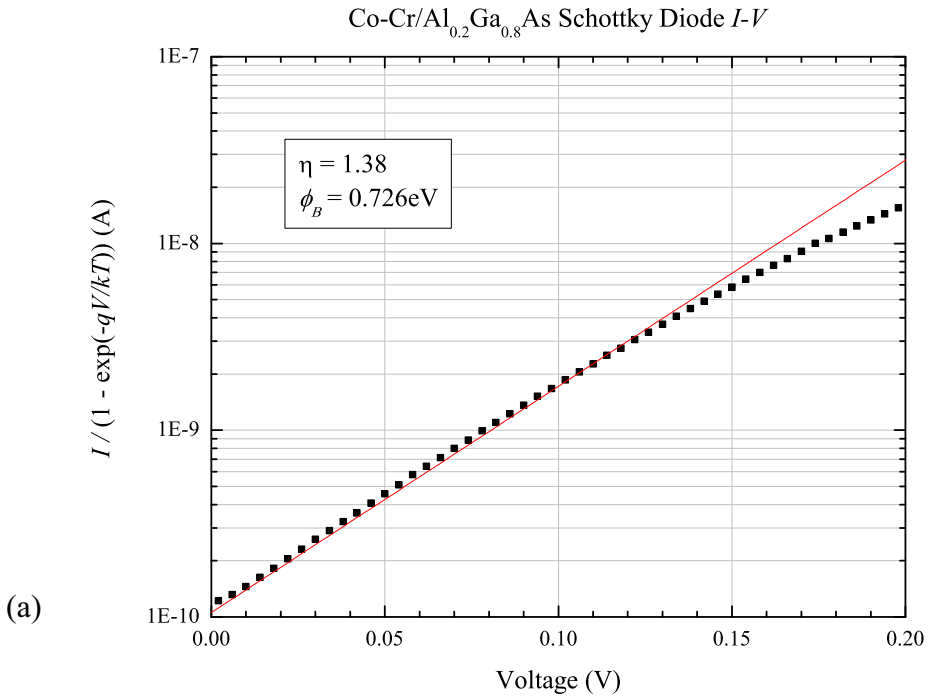


(a)

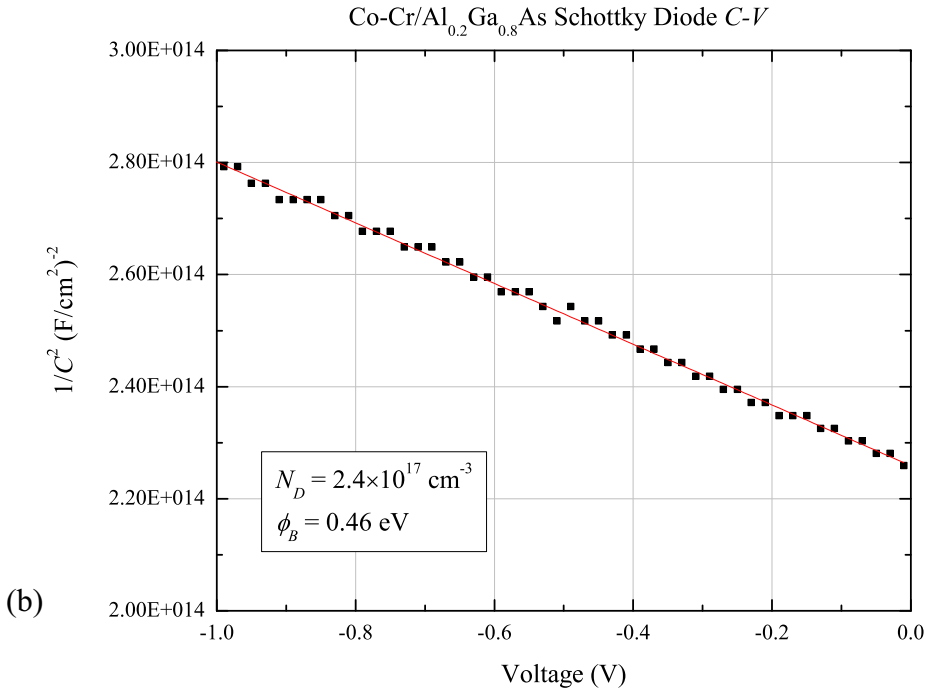


(b)

Figure 5.4: Sb0643-CoCr Schottky diode *I-V* and *C-V* characteristics. (a) Current-voltage behavior of the Schottky diode shows $\phi_B = 0.726$ eV. (b) Capacitance-voltage characteristics, on the other hand, show $\phi_B = 0.46$ eV. In general, *C-V* determination of the Schottky barrier height is considered more trustworthy than *I-V* measurements. The low doping doping density in (b) is due to depletion from the burried *p-n* junction.

(a)

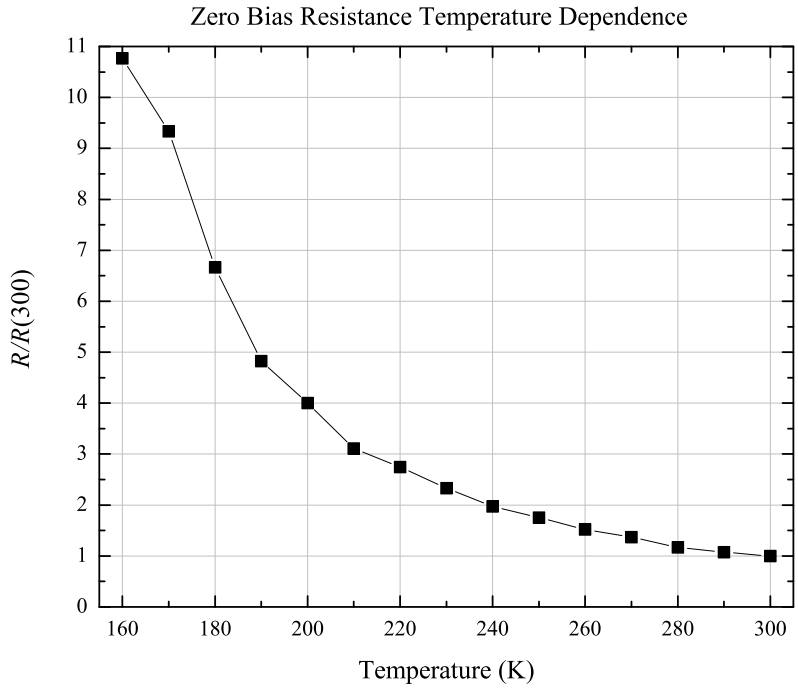


(b)

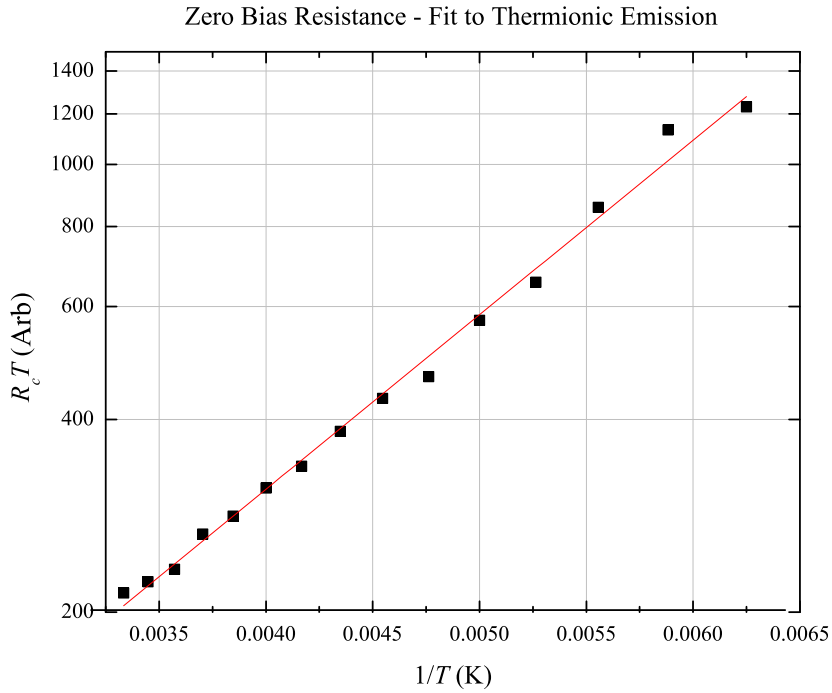


Figure 5.5: Sb0643-CoCr zero bias resistance. (a) Linear scale temperature dependence. (b) Fit to the thermionic emission model.

### 5.3.2 Growth Characterization Redux

Because the device current was shown to be dominated by thermionic emission whereas the design was made to ensure a large tunneling current, it would be wise to revisit the characterization of the growth to ascertain the root cause of the discrepancy between design and product.

Upon closer inspection of the growth logs, it was discovered that the pause in growth while the Si cell was ramped up in temperature was too short to allow the cell to reach its target temperature. The last 100 Å of $Al_{0.2}Ga_{0.8}As$ growth was intended to be $2 \times 10^{19}$ cm$^{-3}$ *n*-type while the preceeding 150 Å was supposed to be a transition from $2 \times 10^{18}$–$2 \times 10^{19}$ cm$^{-3}$ (see §3.2 for more growth details). Instead, the 150 Å region started at $1.3 \times 10^{18}$ cm$^{-3}$and the doping increased exponentially to $5.07 \times 10^{18}$ cm$^{-3}$. There it stayed for the remaining 100 Å of growth.

The effects of the doping discrepancy can be seen in Figure 5.6. The plot shows a SimWindows simulation of the conduction band edge in the semiconductor for the desired and actual doping densities. The metal-semiconductor contact occurs at $x = 0$ and the Schottky barrier height has been taken to be 0.46 eV.

The tunneling current is proportional to the tunneling probability:

$$I \sim \exp\left[-2d\sqrt{2m_n\left(q\phi_B - qV\right)/\hbar^2}\right], \tag{5.6}$$

where $V$ is the applied voltage. From the device simulation, the designed barrier width was 40 Å, but doping problems extended the width to 94 Å. Because of the exponential dependence of the tunneling current on the barrier width, $d$, the tunneling current for the as-grown structure was approximately ten times smaller than it was meant to be, giving one possible explanation as to why no spin injection was observed in these devices.

Another possible factor affecting spin injection is the quality of the metal-semiconductor interface. Although the interface was flat for both the Fe and Co-Cr samples (see figures 4.2 and 4.3), the bonding between these materials at the junction may have had a significant impact on the ability of this system to support spin-polarized transport. Analysis of this interface by X-ray photospectroscopy would illuminate these issues.

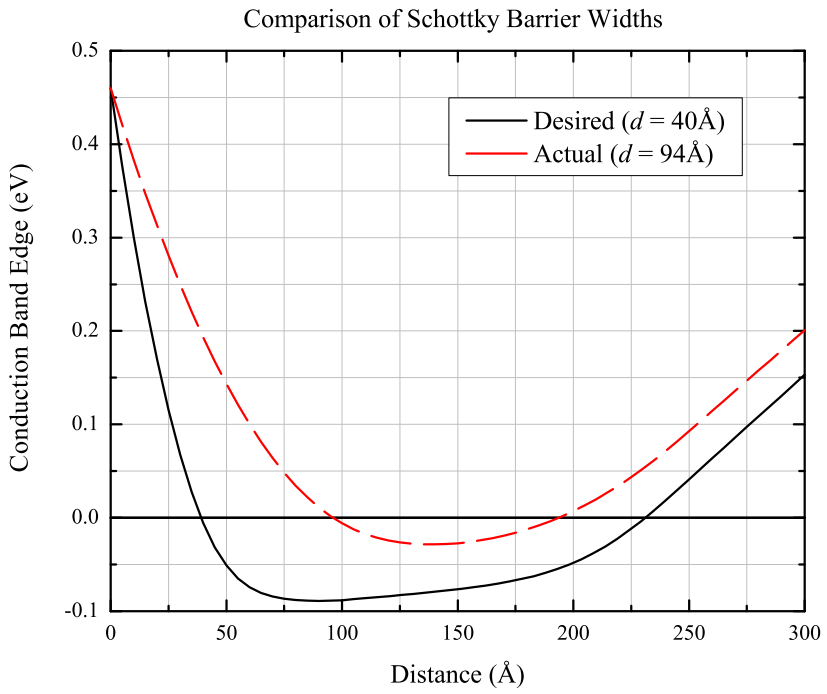


Figure 5.6: Designed and as-grown Schottky barrier widths. The increased width of the as-grown barrier exponentially decreases the tunneling current.

## 5.4 Summary

Circular polarization of the spin-LED electroluminescence was measured at 4.2 K as a function of magnetic field. No polarization signal was measured under applied magnetic fields of up to 4 T for either the Fe or Co-Cr spin-aligning contacts, in contrast to the positive results found elsewhere (see Table 1.1).

The absence of a polarization signal called into question the nature of the current flowing through the metal-semiconductor contact. Although tunneling was expected to be the dominant mechanism for current transport across the interface, thermionic emission could not be ruled out.

Use of the Rowell criteria confirmed that tunneling took a backseat to thermionic emission in these devices. Parabolicity of the differential conductance of the metal-semiconductor contact and reasonable values obtained by fitting this to the BDR asymmetric tunnel barrier model gave hope that tunneling was dominant. Testing the zero bias specific contact resistance, however, revealed a temperature dependence pointing to thermionic emission as the

conduction mechanism.

Close inspection of the growth logs indicated a deviation in the as-grown doping from the intended doping due to low Si cell temperatures during the last phase of growth. This resulted in a tunnel barrier more than two times wider than the device design, and therefore a supression of the tunneling current with respect to thermionic emission.

# References


[1] Marquardt, Ph.D. thesis, California Institute of Technology, 1995.

[2] *Operating Instructions for Superconducting Magnet Systems*, Janis Research Company, 1980.

[3] *Operating Instructions for Supplied Ancillary Equipment*, Janis Research Company, 1980.

[4] M. N. Jirmanus, *Introduction to Laboratory Cryogenics*, 1980.

[5] J. C. Kemp, *Polarized Light and its Interaction with Modulating Devices*, 1987.

[6] A. T. Hanbicki, B. T. Jonker, G. Itskos, G. Kioseoglou, and A. Petrou, Appl. Phys. Lett. **80**, 1240 (2002).

[7] D. L. Smith and R. N. Silver, Phys. Rev. B **64**, 045323 (2001).

[8] *Tunneling Phenomena in Solids*, edited by E. Burstein and S. Lundqvist (Plenum Press, New York, 1969).

[9] B. J. Jonsson-Akerman, R. Escudero, C. Leighton, S. Kim, I. K. Schuller, and D. A. Rabson, Appl. Phys. Lett. **77**, 1870 (2000).

[10] A. T. Hanbicki, O. M. J. van 't Erve, R. Magno, G. Kioseoglou, C. H. Li, B. T. Jonker, G. Itskos, R. Mallory, M. Yasar, and A. Petrou, Appl. Phys. Lett. **82**, 4092 (2003).

[11] W. F. Brinkman, R. C. Dynes, and J. M. Rowell, J. Appl. Phys. **41**, 1915 (1970).

[12] S. M. Sze, *Physics of Semiconductor Devices*, 2nd ed. (John Wiley & Sons, Inc., New York, YEAR).

# Appendix A Stokes Parameters

An electromagnetic plane wave of wavevector $\mathbf{k}$ can be described by

$$\mathbf{E}(\mathbf{x}, t) = (\boldsymbol{\epsilon}_1 E_1 + \boldsymbol{\epsilon}_2 E_2)\, e^{i(\mathbf{k}\cdot\mathbf{x}-\omega t)}, \tag{A.1}$$

where $E_1$ and $E_2$ are complex numbers representing the magnitude and phase of the electric field, and $\boldsymbol{\epsilon}_1$ and $\boldsymbol{\epsilon}_2$ are unit vectors such that $\boldsymbol{\epsilon}_1 \times \boldsymbol{\epsilon}_2 = \hat{\mathbf{k}}$. The polarization state of the wave is completely determined by the four quantities $\mathrm{Re}[E_1]$, $\mathrm{Im}[E_1]$, $\mathrm{Re}[E_2]$, and $\mathrm{Im}[E_2]$. Direct measurements of these four quantities, however, is not easily accomplished. Thus, it is more convenient to express the polarization state of the light in terms of combinations of these electric field components that can be directly measured in the lab.

The Stokes parameters satisfy this requirement and are given by [1, 2]

$$I = |\boldsymbol{\epsilon}_1 \cdot \mathbf{E}|^2 + |\boldsymbol{\epsilon}_2 \cdot \mathbf{E}|^2 \tag{A.2}$$

$$Q = |\boldsymbol{\epsilon}_1 \cdot \mathbf{E}|^2 - |\boldsymbol{\epsilon}_2 \cdot \mathbf{E}|^2 \tag{A.3}$$

$$U = 2\,\mathrm{Re}\left[(\boldsymbol{\epsilon}_1 \cdot \mathbf{E})^* (\boldsymbol{\epsilon}_2 \cdot \mathbf{E})\right] \tag{A.4}$$

$$V = 2\,\mathrm{Im}\left[(\boldsymbol{\epsilon}_1 \cdot \mathbf{E})^* (\boldsymbol{\epsilon}_2 \cdot \mathbf{E})\right]. \tag{A.5}$$

Using the the basis defined by $\boldsymbol{\epsilon}_1$ and $\boldsymbol{\epsilon}_2$, the Stokes parameters are identified as follows (see Figure A.1):

| | |
|---|---|
| $I$ | Total intensity |
| $Q$ | Degree of linear polarization along the $\boldsymbol{\epsilon}_1$- and $\boldsymbol{\epsilon}_2$-axes |
| $U$ | Degree of linear polarization along the diagonals $\frac{1}{\sqrt{2}}(\boldsymbol{\epsilon}_1 + \boldsymbol{\epsilon}_2)$ and $\frac{1}{\sqrt{2}}(-\boldsymbol{\epsilon}_1 + \boldsymbol{\epsilon}_2)$ |
| $V$ | Degree of circular polarization $RCP - LCP$ |

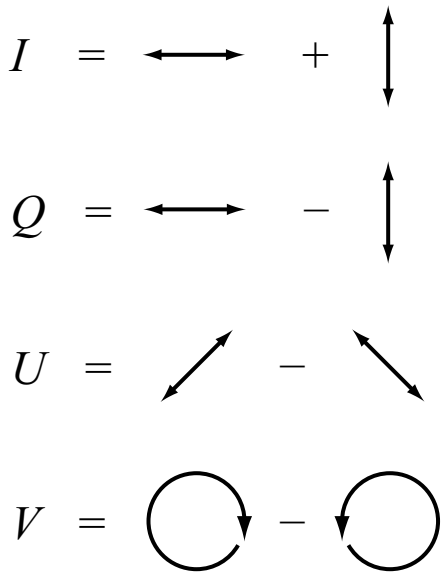


Figure A.1: Pictorial representation of the Stokes parameters.

If the normalized Stokes parameters $Q/I$, $U/I$, and $V/I$ are used, then the identification of the polarization state of the radiation becomes even easier. The three parameters that describe the degrees of linear and circular polarization then take on the maximum value of 1 when the light is completely polarized along one direction and $-1$ when the light is completely polarized along the orthogonal direction. Note that if one of these normalized Stokes parameters assumes its maximum or minimum value, the remaining two normalized Stokes parameters must be identically equal to 0.

# References

[1] J. D. Jackson, *Classical Electrodynamics*, 3rd ed. (John Wiley & Sons, Inc., New York, YEAR).

[2] E. Hecht, *Optics*, 3rd ed. (Addison-Wesley, New York, 1998).

# Appendix B Photoelastic Modulator Theory of Operation

The Hinds PEM-90 photoelastic modulator (PEM) utilizes the birefringence caused by the piezoelectric effect in a quartz crystal to introduce a phase shift to the polarization of light passing through the crystal. The magnitude of the phase shift depends upon the driving voltage, which alternates sinusoidally at a frequency $f$. Combined with other optical elements, a PEM can measure linear and circular dichroism, birefringence, as well as perform a complete analysis of the polarization state of light via Stokes polarimetry.

Figure B.1 shows the appropriate setup for use of the PEM for Stokes polarimetry. For incident light with polarization

$$\mathbf{E} = E_x\hat{x} + E_y\hat{y}, \tag{B.1}$$

where $E_x$ and $E_y$ are the complex components of the electric field along the $x$- and $y$-axes, the effect of the PEM is to introduce a time-dependent phase shift between the two polarization components. This phase shift is given by $\delta = A\cos\omega t$ where $A$ is the amplitude of the shift and $\omega = 2\pi f$ is the angular frequency at which the device operates. The light then passes through an analyzer oriented along $(-\hat{x} + \hat{y}) / \sqrt{2}$ and the intensity is recorded by a photodetector. At the detector, the intensity of the light is given by [1]

$$\begin{aligned} I_{\text{det}} &= |\mathbf{E}|^2 = I_0 - \Re\left[E_x E_y e^{i\delta}\right] && \text{(B.2)} \\ &= I_0 - 2\Re\left[E_x^* E_y\right]\cos\delta + 2\Im\left[E_x^* E_y\right]\sin\delta && \text{(B.3)} \\ I_0 &= |E_x|^2 + \left|E_y\right|^2. && \text{(B.4)} \end{aligned}$$

Looking back at Appendix A, we can identify a couple of the quantities in B.3 with the Stokes parameters (see equations A.2–A.5):

$$I_{\text{det}} = I_0 + U\cos\delta + V\sin\delta \tag{B.5}$$

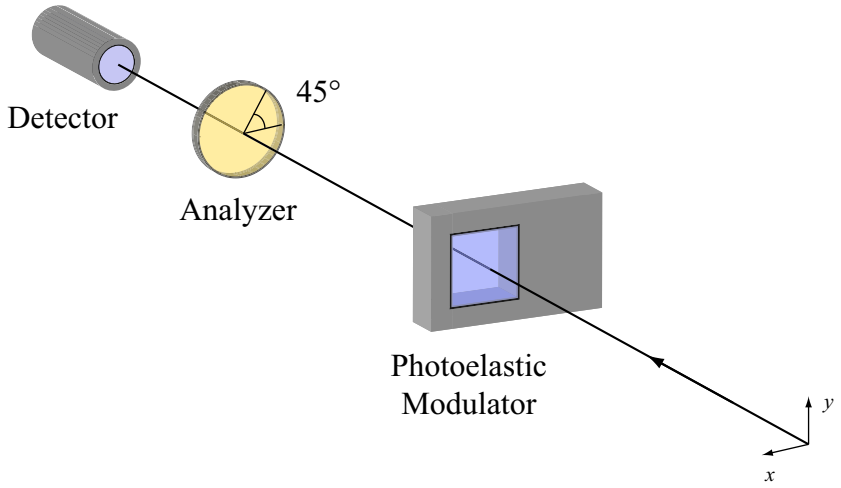


Figure B.1: Diagram of PEM usage for Stokes polarimetry. Light of an unknown polarization is conditioned by the PEM and analyzer so that polarization components are detectable as intensity modulations at frequencies $f$ and $2f$.

$$= I_0 + U\cos(A\cos\omega t) + V\sin(A\cos\omega t). \tag{B.6}$$

This equation can be put into more familiar terms by using the expansions

$$\cos(A\cos\omega t) = J_0(A) + 2\sum_{k=1}^{\infty}(-1)^k\cos(2k\omega t)\,J_{2k}(A) \tag{B.7}$$

$$\sin(A\cos\omega t) = 2\sum_{k=0}^{\infty}(-1)^k\cos((2k+1)\omega t)\,J_{2k+1}(A), \tag{B.8}$$

where the $J_k(A)$ are Bessel functions. Keeping only the first-order terms in these series, the intensity at the detector is therefore given by

$$I_{\text{det}} = I_0 + U\left[J_0(A) - 2J_2(A)\cos(2\omega t)\right] + 2V\,J_1(A)\cos(\omega t). \tag{B.9}$$

The intensity measured by the detector has a frequency component at $2f$, twice the PEM modulation frequency, which is proportional to the linear polarization $U$ and also to a component at $f$ which is proportional to $V$. Using a lock-in detection scheme allows for measurement of these quantities. The last remaining Stokes parameter, $Q$, can be measured by rotating both the PEM and analyzer by 45°.

# References

[1] J. C. Kemp, *Polarized Light and its Interaction with Modulating Devices*, 1987.